Pitting and Crack Initiation in High Strength Aluminum Alloys for Aircraft Applications

by

Hiu Au

B.S. Metallurgical Engineering
Carnegie Mellon University (1989)

Submitted to the Department of Materials Science and Engineering
in Partial Fulfillment of the Requirements for the Degree of
Doctor of Science

Massachusetts Institute of Technology
January 1996

Signature of Author. . . . . .
Department of Materials Science and Engineering
January 12, 1996

Certified by . . . . . .
Professor R.G. Ballinger
Thesis Supervisor

. . . . . .
Professor R.M.N. Pelloux
Thesis Supervisor

Accepted by . . . . . .
Professor M.F. Rubner
Chair, Departmental Committee on Graduate Students

Pitting and Crack Initiation in High Strength
Aluminum Alloys for Aircraft Applications

by

Hiu Au

Submitted to the Department of Materials Science and Engineering in partial fulfillment of the requirements for the Degree of Doctor of Science in Metallurgy

Abstract

The fundamental variables controlling the initiation of localized corrosion and stress corrosion crack initiation in 7178-T6 and 7075-T651 aluminum alloys were studied. The role of micro as well as macro material inhomogeneity were explored. Micro inhomogeneity was examined by evaluating the role of the intermetallic constituent particles. Macro inhomogeneity was examined by evaluating the role of steel fasteners in aluminum wing joints. A set of guidelines is given to compare the performance of different alloys.

Five intermetallic alloys were produced with the same chemical composition and crystal structure as the constituent particles found in aluminum alloys. Three of the intermetallics are variants of Al_2Cu with different concentrations of Zn (0-1.6 wt.%). The other two are $Al_6(Fe,Cu)$ and Al_3Fe. The electrochemical properties of these alloys and pure aluminum were obtained in NaCl environments. All the intermetallics were found to exhibit corrosion potentials more noble than aluminum. The intermetallics were more effective at reducing hydrogen and oxygen. The corrosion properties of aluminum alloys were modeled by applying the mixed potential theory. Galvanic experiments were conducted to verify these predictions. It is demonstrated that the constituent particles cannot cause localized film breakdown and pit initiation in deaerated environments. In aerated conditions however, localized film breakdown can be expected in the vicinity of these particles.

Two riveted wing joints from a replaced wing panel were disassembled. The electrochemical properties of the steel rivet and the aluminum alloy were obtained in NaCl solutions. The results indicate that pitting and intergranular attack can occur on the aluminum alloy in aerated and deaerated conditions. Alloys 7178-T6 and 7075-T651 cannot spontaneously repassivate in NaCl solutions. Once localized breakdown has begun, active dissolution continues. This accounts for the rapidity and severity of the corrosion damage often observed in steel riveted wing joints.

Controlled potential constant load and constant displacement (4-point bend) stress corrosion crack initiation experiments were conducted on 7178-T6 and 7075-T651 in NaCl solutions. The phenomenon of intergranular stress corrosion cracks (IGSCC) originating from pits was successfully reproduced in the laboratory.

Thesis Advisors: Professors R.G. Ballinger and R.M.N. Pelloux

Table of Contents

List of Figures

List of Tables

Acknowledgments

I would like to first acknowledge the support of my thesis advisors, Professors Ballinger and Pelloux. Special thanks go to Prof. Ballinger for his guidance and patience throughout the course of my studies at M.I.T. I am also grateful for the advice and encouragement from Prof. Pelloux who was essential in dispelling all the confusion.

I would like to thank Dr. Yutaka Watanabe for providing the much needed help and tutelage in the initial stages of the research.

I would like to express my deep appreciation to a special group of friends: members of the nuclear materials research group. Martin Morra, John Murphy, John Chun, and Dan Wang made my stay at M.I.T. much more enjoyable. To Jean-Marc Genkin, Dave Grundy and Bruce Brisson, I say, "Get back to work."

1.0 Introduction

Deterioration of aircraft structures occurs by many mechanisms. Mechanical damage, such as abrasion, wear, or fatigue can take place. Deterioration can also occur by corrosion which depends on the details of the design, the materials used, and the nature of the service environment. Corrosion damage, which can be general or localized, usually increases with the age of the airframe. Localized corrosion, including pitting, stress corrosion cracking, and corrosion fatigue, are the most significant sources of life limiting forms and degradations in airframes. As the aircraft ages, the effect of corrosion can become more pronounced. If corrosion damage is not detected early and repaired, it may represent a severe risk to the structural integrity of the aircraft.

Stress corrosion cracking which often initiates from the bottom of pits has been observed on aircraft components where corrosive environment and tensile stresses are present simultaneously. This form damage was observed on the wing box lower panel of a fighter aircraft which was fabricated from 7075-T6 aluminum alloy.[1] The predominant damage was pitting in the bores and countersink area of the fastener holes. Extensive intergranular cracking was observed to originate from these pits. "Several surface connected cracks can be seen running between fastener holes. Metallographic examinations showed that substantial intergranular cracking was associated with the surface connected cracks."[1] The failure of the trailing edge flap hinge lug in an F/A-18 has also been attributed to corrosion accelerated cracking.[2]

Most of the large military airframes in service are at least 15 years old with the average age of many, the KC-135 or B-52 for example, exceeding 25 years. More importantly, it is unlikely that replacement airframes will be built before the year 2020. The role of corrosion assisted damage, now very significant, will become critical and control the useful life of the airframe. Crack initiation and growth from pits or other localized corrosion damage is one of the primary forms of degradation. The development of an understanding for the evolution of corrosion damage, and its influence on the subsequent cracking behavior is therefore extremely important.

This research effort concentrates on thick gauge, high strength aluminum alloys used for wing applications. Alloy 7178 is a high strength variant of alloy 7075. Many older aircraft, with structural components manufactured from alloy 7178, are still in active service. The relationships between structural as well as microstructural material heterogeneity and the localized corrosion behavior in these aluminum alloys used for older and newer generation airframes are explored. In particular, the effect of the variables on pitting will be examined. Since cracks most often initiate from pits in these structures, the control of this form of localized corrosion is critical to life extension.

This thesis research is approached from the standpoint of electrochemistry. Passive film formation and its breakdown, pitting, are electrochemical processes. It is the local electrochemistry that determines the local environment. This environment, in turn, determines the stability of the protective film. Additionally, the dominant environmental factors such as the presence or absence of oxygen and chloride ions in the electrolyte determine the stability of surface films.

This thesis is organized in the following way. Chapter 1 presents an introduction. This includes a brief description of the electrochemical concepts necessary for the understanding of experimental procedures and results. The most important of these concepts is the mixed potential theory. The relationships between structural as well as microstructural components and the resulting corrosion potential are defined by the mixed potential. Chapter 2 presents a review of the relevant literature. The experimental procedures are described in Chapter 3 while Chapter 4 and 5 presents the results and discussion respectively.

1.1 Background

1.1.1 Electrochemical Relationships

Electrochemical reactions in general can be represented in the form

$$O + ne^- \rightleftarrows R \tag{1.1}$$

where O is reduced to R, or R is oxidized to O. Oxidation takes place at the anode while reduction takes place at the cathode. Equations 1.2 and 1.3 list examples of aluminum oxidation and hydrogen reduction reactions.

$$Al \rightarrow Al^{3+} + 3e^- \tag{1.2}$$

$$H^+ + e^- \rightarrow \frac{1}{2} H_2 \tag{1.3}$$

The Gibbs free energy change associated with equation 1.1 is

$$\Delta G = \Delta G^o + RT \ln \frac{a_R^*}{a_O^*} \tag{1.4}$$

where

- ΔG : Gibbs free energy change
- ΔG^o : changes in Gibbs free energy when the products and reactants are in their standard state
- R : universal gas constant (8.3144 Joules/deg • mole)
- T : temperature in degrees Kelvin
- a_O^* : activities of species O in the bulk
- a_R^* : activities of species R in the bulk.

Since electrochemical reactions involve the transfer of electrons, an electromotive force is set up between the anode and the cathode. This emf is related to the change in Gibbs free energy by

$$\Delta G = -nFE \tag{1.5}$$

where

- n : number of electrons involved in the electrochemical reaction
- F : Faraday's number (9.64846×10^4 C/equiv)
- E : emf of the cell.

The Nernst equation (equation 1.6) which defines the equilibrium potential is obtained by combining equations (1.4) and (1.5).

$$E_{eq} = E^o - \frac{RT}{nF} \ln \frac{a_R^*}{a_O^*} \tag{1.6}$$

where

E_{eq} : equilibrium corrosion potential

E^o : formal potential of an electrode.

When the electrodes are polarized from the equilibrium potential (E_{eq}), a net current will flow. The magnitude of this current is a direct measure of the reaction kinetics. The overpotential-current relationship is described by equation 1.7

$$i = i_o \left\{ \frac{C_O(0)}{C_O^*} \exp(-\alpha n f \eta) - \frac{C_R(0)}{C_R^*} \exp\left[(1-\alpha) n f \eta\right] \right\} \tag{1.7}$$

where

i : net current density

i_o : exchange current density

η : overpotential, = E - E_{eq}

$C_O(0)$: surface concentration of species O

$C_R(0)$: surface concentration of species R

α : transfer coefficient, a measure of the symmetry of the energy barrier for forward and backward reactions

$f = \frac{F}{RT}$ where F is the Faraday constant (9.64846×10^4 C/equiv)

R : universal gas constant (8.3144 Joules/deg • mole)

T : temperature in degrees Kelvin

The first term in equation 1.7 describes the cathodic component current at any potential, and the second gives the anodic contribution. There will be no mass transfer effects when the reaction kinetics is sluggish and/or mass transport is fast. Under these restrictions, equation 1.7 collapses to the well known Butler-Volmer equation (equation 1.8). Since mass transfer effects are not included in this equation, the overpotential associated with any given current acts solely as an activation energy.

$$i = i_o \left\{ \exp(-\alpha nf\eta) - \exp\left[(1-\alpha)nf\eta\right] \right\} \tag{1.8}$$

When $|\eta| > \frac{0.118}{n}$ V, the backward reaction contributes less than 1% of the total current at 25°C. As a result, one of the terms in equation 1.8 can be ignored and η - i follows a perfect logarithmic relationship. Under these restrictions, equation 1.8 is often presented in the form of

$$\eta = a + b \log(i) \tag{1.9}$$

In the case of low current and efficient stirring, mass transport effects are negligible. The current is therefore controlled by interface kinetics. Equation 1.9 was put forward by Tafel in 1905 [3] to model the electrode kinetics under these restrictions. Equation 1.9 is often referred to as the Tafel equation. Plots of $\log|i|$ vs. η, known as Tafel plots, will therefore yield a straight line at large values of η (either negative or positive).

When η is a large positive value, the second term in equation 1.8 can be ignored. Equation 1.8 can be rewritten as

$$i = i_o \left\{ \exp(-\alpha nf\eta) \right\}$$

$$\log i = \log i_o - \frac{\alpha nf\eta}{2.3} \tag{1.10}$$

The Tafel plot therefore has a slope of $\frac{\alpha nf}{2.3}$ and an intercept of $\log i_o$ when η is a large positive value. Similarly, the first term in equation 1.8 can be ignored when η is a large negative number. Equation 1.8 then becomes

$$i = i_o \left\{ -\exp\left[(1-\alpha)nf\eta\right] \right\}$$

$$\log i = \log i_o - \frac{(1-\alpha)nf\eta}{2.3} \tag{1.11}$$

The Tafel plot at large negative values of η will therefore has a slope of $\frac{(1-\alpha)nf}{2.3}$ and an intercept of $\log i_o$. These calculations are illustrated

graphically in Figure 1.1. Kinetics parameters such as the exchange current density (i_o) can easily be obtained from Tafel plots.

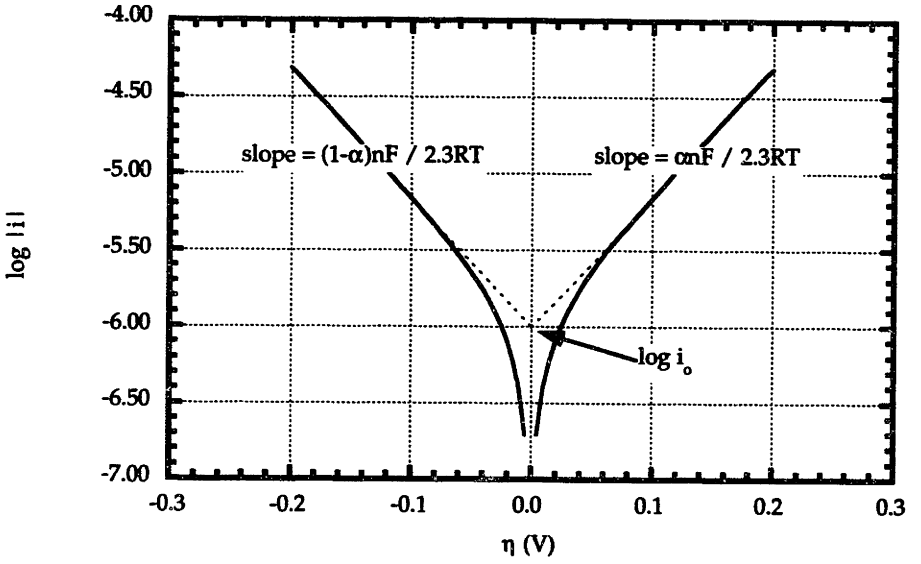

Figure 1.1. Tafel plot for the anodic and cathodic branches of the current – overpotential curve for the reaction $O + ne^- \rightleftarrows R$ with n=1, α=0.5, T=298K, and $i_o=10^{-6}A/cm^2$.

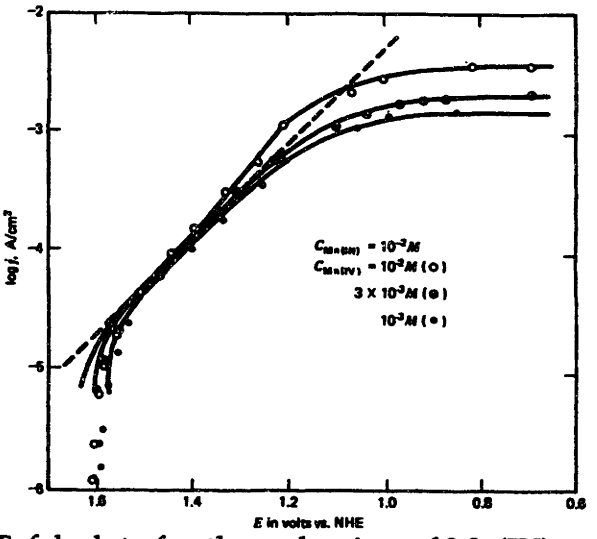

Figure 1.2. Tafel plots for the reduction of Mn(IV) to Mn(III) at Pt in 7.5M H_2SO_4 at 298K. Significant deviation from linearity can be observed at small and large values of overpotential.[4]

Significant deviation from linearity is often observed from experimental data at small and large values of η. Figure 1.2 shows the Tafel plot of reducing Mn(IV) to Mn(III) at Pt in 7.5M H_2SO_4. At small η, the contribution from the backward reaction cannot be ignored. Hence, both of the terms in equation 1.8 are needed to describe the overpotential–current relationship. At very large η, the reaction kinetics becomes controlled by the rate of mass transport. As a result, the current density becomes independent of η.

1.1.2 Anodic Polarization Behavior

Passivity can be defined as a loss of chemical reactivity under certain environmental conditions. This often results from the formation of a protective surface film. The corrosion rate of a metal is very low in this passive state. In other words, when a protective oxide film becomes the thermodynamically stable product in a specific environment, a dramatic reduction in the anodic current density can be expected.

The reaction kinetics in the passive state are essentially independent of potential. This is illustrated schematically in Figure 1.3. At very noble potentials, the current density increases with increasing potential. This is termed the transpassive region. The increased dissolution rate in the transpassive region is often caused by the destruction of the protective film. The potential where the transition between the passive and transpassive region occurs is called the film breakdown potential. In halide environments, corrosion pits often result from the localized breakdown of the protective passive film. The breakdown potential, in this case, is called the pitting potential (E_{pit}). In other words, pits can be observed on the material when the potential becomes more noble than E_{pit}.

Once the film breakdown has occurred, the material must be polarized to potentials more active than the repassivation potential (E_{repass}) before passivity is re-established. Repassivation potential is defined as the potential where the net current changes from anodic in nature to become cathodic. The repassivation potential is shown schematically in Figure 1.4.

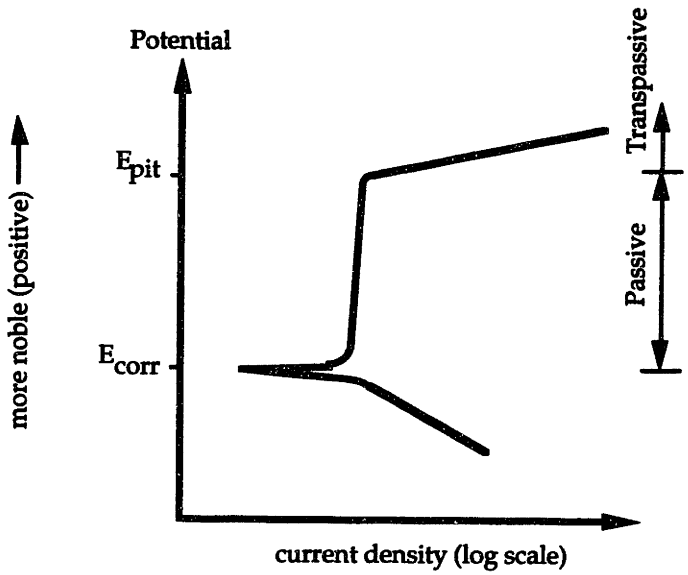

Figure 1.3. Schematic illustration of the passive and transpassive anodic polarization behavior.

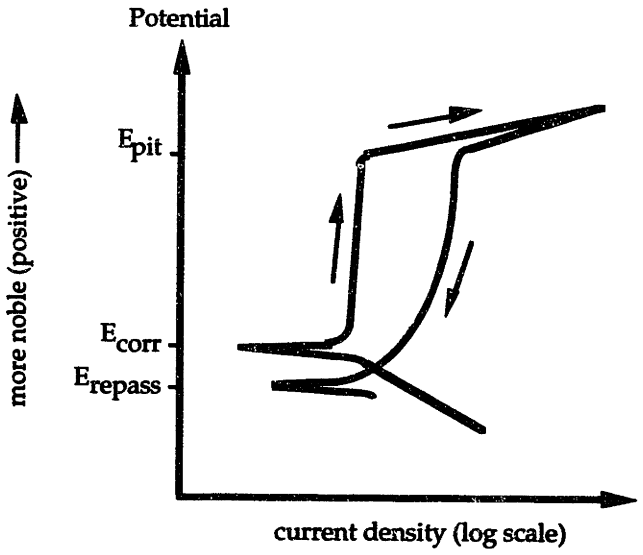

Figure 1.4. Schematic illustration of the repassivation potential (E_{repass}). The arrows indicate the direction of polarization.

1.1.3 Mixed Potential Theory

Thus far, the anodic and cathodic processes have been discussed separately. In actual systems, since charge conservation must be maintained, anodic and cathodic processes occur in a coupled manner. The equilibrium potential of the system is established at the point where each electron released by an oxidation reaction is consumed by a reduction reaction. The equilibrium

potential is thus a "mixed" potential. The process by which this occurs is discussed by the mixed potential theory.

The mixed potential theory consists of two simple hypotheses: [5]

1. Any electrochemical reaction can be divided into two or more partial oxidation and reduction reactions.
2. There can be no net accumulation of electrical charge during an electrochemical reaction.

The first of the hypotheses states that electrochemical processes are composed of coupled oxidation and reduction reactions. The second hypothesis is a restatement of charge conservation.

As an example, the reactions for zinc dissolution in acid are listed below (equations 1.12 and 1.13). Figure 1.5 shows a schematic for the application of mixed potential theory to this system. The overall dissolution of zinc in acid is broken down into the reduction of hydrogen ions (equation 1.12) and oxidation of zinc (equation 1.13). The free corrosion potential (E_{corr}) is defined as the potential where the anodic and cathodic currents are balanced as stated in hypothesis 2 above. Graphically, this implies that the corrosion potential (E_{corr}) is at the intersection of the cathodic and anodic branches in Figure 1.5.

$$2H^+ + 2e \rightarrow H_2 \qquad E_{eq} = -0.059\ pH\ V, SHE \qquad (1.12)$$

$$Zn^{2+} + 2e \rightarrow Zn \qquad E_{eq} = -0.763\ V, SHE \qquad (1.13)$$

Figure 1.5 illustrates the condition when corrosion is under mixed control of both the cathode and anode. That is, neither the anodic nor the cathodic process is dominant. When polarization occurs mostly at the anode, the corrosion rate is said to be anodically controlled. The corrosion potential in this case is near the open circuit potential of the cathode. Conversely, when polarization occurs mostly at the cathode, the process is cathodically controlled. Anodically and cathodically controlled systems are shown schematically in Figures 1.6 a and b respectively.

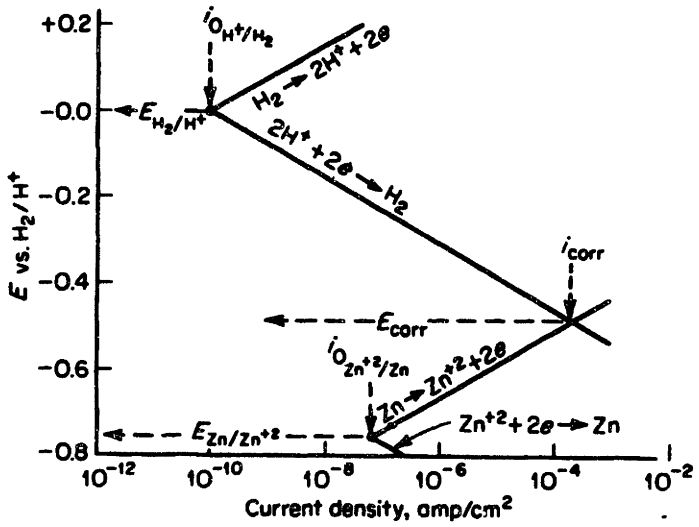

Figure 1.5. Schematic showing the electrode kinetics behavior of pure zinc dissolving in acid.[5]

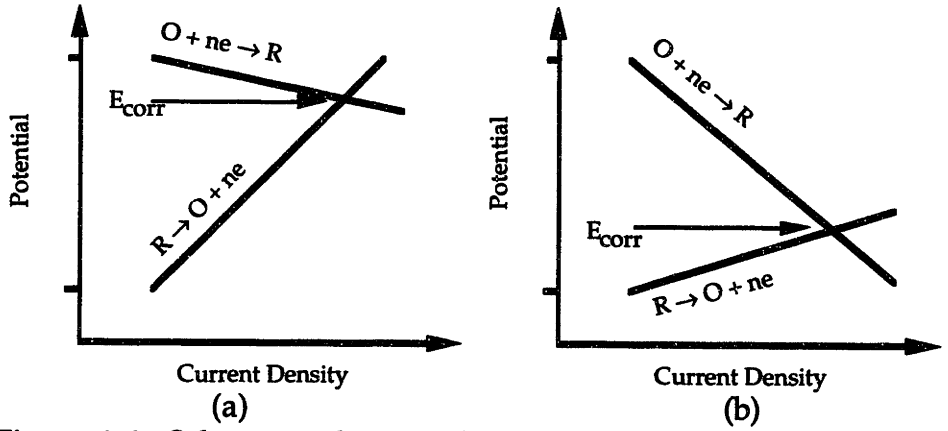

Figure 1.6. Schematic showing (a) anodic control, and (b) cathodic control of the free corrosion potential in a coupled system.

It is often necessary to measure the electrochemical potential of heterogeneous corroding metallic systems. In all but the most ideal systems with very pure metals, the observed free corrosion potential is defined by the mixed potential between individual phases and/or microstructural features such as grain boundaries, matrix, and any other chemical concentration differences. A primary example is the corrosion of precipitation strengthened alloys. Since the precipitates have different chemical composition than the matrix, galvanic couples are established when the alloy is immersed into an electrolyte. Additionally, the kinetics of the hydrogen and/or oxygen reduction reactions which are the most significant cathodic processes, are very

sensitive to the local chemistry, microstructure and phases present. The potential of a coupled cathode - anode galvanic system can be calculated by the mixed potential theory.

In this case, cathodic and anodic reactions can occur on each of the phases. The total cathodic current density in the coupled system at any potential is the sum of all the cathodic current densities weighted by their respective area fractions of the phases, equation 1.14.

$$i_{c,coupled} = f_\alpha i_{c,\alpha} + f_\beta i_{c,\beta} \qquad (1.14)$$

where

$i_{c,coupled}$: cathodic current density in the coupled system
f_α : area fraction of phase α in the coupled system
f_β : area fraction of phase β in the coupled system
$i_{c,\alpha}$: cathodic current density on α
$i_{c,\beta}$: cathodic current density on β.

Similarly, the total anodic current density in the coupled system is given by equation (1.15).

$$i_{a,coupled} = f_\alpha i_{a,\alpha} + f_\beta i_{a,\beta} \qquad (1.15)$$

where

$i_{a,coupled}$: anodic current density in the coupled system
$i_{a,\alpha}$: anodic current density on α
$i_{a,\beta}$: anodic current density on β.

The net current density ($i_{net,\ coupled}$) at any potential is simply the sum of the cathodic and anodic component currents.

$$i_{net,\ coupled} = i_{a,\ coupled} + i_{c,\ coupled} \qquad (1.16)$$

The free corrosion potential of the coupled system is found at the point where the net current density is zero (Hypothesis 2). Figure 1.7 is a graphical illustration of these calculations. $E_{eq,a,\alpha}$ and $E_{eq,a,\beta}$ are the equilibrium potential of the anodic reactions on α and β respectively. The equilibrium potential for the cathodic reactions are represented by $E_{eq,c,\alpha}$ and $E_{eq,c,\beta}$. In Figure 1.7, it is assumed that $E_{eq,c,\alpha}$ equals $E_{eq,c,\beta}$.

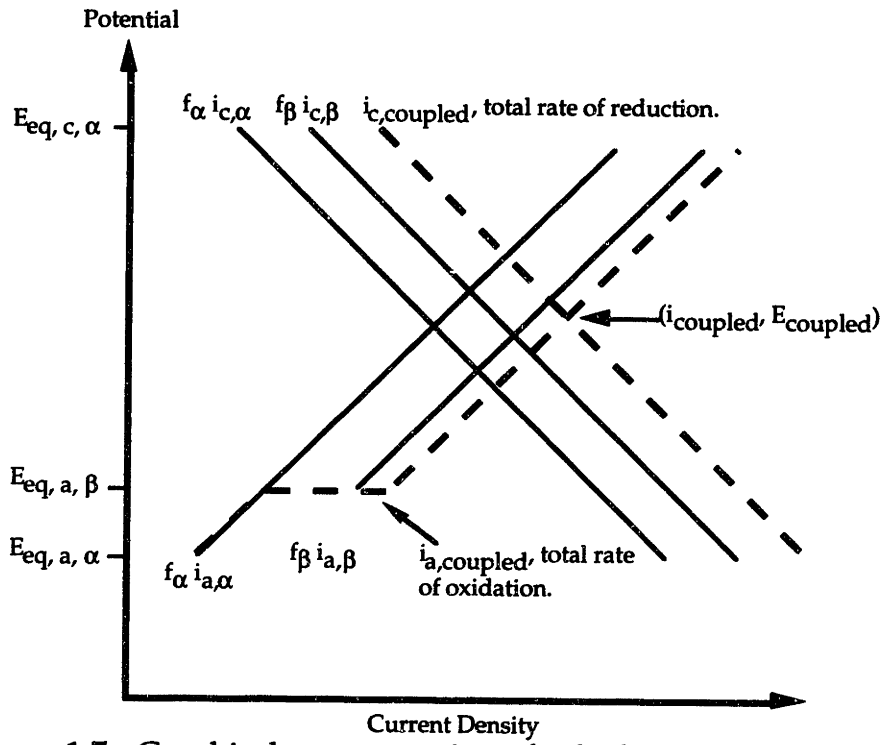

Figure 1.7. Graphical representation of calculations for the free corrosion potential in a coupled system.

The free corrosion potential of a coupled system varies as the area fraction of the phases changes. As f_α approaches 1, $E_{coupled}$ tends towards the free corrosion potential of the α phase (E_α). Similarly, $E_{coupled}$ is equal to E_β when f_β is 1. For the calculations outlined above, $E_{coupled}$ is always in between the free corrosion potentials of the individual components. In other words, $E_{coupled}$ is bounded by E_α and E_β. This is only true when there are no secondary reactions between the alloy systems. When the protective film becomes more stable due to alloying with the formation of denser mixed oxide for example, $E_{coupled}$ can be more positive (more noble) than the upper bound. Conversely, $E_{coupled}$ can be more negative than the lower bound when the oxide film becomes less stable by alloying.[6] These cases are presented graphically in Figure 1.8.

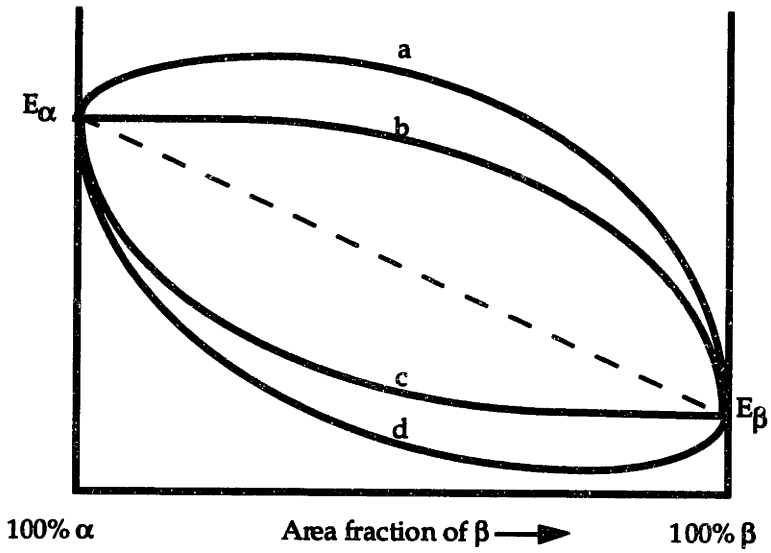

Figure 1.8. Schematic showing possible variations of coupled corrosion potential as a function of the area fraction of the phases under (a) formation of more stable protective film, (b) anodic control, (c) cathodic control, and (d) destabilization of protective film.

2.0 Literature Review

2.1 Physical Metallurgy

Aluminum alloys are widely used in the aerospace industry, in part, due to their high strength to weight ratio. The highest strength aluminum alloys are based on the Al-Zn-Mg-Cu system (7xxx series alloys). Typical composition and mechanical properties for some of these alloys are listed in Tables 2.1 and 2.2.

The 7xxx series aluminum alloys are precipitation strengthened. The most common heat treatments involve a solution treatment, quench, followed by an aging cycle. Table 2.3 shows some of the heat treatment practices used for these alloys. At the solution treatment temperature, most of the alloying elements are in solid solution. However, manganese rich intermetallics, often present in these alloys, may not be soluble and thus help to retard the movement of grain boundaries. As a result, the elongated shapes of cold worked grains are retained after heat treatment. It has been shown that the elongated grain shape reduces stress corrosion cracking (SCC) susceptibility.[7] Rapid cooling from the solution treatment temperature results in a homogeneous supersaturated matrix. With cooling rates slower than $1000^{o}F$/sec, heterogeneous nucleation of copper rich precipitates at grain boundaries can occur. This can result in copper depleted zones adjacent to the grain boundaries. The presence of these depleted zones is often proposed as the source of increased susceptibility to environmental degradation.[8]

The source of strengthening in age hardenable aluminum alloys is the precipitation of Guinier-Preston (GP) zones and derivative equilibrium phases. For the Al-Zn-Mg-Cu alloy system, the precipitation sequence at elevated temperature depends on the zinc to magnesium ratio. Spherical GP zones precipitate first followed by transformation to η', then to η ($MgZn_2$) in high zinc-magnesium ratio alloys. η' is a transitional phase which has a hexagonal structure. Its basal planes are coherent with {111} planes of the alloy matrix while the interfaces in its c axis are incoherent. The equilibrium η phase forms at longer aging time. At lower zinc to magnesium ratios, T ($Mg_3Zn_3Al_2$) replaces η as the equilibrium phase. A transition phase T' has

also been observed.[8] Table 2.4 summarizes the characteristics of these strengthening phases found in Al-Zn-Mg alloys.

Heterogeneous nucleation and growth of η along the grain boundaries is often observed in under aged and peak aged material. A solute depleted region, called the precipitate free zone (PFZ) is created adjacent to the grain boundaries due to this precipitation process. Figure 2.1 shows a TEM micrograph of a grain boundary decorated with coarse $MgZn_2$ particles. The PFZ adjacent to the grain boundary is clearly evident. Further aging leads to the diffusion of solute elements back into the PFZ eliminating the chemical heterogeneity. The presence of these PFZ is often sited as the cause of intergranular corrosion susceptibility.

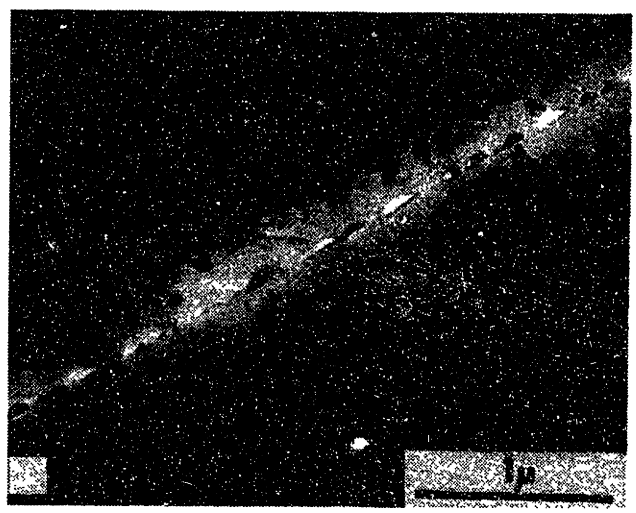

Figure 2.1. TEM picture showing the coarse $MgZn_2$ particles in the grain boundary and the adjacent precipitate free zone (PFZ) in Al-Zn-Mg alloy.[9]

Table 2.1. Chemical composition limits of commercial aluminum alloys (in wt.% maximum unless shown as a range).[10]

Alloy	Zn	Mg	Cu	Fe	Si	Mn	Cr	Ti
7049	7.2-8.2	2.0-2.9	1.2-1.9	0.35	0.25	0.20	0.10-0.22	0.10
7050	5.7-6.7	1.9-2.6	2.0-2.8	0.15	0.12	0.10	0.04	0.06
7075	5.1-6.1	2.1-2.9	1.2-2.0	0.50	0.40	0.30	0.18-0.35	0.20
7178	6.3-7.3	2.4-3.1	1.6-2.4	0.50	0.40	0.30	0.18-0.35	0.20
7079	3.8-4.8	2.9-3.7	0.40-0.80	0.40	0.30	0.10-0.30	0.10-0.25	0.10

Table 2.2. Mechanical and fracture properties for several aluminum alloys.[11]

Alloy-Temper	Thickness (in.)	Axis of specimen	Minimum Tensile Strength		Elong (% in 2in)	Range in plane strain fracture toughness, K_{IC} (ksi$\sqrt{in}$)		
			UTS (ksi)	0.2% YS (ksi)		Long.	Long trans	Short trans
7049-T73	2.000-3.000	LT	70	60	3	32-34	–	18-29
7050-T7351	–	–	–	–	–	36	30	26
7075-T651	0.500-1.000	LT	78	68	7	25-33	19-31	15-20
7075-T7651	0.500-1.000	LT	71	60	6	31	23-26	22
7075-T7351	0.250-1.000	LT	69	57	7	30-41	24-35	19-21
7079-T651	0.250-1.000	LT	74	65	8	25-34	22-28	15-18
7178-T651	0.500-1.000	LT	84	73	6	21-27	18-23	14-21
7178-T7651	0.500-3.000	LT	73	62	6	26-30	21-28	17-19

Table 2.3. Heat Treatments for Commercial Aluminum Alloys.[12]

Alloy	Temper	Solution Treatment (^{o}F)	Artificial aging treatment
7178	T6, T651*	875	24hr 250^{o}F
	T76, T7651*	875	3-5hr 250^{o}F + 15-18hr 325^{o}F
7075	T6, T651*	900	24hr 250^{o}F or 4hr 205^{o}F + 8hr 315^{o}F
	T7, T7351*	900	6-8hr 225^{o}F + 24-30hr 325^{o}F or 6-8hr 225^{o}F + 14-18hr 335^{o}F

* Stress relieved by cold stretching (to produce permanent set of 1.5% to 3% for sheet and plate) after solution heat treatment and prior to any elevated-temperature precipitation treatment.

Table 2.4. Characteristics of strengthening phases in Al-Zn-Mg alloys.[13]

	GP Zones	η'	η	T
Stoichiometry	—	$MgZn_2$	$MgZn_2$	$(Al,Zn)_{49}Mg_{32}$
Shape	Spherical	Platelets	Rods, plates	Irregular
Structure	Alternate layers of Mg, Zn	HCP, a = 4.96Å c = 8.68Å	HCP, a = 5.21Å c = 8.60Å	BCC a = 14.16Å
Coherency	Yes	Semi	No	No
Size	35Å	200Å long 50Å wide	500Å	—
Transition temperature (C)	120 - 160	120	200 - 250	190
Solvus temperature (C)	150	250	370	190

2.2 Localized Corrosion

The effect of copper on the corrosion properties of aluminum was recognized as early as the 1940's. Brown et al.,[14, 15] for example, produced a series of Al-Cu binary alloys which were solution treated for long periods of time at 525°C. These alloys were then quenched rapidly in cold water. The free corrosion potential of these alloys in the NaCl – H_2O_2 environment is made more noble (less negative) as increasing amount of copper is placed in solid solution. This is shown by the sloping curve in Figure 2.2. The break in the curve followed by the horizontal section indicates the solubility limit for copper at 525°C has been reached. Increasing the Cu content beyond the solubility limit has little effect on the solution potential of the alloy in the chloride environment examined.

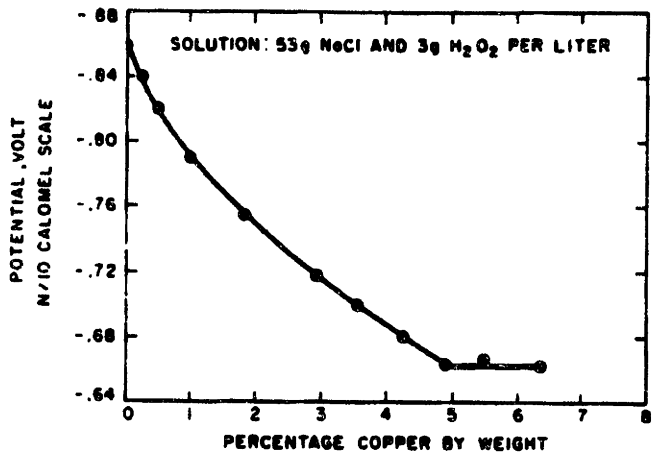

Figure 2.2. Plot of the solution potential for Al-Cu binary alloy in NaCl – H_2O_2 environment as a function of Cu content. The break in the sloping curve indicates the solubility limit has been reached.

Dix [15, 16] measured the open circuit potential between the matrix and grain boundaries of Al - 4% Cu in the same NaCl – H_2O_2 environment. Precipitates, presumably $CuAl_2$, were found along the grain boundaries. Copper depleted zones were observed adjacent to the grain boundaries. The corrosion potential of these copper depleted zones were found to be 0.044V more active than the grain matrix. Dix thus concluded that the intergranular corrosion susceptibility of the material is caused by the difference in the corrosion potential between these regions.

The effect of other principal alloying elements on the corrosion potential of aluminum binary alloys are summarized in Figure 2.3. Manganese has a similar effect as copper. Namely, increasing the Mn content increases the corrosion potential to more noble values. Zinc and magnesium have the opposite effect. The corrosion potential becomes more active when the Zn and Mg content is increased.

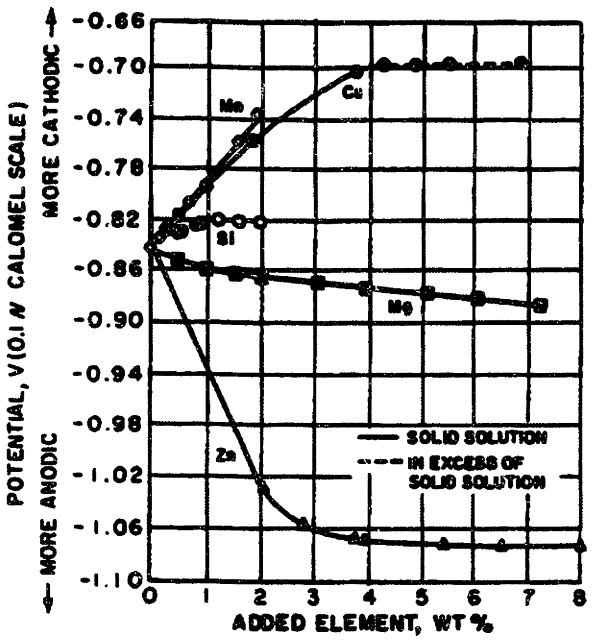

Figure 2.3. Effects of principal alloying elements on the solution potential of Al binary alloys in NaCl – H_2O_2 solution at 25°C.[17]

The mechanism proposed by Dix however, does not explain why halide ions are necessary for intergranular corrosion. Galvanic corrosion should occur in any conductive electrolyte. As a result, Galvele et al. [18, 19] proposed that intergranular corrosion susceptibility resulted not from the difference in corrosion potential, but from the difference in the film breakdown potential of these materials in halide environments. Figure 2.4 shows the anodic polarization behavior of pure aluminum in deaerated NaCl solution. The film breakdown potential is defined as the potential where there is a marked increase in the current density and is labeled as E_p in Figure 2.4.

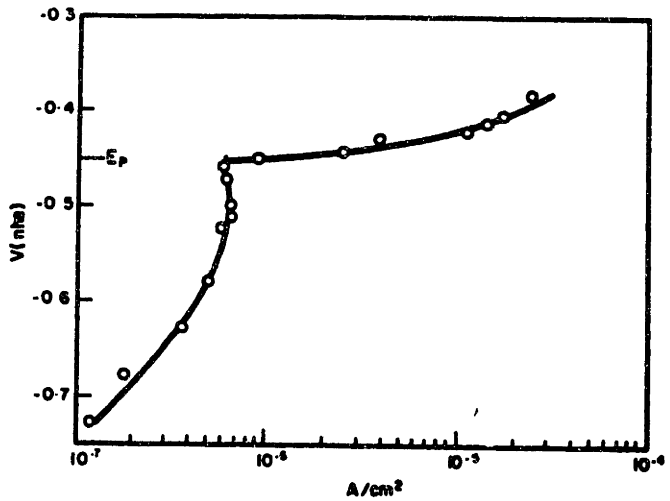

Figure 2.4. Anodic polarization curve of 99.99% Al in deaerated 0.1M NaCl solution. The breakdown potential (E_p) is the potential at which there is a marked increase in current density and signifies the onset of pitting. [18]

Although pure aluminum is a highly reactive metal, the formation of a surface film often results in passivity. Figure 2.5 shows a phase stability diagram (Pourbaix diagram) for the aluminum system. $Al_2O_3 \cdot 3H_2O$ is the thermodynamically stable phase in aqueous environments with pH of roughly 4 to 10.[20] This oxide is stable to very noble (positive) potentials. The stability of this film however, is strongly influenced by the presence of halide ions. When aluminum alloys are polarized to potentials more noble than the film breakdown potential in halide environments, corrosion pits are observed on the surface of the alloy. The film breakdown potential, in this case, is therefore labeled as the pitting potential (E_{pit}). In other words, pits will form when the potential become more noble than E_{pit}.

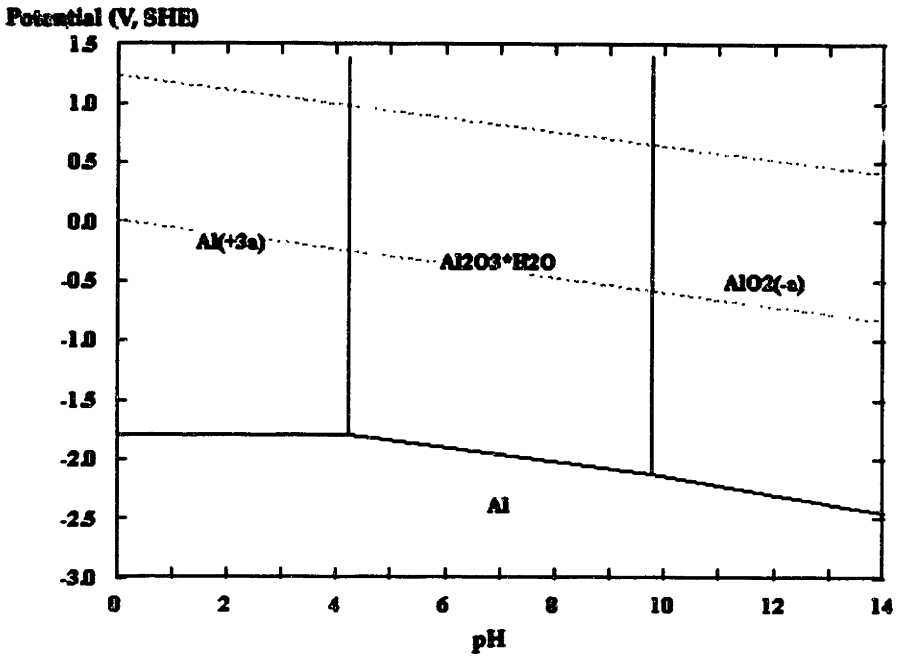

Figure 2.5. Pourbaix diagram showing regions of stability, passivity, and general corrosion for aluminum in aqueous environment at 25°C.

Acidification and enrichment of chloride ions are often observed within active pits.[21] During localized corrosion in chloride environments, hydrolysis of metal ions by reactions such as

$$Al^{3+} + 6H_20 \rightarrow Al(OH)_3 \bullet (H_2O)_3 + 3H^+ \qquad (2.1)$$

can cause the pH to drop to 3.5 at the bottom of a pit. Chloride ions then migrate into the pit in order to maintain charge neutrality.[21] The pit, in essence, is filled with hydrochloric acid. Repassivation of the active pit becomes impossible because the oxide is no longer the thermodynamically stable phase in this aggressive environment. Active dissolution therefore continues. The process can become autocatalytic as increased dissolution occurs with decreasing pH.

The pitting potential for numerous alloy systems are often found to have a logarithmic dependence on the chloride ion concentration or activity.[22, 23, 24] The data reported in the literature are usually in the form of:

$$E_{pit} = A + B \log [Cl^-] \qquad (2.1)$$

and B is found to depend on the composition of the supporting electrolyte, the measurement technique, and the metal involved.[25] In the case of aluminum alloys, B has been reported to be in the range of 0.05 to 0.13V.[18, 26]

The effects of principal alloying elements on the film breakdown potential of aluminum have been studied. Nilsen and Bardal [27] reported that the additions of magnesium (0.95, 2.7, and 4.5% Mg), manganese (0.8%), or silicon (0.83%) does not significantly affect the film breakdown potential of aluminum alloys in artificial sea water. The addition of tin, however, dramatically lowers the film breakdown potential. The potential drops 0.5V when 0.1% Sn is added.[28]

Wood et al. [29] observed that the surface oxide films on all aluminum, whatever the surface finish, contain sufficient flaws to provide sites at which pits may initiate. Similarly, Szklarska-Smialowska [30] proposed that aluminum oxide film is not an effective barrier against the penetration of water and chloride ions to the metal surface. She suggested that the rate determining step for stable pit growth, is not the diffusion of aggressive species in the environment through the oxide film, but the development of a stable aggressive environment which allows the continuous dissolution of the metal. These flaws in the film are more severe near copper or iron rich segregates because these precipitates interfere with the oxide growth above and around them. More recently, Seri [31] studied the corrosion behavior of a Al-1.4%Fe alloy in NaCl solutions and proposed that the oxide film in the aluminum matrix adjacent to $FeAl_3$ particles is weak. Pits then initiate at such weak spots and propagate by metal dissolution into the material and by undermining of the oxide film.

Exfoliation refers to the observed corrosion damage which consists of layers of corroded and uncorroded metal. Selective strata of material are corroded forming wedges of corrosion products. The corrosion products then forces the uncorroded layers upward giving rise to a blistered appearance.[32] Exfoliation has been observed in AlMg, AlZnMg, and AlZnMgCu systems of alloys.[33] Manganese depleted regions, which have a more active corrosion potential, have been reported as the sites of corrosion.[33]

2.2.1 Constituent Particles

Iron and silicon are the dominant impurities in commercial grade aluminum alloys. Although iron is highly soluble in molten aluminum, the solubility of iron in solid aluminum is very low (~0.04%).[34] Similarly, the solubility of silicon decreases from 12.6% in molten aluminum to 1.65% in solid aluminum.[34] Most of the iron will therefore precipitate out during solidification forming large second phase particles. Theses particles are usually in the order of 10 μm in diameter and are labeled as constituent particles. Depending on the purity of the aluminum alloy, the volume fraction of constituent particles can range from 0.1% to roughly 3%.

The large second phase constituent particles in aluminum alloys are often cited as the initiation sites of localized corrosion. Elevated iron contents have been reported to increase the pitting susceptibility of Al alloys in halide environments.[21, 35, 36] Hübner et al. [21] suggested the $FeAl_3$ precipitates act as cathodes in local cells on the metal surface resulting in the increased pitting susceptibility.

Gehring and Peterson [37] found that pits tend to initiate from constituent particles in 5456-H137 Al alloys in sea water. The composition of the particles, based on EDX analysis, roughly conformed to $(Cr,Fe,Mn)Al_6$. They suggested that pits initiate around an intermetallic particle due to galvanic interaction between the matrix and the particle.

It is obvious that the large second phase constituent particles play a significant role in the initiation of localized corrosion in aluminum alloys. It is therefore useful to review the possible phases that can be present in the Al-Zn-Mg-Cu alloy system. No element is known to have complete miscibility with aluminum in the solid state.[38] Constituent particles can form from the melt when the concentration of the alloying element exceeds its solubility in solid aluminum. Table 2.5 lists the solubility limits for various binary aluminum alloys in both the liquid and solid state while Table 2.6 lists the phases that have been observed in the Al-Cu-Mg-Zn-Fe-Si-Cr system. Depending on the cooling rate during solidification, and the subsequent heat treatments, not all the phases mentioned in Table 2.6 may appear simultaneously in the alloy.

Table 2.5 Solubility limits for various binary aluminum alloys.[38]

Element	Temp.(^{o}C)	Liquid Solubility (wt.%)	Solid Solubility (wt.%)
Cu	550	33.15	5.67
Cr	660	0.41	0.77
Fe	655	1.87	0.052
Mg	450	35.0	14.9
Si	580	12.6	1.65
Zn	380	95.0	82.8

Table 2.6 Possible phases in the Al-Cu-Mg-Zn-Fe-Si-Cr alloy system.[38]

Alloy system	Alloy examples	Alloy form	Phases
Al-Cu-Mg-Zn-Fe-Si-Cr	7075,7178	Ingot	$(Fe,Cr)Al_3$, $(Fe,Cr)_3SiAl_{12}$, Mg_2Si, $Mg(Zn_2AlCu)$, $CrAl_7$
		Wrought	$(Fe,Cr)SiAl_{12}$, Cu_2FeAl_7, Mg_2Si, $CuMgAl_2$, $Mg(Zn_2AlCu)$, $Cr_2Mg_3Al_{18}$

2.3 Stress Corrosion Cracking

Stress corrosion cracking (SCC) is the synergistic interaction between tensile stress and corrosion acting on a susceptible material in a specific environment. SCC crack velocity for Al-Zn-Mg-Cu alloys is strongly influenced by their copper content and heat treatment conditions.[39] Figure 2.6 shows that increasing the copper content above 1% and overaging the material can reduce the SCC crack growth rate by several orders of magnitude. The relation between SCC susceptibility and the microstructure for the 7xxx series aluminum alloys can be summarized as follows:[40]

Microstructure	Susceptibility
• Solution treated, no grain boundary precipitation	Immune
• Underaged	Maximum
• Peak aged	Susceptible
• Overaged	Decreases with aging

Although many mechanisms have been proposed for the initiation and growth of intergranular stress corrosion cracking (IGSCC) in high-strength aluminum alloys, two basic theories have evolved: stress assisted anodic dissolution (active path), and a hydrogen embrittlement based mechanism. The anodic dissolution mechanism suggests that a highly localized form of anodic attack occurs along grain boundaries which is aided by tensile stress. The hydrogen embrittlement mechanism, on the other hand, emphasizes the ingress of aggressive hydrogen atoms which leads to a general loss of ductility.

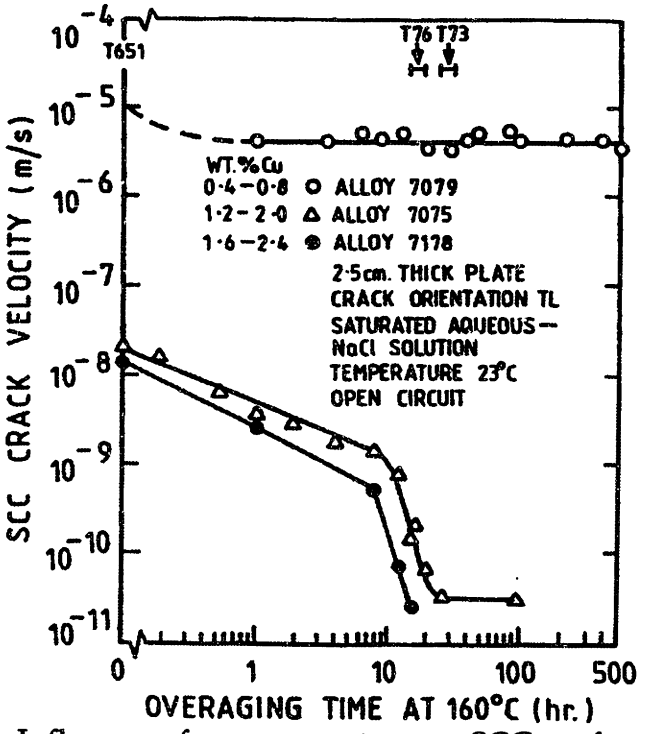

Figure 2.6. Influence of copper content on SCC performance as a function of aging time at 160°C.[41]

2.3.1 Anodic Dissolution

Stress assisted anodic attack is favored by some researchers as the mechanism of IGSCC in the Al-Zn-Mg-Cu alloys. The dissolving phase is either the grain boundary region or the precipitates. For example, Maitra and English [42, 43] studied the corrosion behavior of 7075-T651 and -T7351 in 3.5% NaCl solution. They found that the material is susceptible to both intergranular attack (IGA) and pitting when peak aged (T651) , but only susceptible to pitting when overaged (T7351). They reasoned that in the peak aged material, heterogeneous nucleation and growth of η ($MgZn_2$) at the grain boundaries

preferentially enriched these sites with Mg and Zn which leads to the increased intergranular corrosion susceptibility. Homogeneous nucleation of η within the matrix in the overaged condition reduces the corrosion potential gradient between the matrix and the grain boundary regions.[44] As a result, the material is no longer susceptible to IGA.

Sedriks et al. [9] studied the electrochemical properties of the intermetallic phase $MgZn_2$ and Al-Zn-Mg alloys in NaCl and $AlCl_3$ solutions. They found the intermetallics to be more anodic than the alloys in environments similar to those found in active crack tips. As a result, they concluded that pits are formed by the dissolution of $MgZn_2$ precipitates. A crack is then formed by the lateral coalescence of these pits due to the applied stress. The crack grows by either ductile fracture or active dissolution until the next particle is reached. Once the crack tip reaches the next $MgZn_2$ particle, the process is repeated again. These processes are illustrated in Figure 2.7.

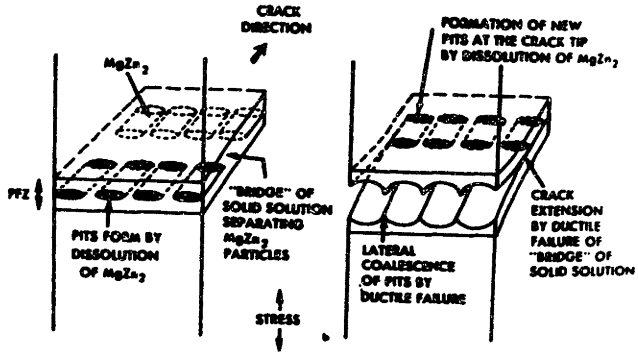

Figure 2.7. A schematic illustration of crack propagation mechanism involving the dissolution of $MgZn_2$ particles and ductile failure of the "bridge" material at the grain boundary.[9]

Poulose et al. [45] on the other hand, found that the SCC crack velocity, with stress intensity factor taken into account, is inversely proportional to the volume of $MgZn_2$ in the grain boundary. They proposed that the grain boundary precipitates act as sacrificial anodes to retard IGSCC. However, they cautioned, "this advantage (of increasing the volume of $MgZn_2$ at the grain boundary) would have to be balanced against the possible disadvantage that having larger precipitates might contribute to crack initiation."

Attempts to correlate the size of the precipitate free zone (PFZ) and SCC susceptibility has added to the confusion. Some researchers found that the width of the PFZ has no effect on SCC [46, 47]. Others, on the other hand, have detected increasing [48] as well as decreasing [49] susceptibility as the width of the PFZ is reduced.

2.3.2 Hydrogen Embrittlement

The presence of cathodically charged internal hydrogen has been linked to the loss of ductility in high strength aluminum alloys.[50, 51, 52, 53] This is often demonstrated by a reduction of area in a tensile test and the occurrence of intergranular fracture. Lynch [54] suggested that hydrogen increases the plasticity in the material which leads to the loss of ductility. Brittle hydride formation [55, 56], crack blunting with hydrogen bubbles [57], reduction in cohesive strength [58], microvoid nucleation [59], and pressurization by hydrogen bubbles [60] have also been suggested as the cause of hydrogen embrittlement. Since hydrogen atoms are generated during corrosion in aqueous environment, hydrogen embrittlement is frequently quoted as the cause of intergranular stress corrosion cracking (IGSCC) in the Al-Zn-Mg-Cu system.

Hydrogen must be present ahead of an advancing crack tip for it to cause embrittlement. Volume diffusion of hydrogen in aluminum however, is extremely sluggish, usually orders of magnitude slower than the SCC growth rate. This led Albrecht et al. [61] to suggest that hydrogen is transported by mobile dislocations rather than bulk diffusion. They showed that straining plus cathodic charging of hydrogen embrittles the high purity underaged 7075 alloy more than charging alone. They also found that a notch accelerates the embrittlement process. As a result, they concluded that hydrogen transport by mobile dislocations is not only possible, but is kinetically preferred to volume diffusion.

Gruhl [62], on the other hand, suggested that hydrogen transport is via the grain boundaries. He proposed that hydrogen solubility in the grain boundaries is influenced by the amount of Zn in solid solution at the grain boundaries, and the magnitude of the tensile stress normal to the boundaries. He showed a linear inverse correlation between the amount of Zn in solid

solution and the time to failure. Grain boundaries, having a lower elastic modulus than the matrix, are preferentially opened up by the tensile stress. As a result, the ingress of atomic hydrogen is greatly accelerated when the grain boundaries are depleted in Zn and are opened up by the tensile stress which leads to IGSCC.

Thompson et al. [63] showed that the loading mode strongly affects the SCC susceptibility of 7075 aluminum alloy. The time to failure in $AlCl_3$ solution for materials under mode I loading (tension) was much shorter than that under mode III loading (torsion). The fracture surfaces from mode I failures were highly intergranular in nature while mode III fracture surfaces were predominantly transgranular ductile type failure. The triaxial stress state at crack tips in mode I can assist hydrogen cracking but cannot assist anodic dissolution. SCC which takes place by a hydrogen mechanism should therefore be more pronounced in mode I and slightly less or absent in mode III while SCC due to anodic dissolution should be similar in both loading modes. Thompson et al. therefore concluded that SCC propagated by a hydrogen embrittlement mechanism which led to the much greater SCC susceptibility in mode I loading.

Speidel [64] observed that when the material contains a high volume fraction of coherent particles, it is highly susceptible to SCC. When the material contains a high volume fraction of incoherent particles, on the other hand, it becomes highly resistant. A higher volume fraction of incoherent precipitates are formed for the copper rich alloys after the same heat treatment because copper accelerates the transformation kinetics from coherent GP zones to incoherent η phase. As a result, the copper rich alloys are less susceptible to SCC after a short heat treatment while alloys with less than 1 wt% copper required gross overaging before high resistance to SCC is achieved (Figure 2.6).[65]

Speidel [64] observed that alloys with very few active slip planes are more susceptible to SCC. Coherent particles which are usually sheared during deformation produce a highly localized deformation structure. The shear stress at which a dislocation can shear a particle depends on the cross sectional area of the particle on the slip plane. As a particle is sheared, its cross sectional area on the active slip plane is reduced. Once a slip plane is

activated, it therefore becomes the preferential slip system as the shear stress required for further deformation is reduced. When a particle is looped, as in the case of incoherent particles, no such reduction of shear stress occurs. Thus, other slip systems are just as likely to be active. That is, alloys with a high volume fraction of coherent particles have very few active slip systems; the deformation is highly localized. Large numbers of dislocations are therefore restricted to the few active slip planes which leads to large number of dislocations piled up at the grain boundaries. The stresses at the head of the pile up, and the height of the slip step is proportional to the number of the dislocations in the pile up. Thus, alloys with a large volume fraction of coherent particles have very localized deformation characteristics which in turn leads to very large dislocation pile ups at grain boundaries. Speidel attributed the increase susceptibility of these alloys to either the magnified stresses experienced at the head of a pile-up which aids in the nucleation of a crack, or the increased step height which makes repassivation of an exposed surface more difficult.

Researchers concentrating on the hydrogen embrittlement mechanism of SCC [61, 66, 67] also have made use of the deformation mode argument. They reasoned that if hydrogen is transported by mobile dislocations, the hydrogen concentration ahead of an advancing crack is going to be higher when the mobile dislocations are constricted to very few active slip planes. Hence, SCC susceptibility is higher for non-copper-containing alloys which have a very localized deformation characteristics. For these authors, matrix precipitates are their primary concern. These matrix precipitates exercise the most control on the deformation mode which in turn influences the rate of hydrogen transport to the crack tip. Grain boundary precipitates can only play a secondary role, probably via hydrogen trapping mechanisms and enhanced intergranular embrittlement. The presence and size of the precipitate free zones (PFZ) are of minor importance to these researchers.

3.0 Experimental Procedures

The corrosion properties of the alloys 7178-T6 and 7075-T651 were studied by potentiodynamic and potentiostatic techniques. Constituent particles were observed to be the initiation sites of pits for these alloys. The role of the constituent particles in corrosion processes was explored by galvanic studies where the intermetallic phases were electrically coupled to pure aluminum. Galvanic experiments were also conducted on a disassembled riveted wing joint where steel rivets were used to fasten the aluminum panel. Controlled potential constant load and constant displacement stress corrosion cracking tests were conducted to reproduce the phenomenon of intergranular stress corrosion cracking initiating from corrosion pits.

3.1 Material

3.1.1 Commercial Materials

As discussed earlier, aluminum alloys 7178 and 7075 are the main focus of this research program. Alloy 7178 is a high strength variant of 7075 and was used in airframes such as the KC-135 and B52. An understanding of the behavior of this material will allow for better extrapolation of current airframe life predictions. Alloy 7075 has a higher fracture toughness and is less susceptible to environmental degradation due to SCC. However, the constituent particle chemistry is similar for both alloys.

Alloy 7178 material was obtained as part of a replaced wing panel from a KC-135 aircraft. The panel was obtained from the U.S. Air Force Air Logistic Center at Oklahoma City and contained obvious corrosion damage at rivet attachment points. The material was identified as being in the T6 condition. Alloy 7075 was obtained in plate form (38mm thick) from a commercial source in the T651 condition. The composition of these materials is listed in Table 3.1.

Table 3.1. Chemical composition (wt.%) of the plates used.

Sample	Al	Zn	Mg	Cu	Fe	Si	Cr	Ni	Mn	Ti
7178-T6	90.0	6.38	2.21	1.86	0.23	0.09	0.18	0.005	0.043	0.047
7075-T651	90.4	5.33	2.20	1.47	0.25	0.11	0.18	0.004	0.083	0.040

In addition to the KC-135 panel, a B52 wing panel section was obtained from Boeing - Wichita. The wing panel contained obvious corrosion damage associated with riveted joint areas. Two of the joints, where steel rivets were used to fasten the aluminum panel, were disassembled and used for electrochemical studies. These disassembled joints are presented in Figures 3.1 and 3.2. No corrosion was observed in joint #1 (Figure 3.1). Two areas of corrosion, labeled Area I and II, can be found on the plate from joint #2 (Figure 3.2 b, c, and d). Exfoliation and pits were observed on the countersink area of the aluminum panel. The rivet from joint #2, however, was not corroded (Figure 3.2 a). Samples were cut from the plates and rivets for electrochemical studies. EDX analyses were conducted to identify the composition of the rivets and plates. The results of these analyses are tabulated in Table 3.2.

High purity aluminum (99.999%) was obtained in rod form for electrochemical studies.

The labeling scheme used to identify the orientations and planes of the alloys is shown in Figure 3.3.

3.1.2 Intermetallic Phases

Five types of commonly occurring constituent particles in aluminum alloys were manufactured in bulk by the hot isostatic press (HIP) process. The composition of these phases was chosen based on analysis of precipitates in the 7178 and 7075 materials described above. High purity elemental powders were used as the starting material. The powders were consolidated in steel cans with 0.5" inside diameter, evacuated, sealed, and hipped. Each sample was then sectioned and polished. The finished products were fully dense. The extent of chemical homogeneity was established by energy dispersive X-ray spectroscopy (EDX) mapping of the polished surface. The target and actual composition of the hipped samples are listed in Table 3.3. X-ray diffraction was used for phase identification. The obtained spectra were compared to known data and the results are tabulated in Table 3.4. Al_3Fe (θ) is listed as a "very complex end-centered monoclinic" structure [68] with 100 atoms to the unit cell [69] and not enough is known about the phase to perform a rigorous calculation of the diffraction pattern from first principles.

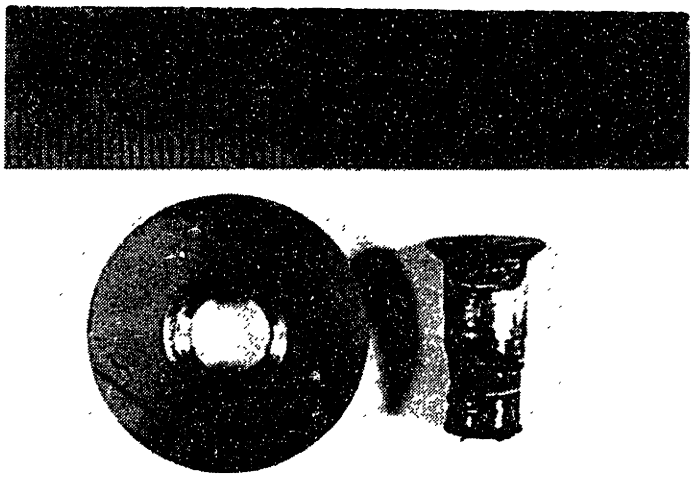

Figure 3.1. Picture showing rivet and plate from joint #1.

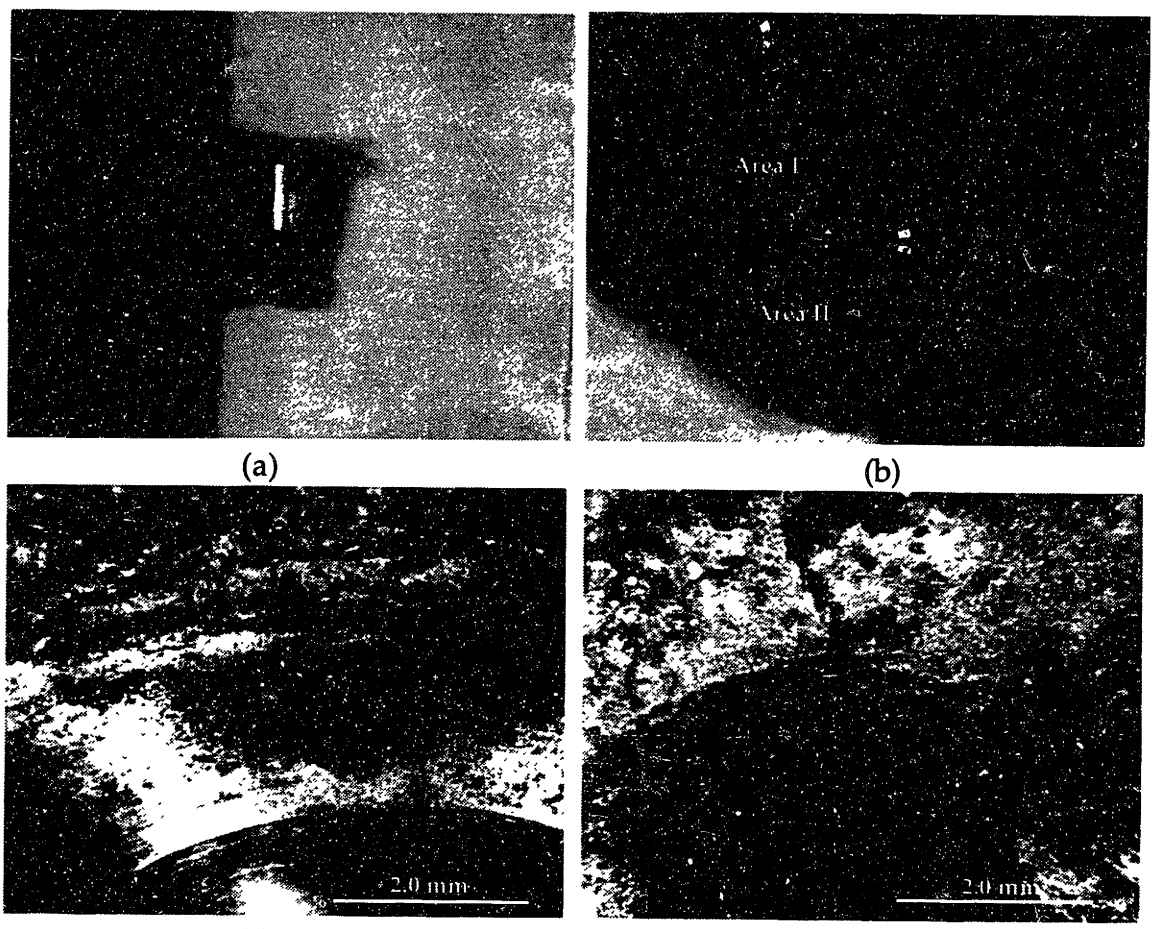

(a) (b) (c) (d)

Figure 3.2. (a) Rivet and (b) plate from joint #2. Corrosion can be observed in (c) Areas I and (d) II.

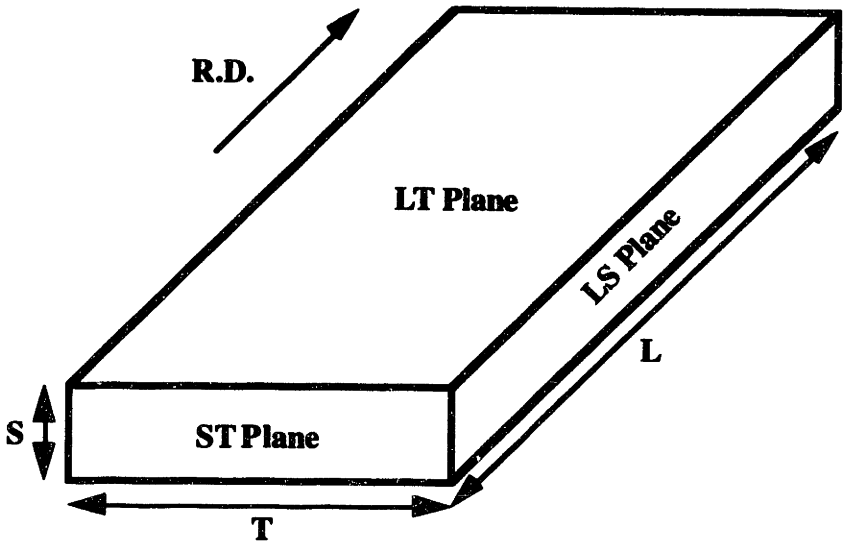

Figure 3.3. Labeling scheme used for directions and planes.

Table 3.2. Composition (wt.%) of the plate and rivets from the dismantled joints.

Material	Al	Cu	Zn	Mg	Fe	Si	Mn	Cr
Plate #2	89.3	2.1	7.1	1.5				
Rivet #1					98.3	0.3	0.8	0.6
Rivet #2					98.7	0.3	0.9	

Table 3.3. Actual and target compositions (wt%) of the five aluminum intermetallic samples.

Material	Al	Cu	Zn	Fe
Al_2Cu	51.9 (Bal)	48.1 (53-54)		
Al_2Cu + 1.5% Zn	50.8 (Bal)	48.5 (53-54)	0.7 (1.5)	
Al_2Cu + 2.5% Zn	50.2 (Bal)	48.2 (53-54)	1.6 (2.5)	
$Al_6(Fe,Cu)$	72.8 (Bal)	5.9 (7-8)		21.3 (22-25)
Al_3Fe	62.1 (Bal)			37.9 (39-41)

Table 3.4. Results of x-ray diffraction qualitative phase analysis of the intermetallic alloys.

Sample	Major Phase	Minor Phase
Al_2Cu	$CuAl_2$ (Khatyrkite)	
Al_2Cu + 1.5% Zn	$CuAl_2$ (Khatyrkite)	Cu_2AlZn
Al_2Cu + 2.5% Zn	$CuAl_2$ (Khatyrkite)	Cu_2AlZn
$Al_6(Fe,Cu)$	Al_7Cu_2Fe	
Al_3Fe	N/A	N/A

3.2 Experimental Environments

The environments chosen for this research work were designed to: (1) simulate the possible ranges of oxygen and chloride concentrations likely to be seen in service, and (2) allow for comparison with other experimental data from the literature. The major environmental variables were the chloride concentration (0.1M, 0.3M, 1.0M, 3.0M and 5.0M) and oxygen concentration (deaerated with nitrogen gas and air saturated). Tests were also carried out in ASTM G69 (58.5±0.1g NaCl and 9±1mL of H_2O_2 per 1L of solution) and G34 (234g NaCl, 50g KNO_3, and 6.3ml of 70% HNO_3 per 1L of solution) environments. The G69 and G34 solutions are 1.0M and 4.0M with respect to NaCl concentration. The G34 solution has an apparent pH of 0.4. Some tests were conducted in sulfate solutions to evaluate the effect of chloride ions. Test temperature ranged from 298 to 323K.

The choice of chloride concentration range was based on a desire to simulate more relevant environments - appropriate to a marine source environment. It was felt that crevice chloride concentrations on the order of 0.1M were not unreasonable to expect in service. The chloride concentration plays a critical role in the pitting of aluminum alloys.

The choice of oxygen concentrations was based on a desire to simulate conditions of air exposure but to allow for crevice conditions where oxygen consumption would be expected. The role of the oxygen reduction reaction in polarizing the material above the pitting potential was felt to be a critical factor in the experimental program.

A standard G69 solution was used for some of the tests in order to allow for

comparison with the data in published literature. However, for most of the electrochemical studies, the potential, as measured during a G69 exposure and achieved chemically, was achieved using potentiostatic methods. In this way, the condition of a G69 exposure could be duplicated in a less aggressive environment (chemically) that was more appropriate to actual service.

The temperature range was chosen to simulate actual service temperatures during non-flight conditions.

3.3 Microscopy

3.3.1 Optical Microscopy

Samples were cut from the 7075-T651 and 7178-T6 plate to confirm the orientation of the material. The samples were ground and polished with diamond paste. The grain boundaries were revealed by a modified Keller's reagent (2.5 ml HNO_3, 1.0 ml HCl, 1.0 ml HF, and 95 ml water).[70]

3.3.2 SEM Microscopy

The Topcon ABT-150S, equipped with a Noran Voyager II X-ray Quantitative Microanalysis System, was used for all scanning electron microscopy (SEM) work and energy dispersive X-ray (EDX) analysis. The accelerating voltage varied between 20 and 40kV. Secondary and back scattered electron imaging modes were used.

3.4 Electrochemical Studies

Samples, approximately $1cm^2$ in area, were cut from the aluminum alloy plates. In the case of the intermetallic alloys, a section roughly 1.5cm thick was first cut from the HIP can. A small cyclinder approximately 0.8 cm in diameter was then removed by EDM. Electrical lead wires were attached to the samples and the samples were then mounted in resin.

Each specimen was ground and polished to a mirror finish. 3μm diamond paste was used for the final polish. The specimen was then rinsed with deionized water, cleaned in isopropanol alcohol, and masked along its edges with resin prior to testing. The exposed area on the sample was measured.

Electrolytes used in all the studies were made from reagent grade chemicals and deionized water. Unless stated otherwise, all electrolytes used were deaerated with nitrogen gas (less than 5ppm oxygen) for a minimum of 45 minutes before testing. In the case of aerated studies, a gas mixture of 20% oxygen in argon was bubbled through the electrolytes for a minimum of 1 hour prior to testing.

Two potentiostats, a EG&G 173 with a 276 interface and a EG&G 273, were used for all the experiments. A programmable electrometer (Keithley 617) was used as a high impedance voltmeter for free corrosion potential measurements.

All electrochemical potential measurements were made via Luggin probes. Saturated calomel electrodes (SCE) were used as the reference in chloride environments. In sulfate solutions, mercury / mercurous sulfate (Hg/Hg_2SO_4) electrodes served as the reference. The readings were then converted to the SCE scale.

3.4.1 Free Corrosion Potential Measurement

Experiments were conducted in accordance to ASTM G69 ("Standard Practice for Measurement of Corrosion Potentials of Aluminum Alloys") and ASTM G34 ("Exfoliation Corrosion Susceptibility in 2XXX and 7XXX Series Aluminum Alloys, EXCO Test"). The free corrosion potential was monitored continuously by the high impedance voltmeter and recorded by computer.

3.4.2 Potentiodynamic Experiments

Dynamic polarization scans were started within 5 minutes of immersing the specimen into the electrolyte. The scans were initiated from the open circuit potential and the potential was scanned in the noble direction at a rate of 10mV/min. When the current density reached $5mA/cm^2$, the experiment was terminated. Experiments were also conducted at 1mV/min to study the effect of scan rate. Dynamic polarization studies were conducted in 0.1M, 0.3M, 1.0M, 3.0M, and 5.0M (saturation at 298K) NaCl solutions to study the effects of chloride ion concentration. Test temperature varied from 298, 308, 318 to 323K. Water baths were used to maintain the test temperature to within $\pm 0.5^{\circ}C$ of the target. The breakdown potentials reported are the

averages of at least two experiments. The average scatter in the critical potentials reported is 4mV.

Cyclic polarization experiments were also conducted to examine the repassivation behavior of these materials. The initial conditions for cyclic polarization experiments were identical to those of dynamic polarization studies. In the case of cyclic polarization experiments, the direction of polarization was reversed when the current density reached $5mA/cm^2$. The scan rate was maintained at 10mV/min. The test was terminated when the material had repassivated.

3.4.3 Potentiostatic Experiments

Potentiostatic experiments were conducted to identify the corrosion sites associated with a particular breakdown potential and environment. The potential was maintained constant until a charge density of approximately $3C/cm^2$ was reached. This ensures significant corrosion had occurred and the breakdown sites could easily be identified. Energy dispersive x-ray spectroscopy (EDX) studies were conducted on various second phase particles found on the corroded surfaces.

3.4.4 Galvanic Corrosion Experiments

Two specimens were immersed into the corrosion cell approximately 2cm apart with the polished surfaces facing each other. The Luggin probe was positioned roughly in the middle of the two specimens. The potentiostat functioned as a zero resistance ammeter (ZRA) in these experiments and the galvanic current was recorded. Concurrently, the high impedance voltmeter monitored the free corrosion potential.

3.5 Mechanical / Environmental Behavior Testing

As discussed earlier, airframe degradation often occurs in the form of pitting / exfoliation attack in occluded area followed by crack initiation in stressed regions. Crack propagation can be either by static stress corrosion cracking or by fatigue (assisted by the environment). The role of the corrosion damage is often to provide both the aggressive environment and the stress concentrator required for crack initiation.

Mechanical/environmental behavior testing was conducted to characterize the initiation process. Two types of tests were employed, constant load and constant displacement. Additionally, tensile tests were performed to characterize the strength of the materials.

3.5.1 Tensile Tests

The configuration of the specimens used for tensile tests is depicted in Figure 3.4. It consists of a round bar with a square gage section. The sides of the square section correspond to the principal directions of the material. The 0.2% offset yield stress was computed for each specimen. At least two specimens were used for each material and orientation. Fracture surfaces were examined in SEM and representative fractographs obtained.

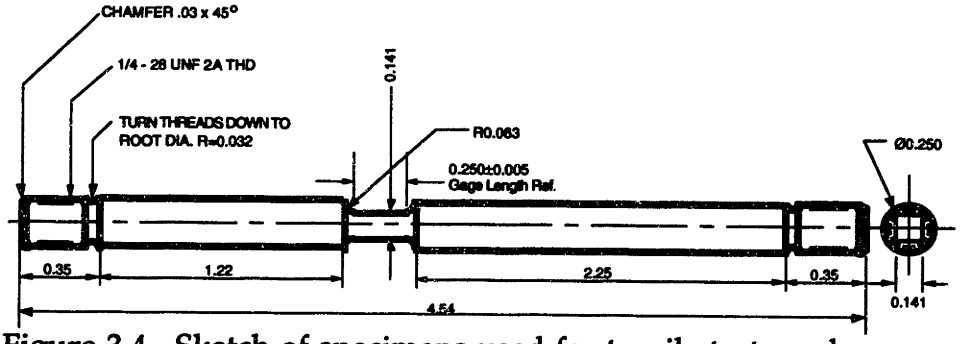

Figure 3.4. Sketch of specimens used for tensile tests and constant load SCC tests. The dimensions are in inches.

3.5.2 Stress Corrosion Cracking Tests

3.5.2.1 Constant Load

The specimens used for constant load SCC tests were identical to those used for the tensile tests. The dimensions of the specimens are shown in Figure 3.4 above. Most of the specimen was masked off with resin during SCC tests. Only the gage area was exposed to the environment. A gas tight 10 liter bottle was used as the electrolyte reservoir. The corrosion cell, which holds roughly 150cc of electrolyte, was machined from Lexan. The test cell is illustrated in Figures 3.5 and 3.6. A Cole Parmer Master Flex pump was used to circulate the electrolyte between the reservoir and the corrosion cell. Deaeration of the electrolyte was accomplished by bubbling nitrogen gas through the reservoir. A nitrogen gas cover inside the corrosion cell maintained the deaeration. A

lever arm creep tester was used to apply the constant load.

The electrochemical potential was maintained by a potentiostat during all tests. A Luggin probe, attached to the side of the corrosion cell, was used to measure the potential. A platinum foil, roughly 6cm^2 in area, served as the counter electrode.

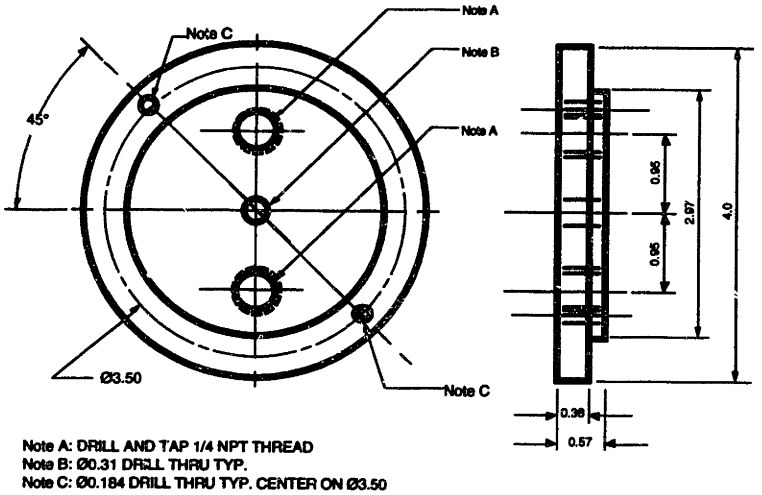

Figure 3.5. Corrosion cell lid used for constant load experiments.

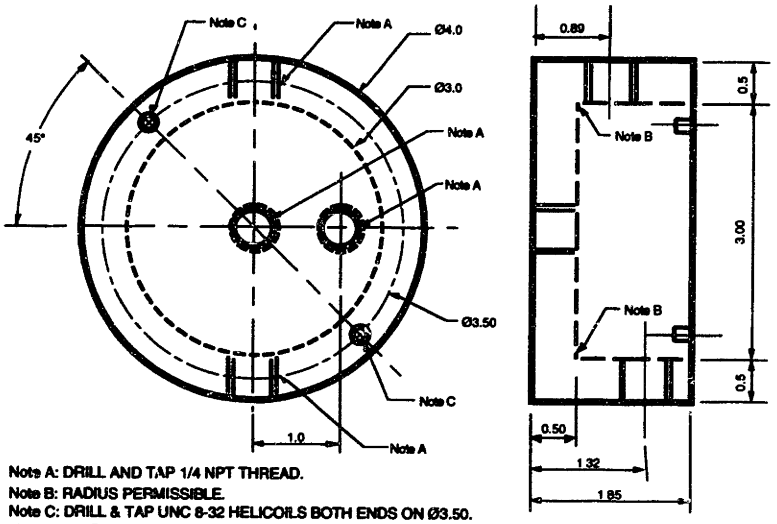

Figure 3.6. Corrosion cell bottom used for constant load experiments.

Electrolyte was first pumped into the cell. The constant electrochemical potential was established by the potentiostat and the load was finally applied.

3.5.2.2 Constant Displacement

The specimens used for constant displacement tests are 4.5" long 0.141" square bars. These tests were conducted in a 316 stainless steel four point bend fixture shown in Figure 3.7. The load was applied by adjusting a stainless steel screw on the bottom of the fixture. Only a small portion of the gage section was exposed to the environment; most of the specimen was masked off with resin. Strain gages were attached to the specimen surface under tension between the two inside supports. Two independent 1/4 bridge strain gage circuits were used for each specimen to assure the accuracy of the measurements.

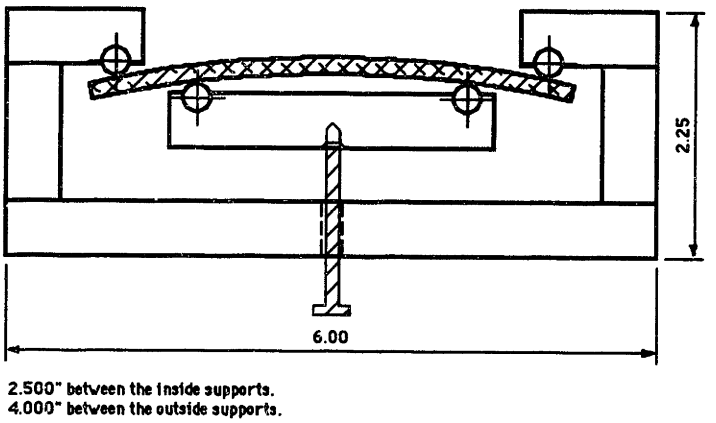

Figure 3.7. Schematic of a four point bend fixture. The dimensions are in inches.

Since the maximum stress never exceeded yield, Hooke's law for uniaxial stress applies. In the elastic range, the normal stress varies linearly with the distance from the neutral surface. [71] This is shown schematically in Figure 3.8. The bending moment is calculated by:

$$\sigma_m = \frac{M}{S} \tag{3.1}$$

where

σ_m : maximum absolute value of stress
M : bending moment
S : elastic section modulus

The elastic section modulus of a beam with rectangular cross sectional width b and depth h is:

$$S = \frac{1}{6}bh^2 \qquad (3.2)$$

The tensile strain on the surface on the specimen was monitored by the strain gages. Since the stress never exceeded yield, the maximum stress (σ_m) can be obtained directly from these strain measurements. With b and h known, the bending moment, M can be calculated. The calculated bending moment is used for stress intensity factor calculations.

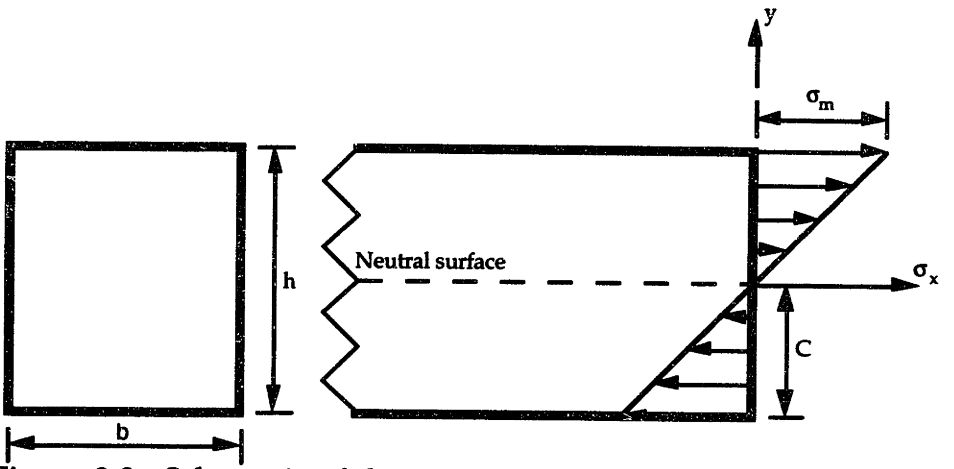

Figure 3.8. Schematic of the stress state for a bending specimen.

The corrosion cell used in the four point bend tests consisted of a 9.0"(L) x 7.5" (W) x 4.3" (H) Lexan box. The electrolyte reservoir and circulation pump used for the constant load tests were also used in four point bend tests. Nitrogen cover gas, electrolyte circulation, and Luggin probe attachment were accomplished via various ports on the corrosion cell. Four test fixtures were attached to the perimeter of the corrosion cell which allowed four specimens to be tested simultaneously.

4.0 Results

4.1 Metallographic Results

Figures 4.1 and 4.2 show the strong grain shape anisotropy common in these materials. The grain boundaries are revealed by a modified Keller's etchant.

Figure 4.1. Optical micrograph showing the strong orientation effect in the 7075-T651 plate.

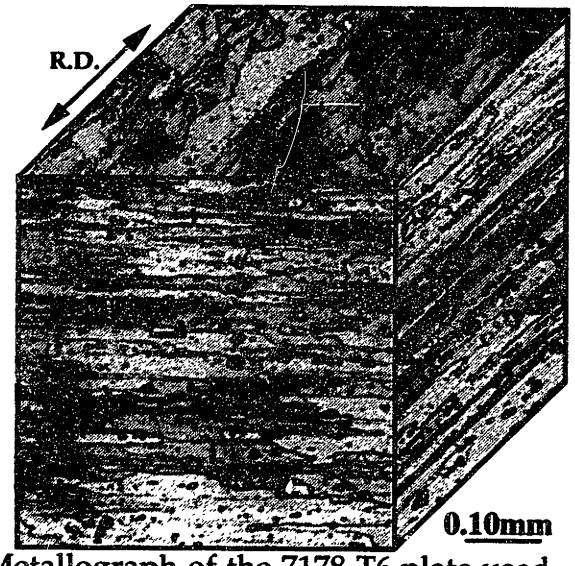

Figure 4.2. Metallograph of the 7178-T6 plate used. The arrow indicates the rolling direction of the plate.

4.2 Electrochemistry

Unless stated otherwise, all electrochemical potentials reported are referenced to the saturated calomel electrode (SCE) scale. Conversion to the standard hydrogen scale (SHE) can be accomplished by adding 0.2416V to the SCE readings.

$$E(V, SHE) = E(V, SCE) + 0.2416 \quad (4.1)$$

4.2.1 Corrosion Potential Measurements

Figure 4.3 shows the potential vs. time for a G69 exposure. The average corrosion potential for 7075-T651 and 7178-T6 in the last 30 minutes of an 1 hour ASTM-G69 test is -0.726 and -0.736V respectively. It is likely that the changes in potential with time is due to the deterioration in the strength of the hydrogen peroxide added to the electrolyte. In other words, the amount of dissolved oxygen in the solution decreased with time.

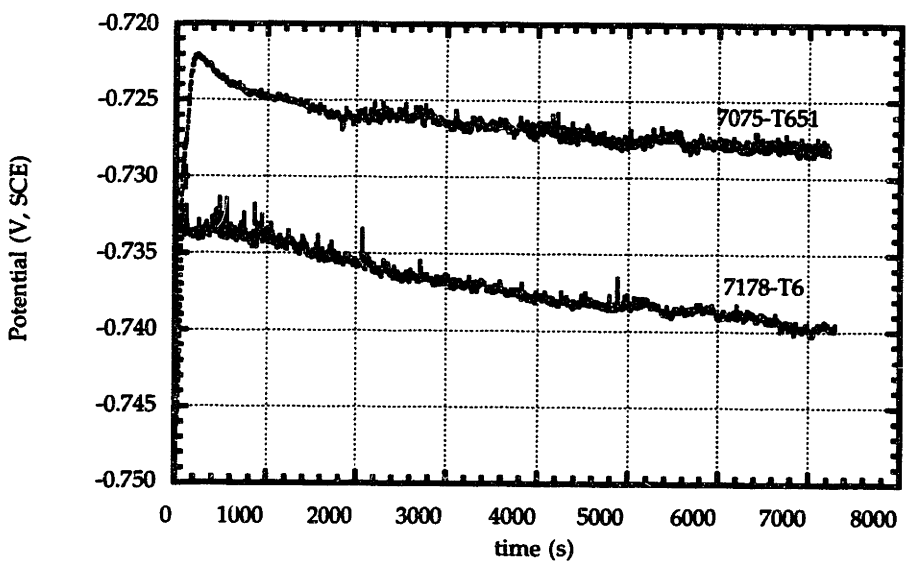

Figure 4.3. Changes in corrosion potential for 7075-T651 and 7178-T6 during ASTM G69 test.

The corrosion potential for these materials was also recorded during ASTM G34 exfoliation susceptibility tests. These are shown in Figure 4.4 The average of the free corrosion potential in the last hour of a 48 hr test is -0.704

and -0.713V for 7075-T651 and 7178-T6 respectively. The corrosion potential for 7178-T6 in both G69 and G34 tests are more active than that of 7075-T651.

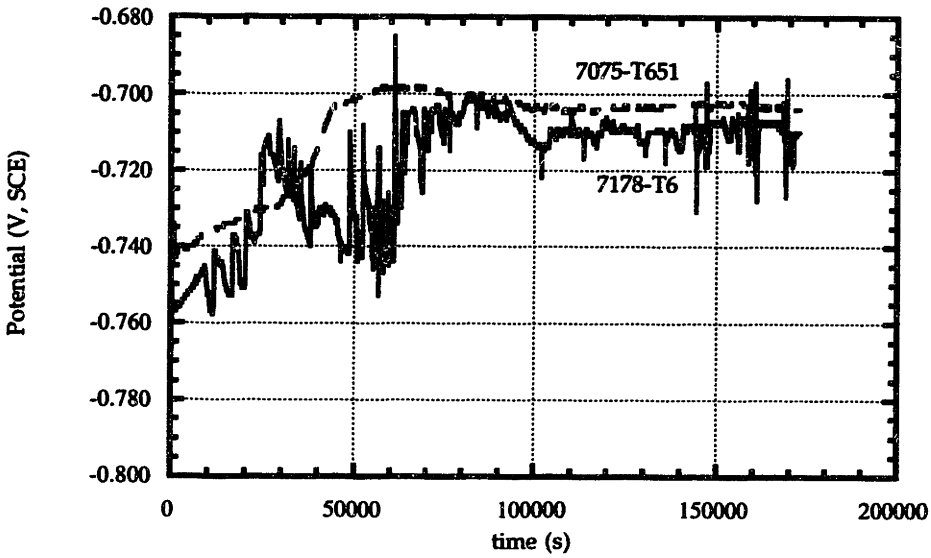

Figure 4.4. Free corrosion potential vs. time for 7075-T651 and 7178-T6 during ASTM G34 test.

The samples from both materials were sectioned after the exfoliation susceptibility test to determine the extent of exfoliation corrosion. Figures 4.5 and 4.6 show the results of this analysis. It is apparent that significant corrosion had occurred in these materials.

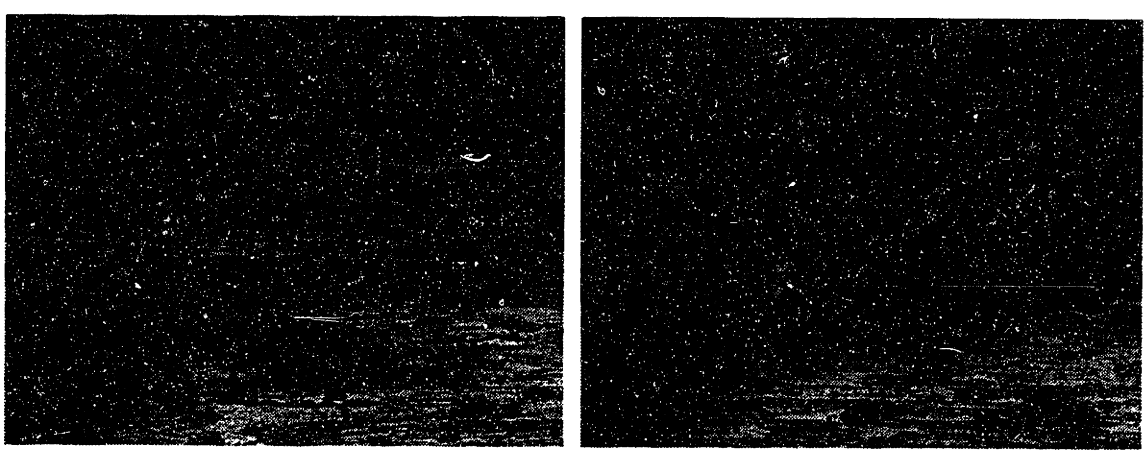

(a) (b)

Figure 4.5. Cross section of 7178-T6 sample after ASTM G34 test.

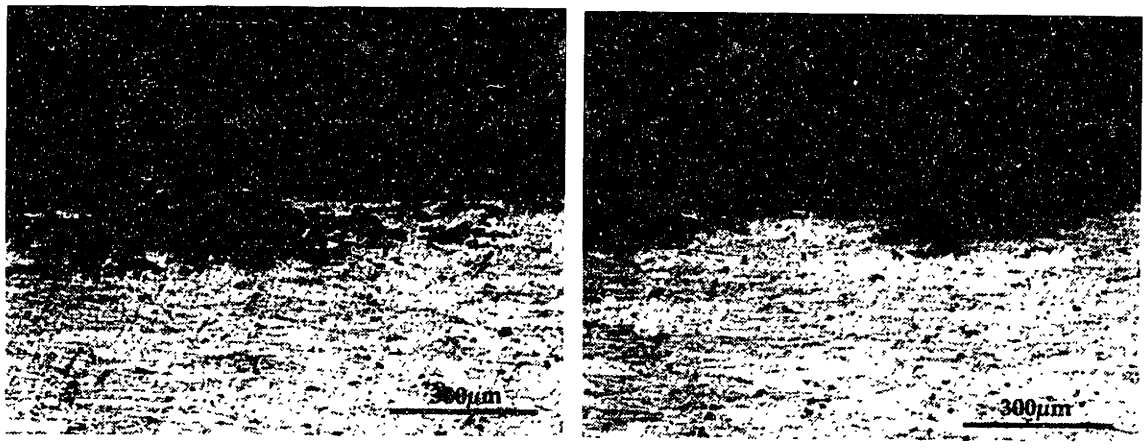

(a) (b)

Figure 4.6. Cross section of 7075-T651 sample after ASTM G34 test.

4.2.2 Identification of Breakdown Potentials

As illustrated in Section 1.1.2, aluminum alloys are protected by a surface film in many environments. However, in the presence of chloride ions and/or at potentials more active than the critical "breakdown" potentials, film breakdown occurs locally and accelerated attack can occur. The accelerated attack can take the form of pitting and/or intergranular attack and was characterized by a potential above which a large increase in current density was observed. The type of the localized corrosion which was responsible for the current density increase was confirmed by metallographic analysis of the polarized sample.

4.2.2.1 7178-T6 Material

Figure 4.7 shows a typical polarization plot for 7178-T6 material in chloride environment. Two breakdown potentials, a "lower" and an "upper" breakdown potential, were identified. In Figure 4.7, the breakdown potentials are at -0.701V and -0.656V.

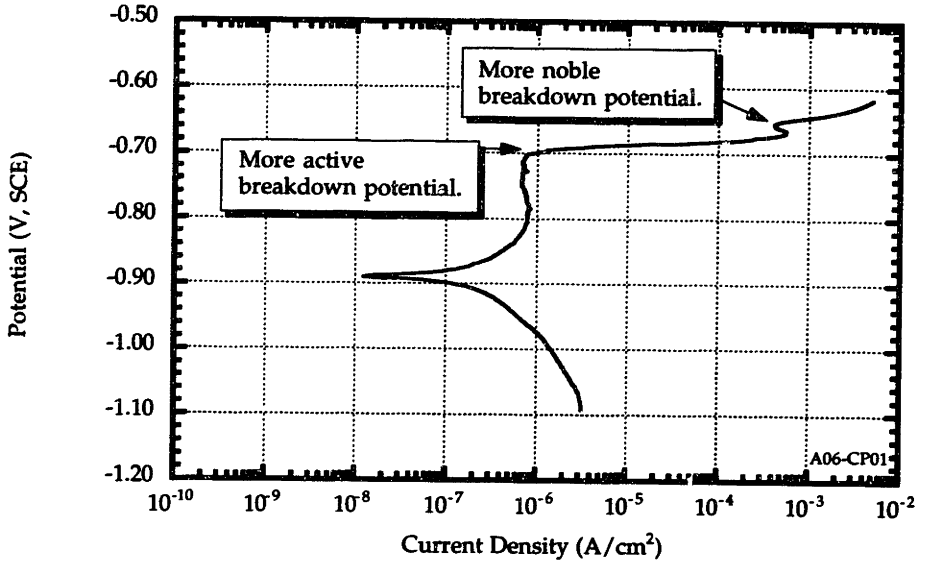

Figure 4.7. Dynamic polarization plot for 7178-T6 in 0.1M NaCl at 298K.

Static polarization experiments were conducted to identify the corrosion sites associated with the breakdown potentials. Figure 4.8 illustrates the typical response of 7178-T6 after static polarization at -0.670V. This potential is above the lower breakdown potential of -0.656V but below the upper breakdown potential of -0.701V. Two different types of second phase particles were observed. EDX analyses were conducted on these particles and the details are shown in Appendix A. The particles shown in Figures 4.8 b and c are rich in copper while Figure 4.8 d shows a silicon rich particle. The arrow in the figures indicates the particle whose EDX spectrum is shown. Because of their size and composition, these particles were classified as constituent particles. The interface between the copper rich particle and the matrix was corroded and is thus the source of the increased current density. In some cases, only dimples were observed. No corrosion was observed around silicon rich particles.

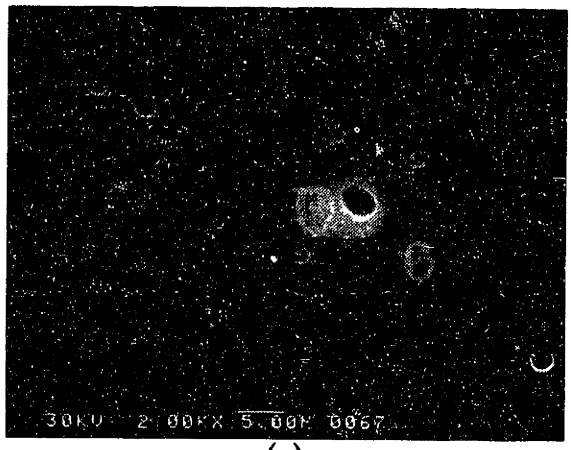
30KV 2.00KX 5.00μ 0067

(a)

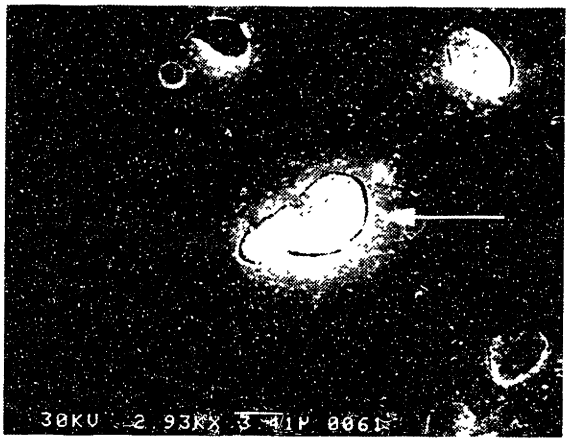
30KV 2.93KX 3.41μ 0061

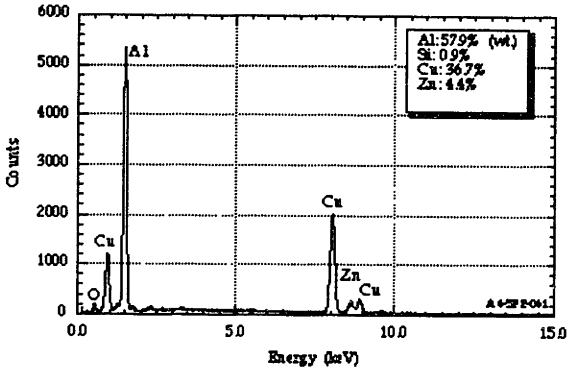
Al:57.9% (wt.)
Si:0.9%
Cu:36.7%
Zn:4.4%
Al
Cu
Cu
Zn
Cu
O
Counts
Energy (keV)
0.0
5.0
10.0
15.0
0
1000
2000
3000
4000
5000
6000

(b)

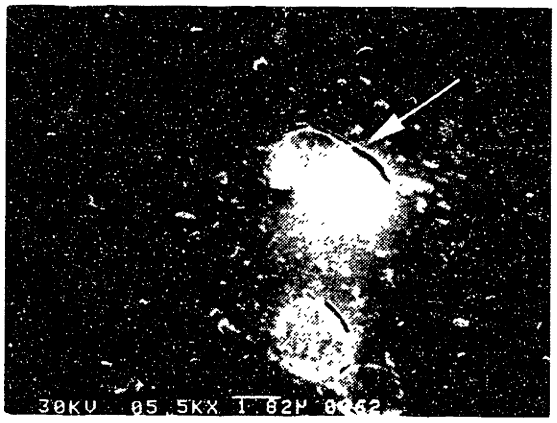
30KV 05.5KX 1.82μ

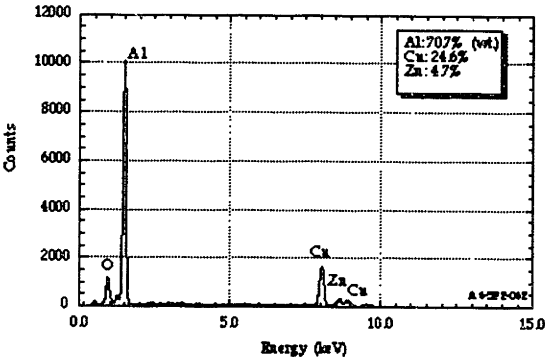
Al:70.7% (wt.)
Cu:24.6%
Zn:4.7%
Al
Cu
Zn
Cu
O
Counts
Energy (keV)
0.0
5.0
10.0
15.0
0
2000
4000
6000
8000
10000
12000

(c)

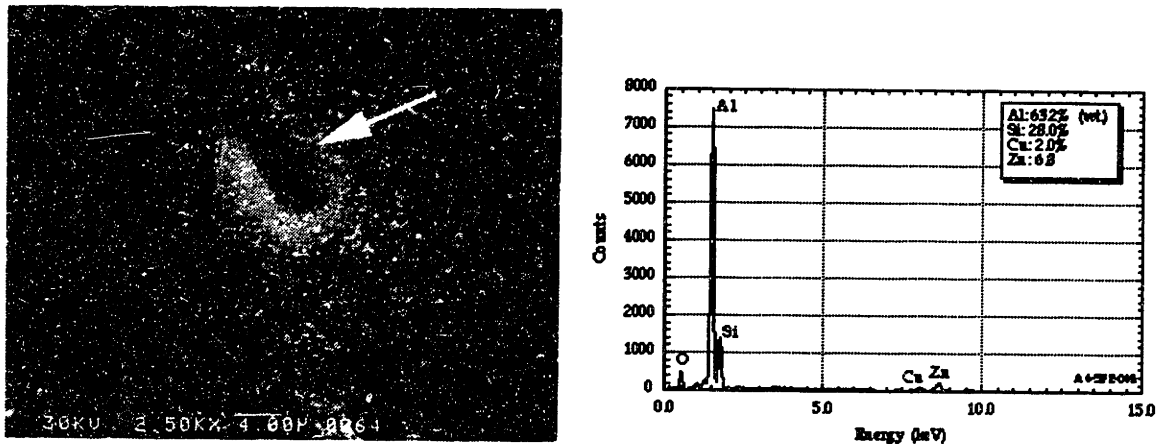

(d)

Figure 4.8. SEM images of corroded surface for 7178-T6 after static polarization at -0.670V in 0.1M NaCl at 298K. The arrow points to the particle whose EDX spectrum is shown.

Intergranular attack (IGA) was the dominant form of corrosion for 7178-T6 after static polarization above the upper breakdown potentials at -0.650V. This is shown in Figures 4.9 and 4.10. Large scale pitting which originated from grain boundaries (Figure 4.9 a and b), and interface dissolution around second phase particles (Figure 4.9 c and 4.10 d) was also observed.

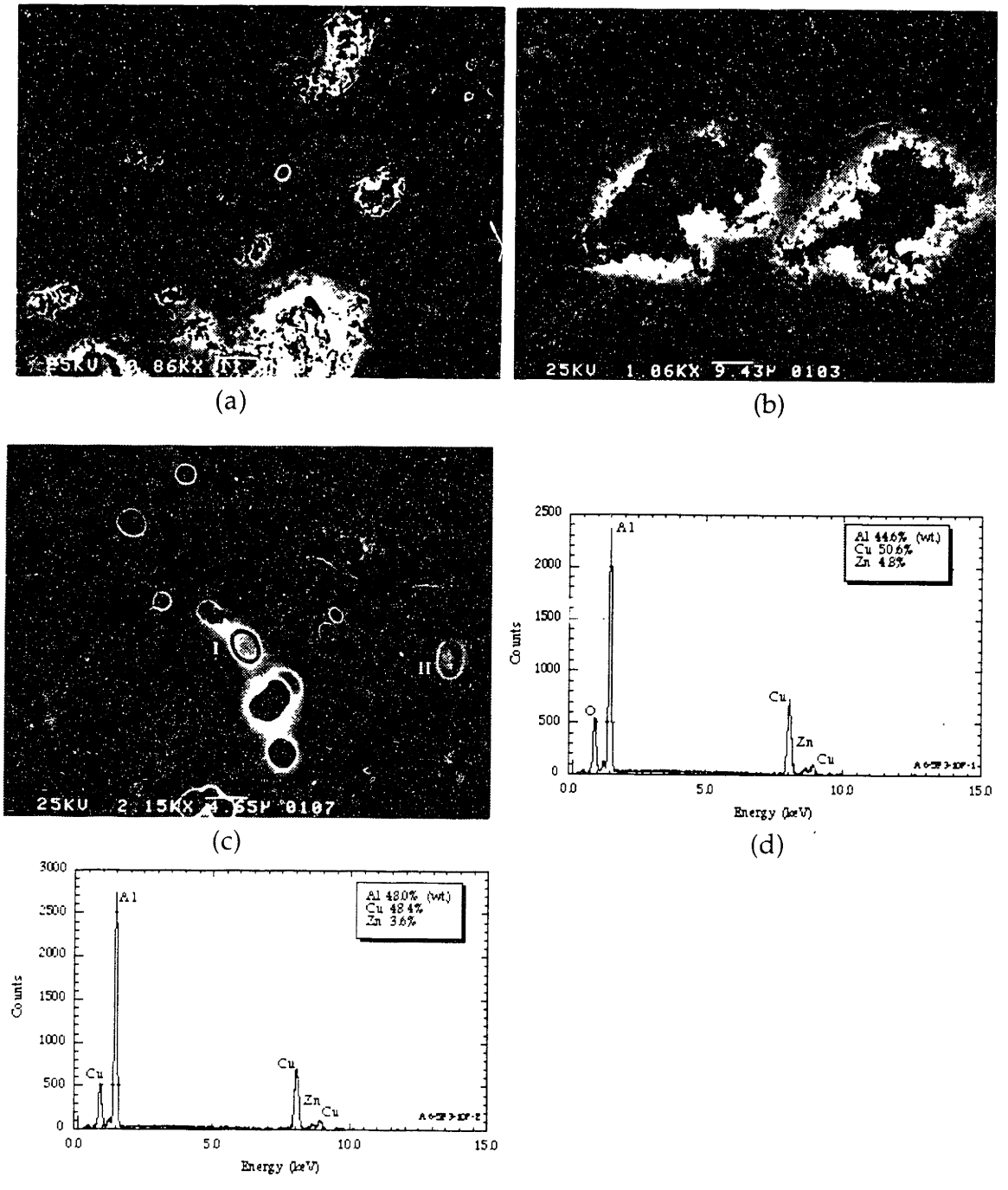

Figure 4.9. SEM micrographs of 7178-T6 after static polarization experiment at -0.650V in 0.1M NaCl at 298K. The EDX spectrums for the particles labeled I and II in (c) are shown in (d) and (e) respectively.

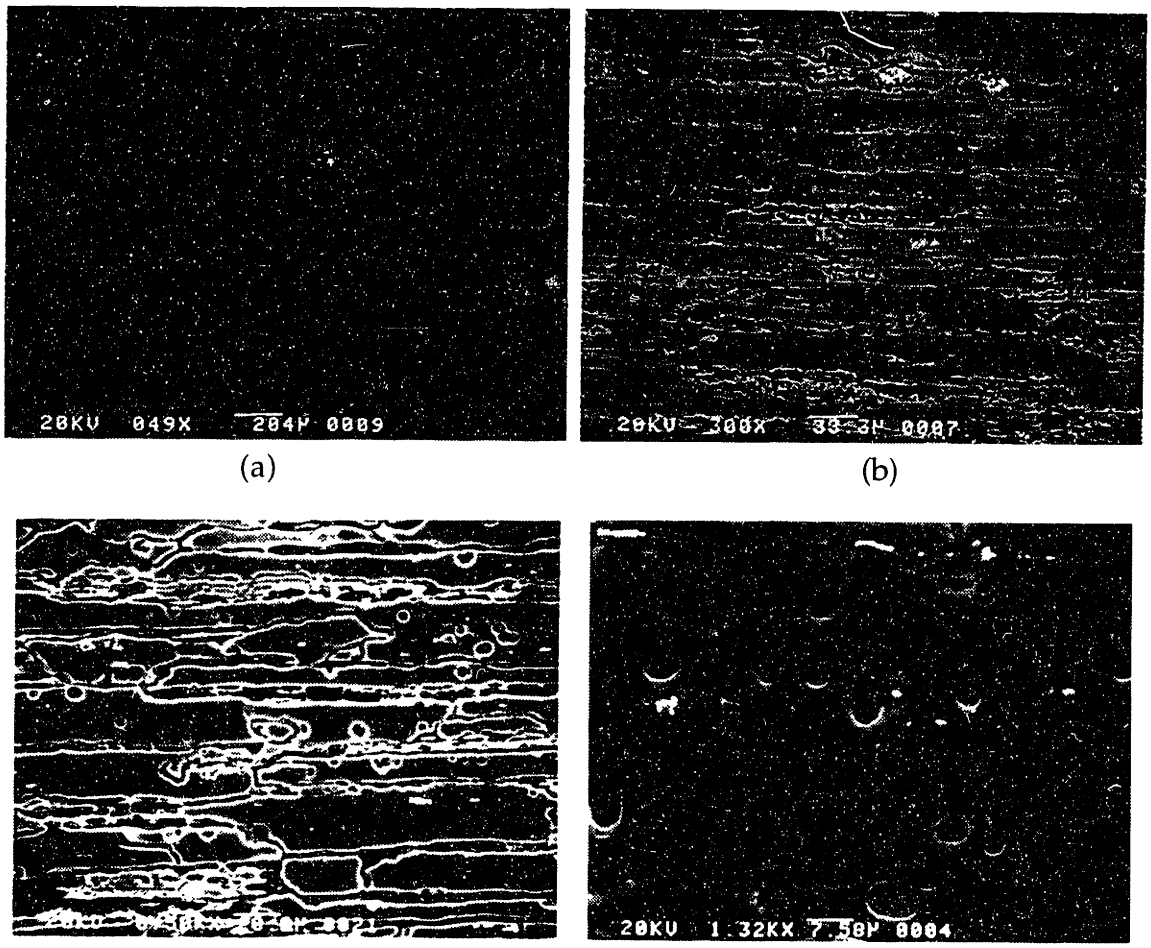

(a) (b)

(c) (d)

Figure 4.10. 7178-T6 ST plane after static polarization at -0.650V in 0.1M NaCl at 298K.

4.2.2.2 7075-T651 Material

As with the 7178-T6 material, two breakdown potentials were observed, a more active breakdown at -0.691V and a more noble breakdown at -0.651V. Figures 4.11 and 4.12 show the surfaces of 7075-T651 after polarization above these potentials. The increase in corrosion current density at the more active breakdown potential is associated with interface corrosion of second phase particles in the matrix. The increase in current density above the more noble breakdown potential is associated with intergranular attack.

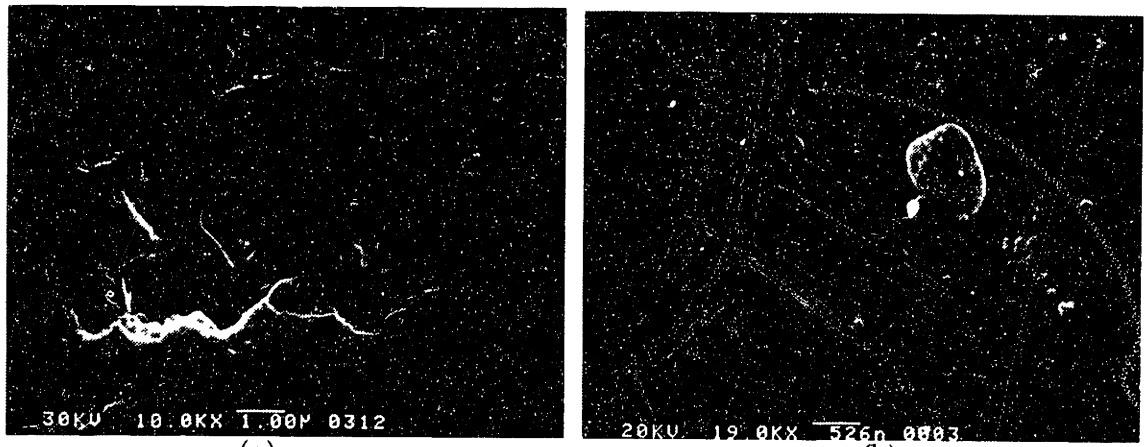

(a) (b)

Figure 4.11. 7075-T651 maintained between the critical potentials, showing interface corrosion around second phase particles.

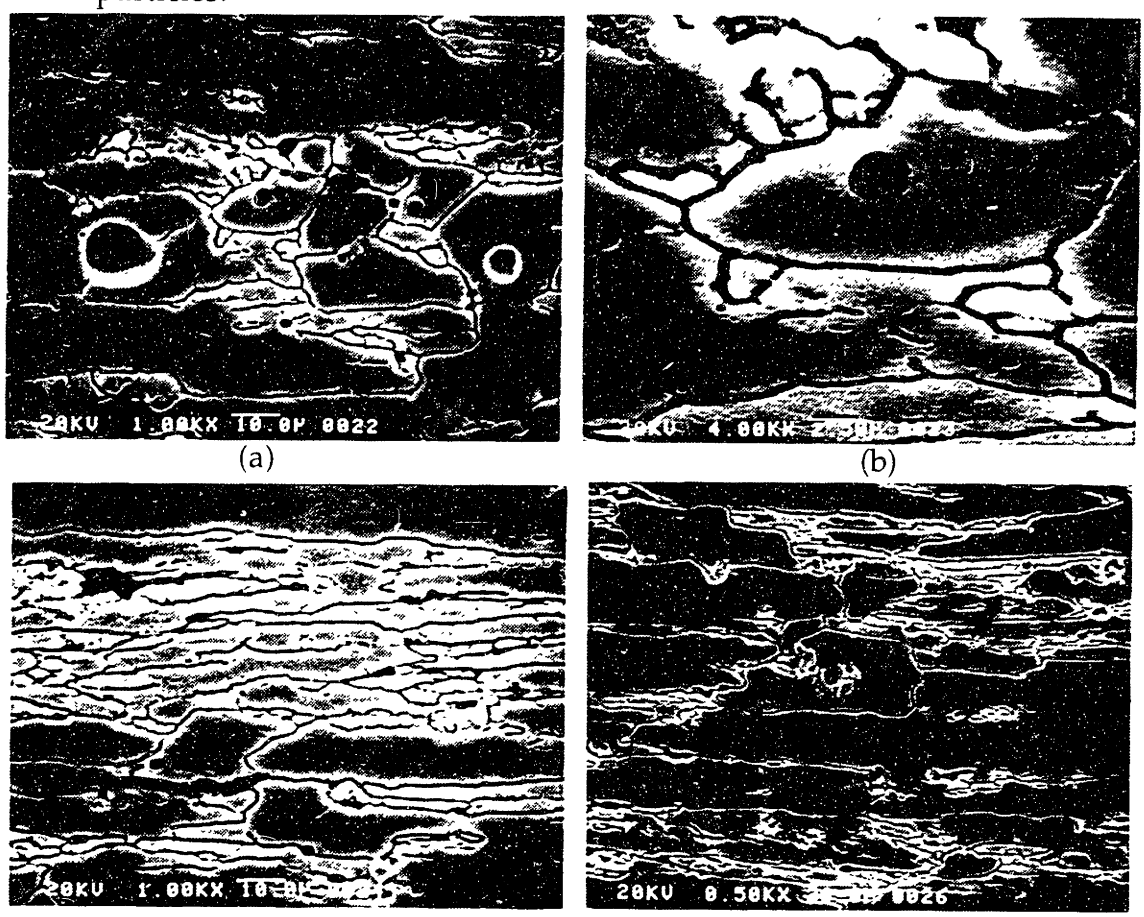

(a) (b)

(c) (d)

Figure 4.12. SEM micrographs of 7075-T651 after static polarization at -0.650V in 0.1M NaCl at 298K showing intergranular attack and dissolution around second phase particles.

It can therefore be concluded, for both 7075-T651 and 7178-T6, that the more active (more negative) breakdown potential is associated with interface corrosion around constituent particles which leads to pitting while the more noble breakdown potential is related to intergranular corrosion. For future reference, the lower (more active) breakdown potential will be referred to as E_{pit} while the upper (more noble) breakdown potential will be referred to as E_{iga}.

Figures 4.13 and 4.14 show the results of polarization in sodium sulfate solution for 7178-T6 and 7075-T651 respectively. In each case, the observed behavior is of a transition to passive behavior with no subsequent breakdown at noble potentials. These results confirm the role of chloride ion in the film breakdown process.

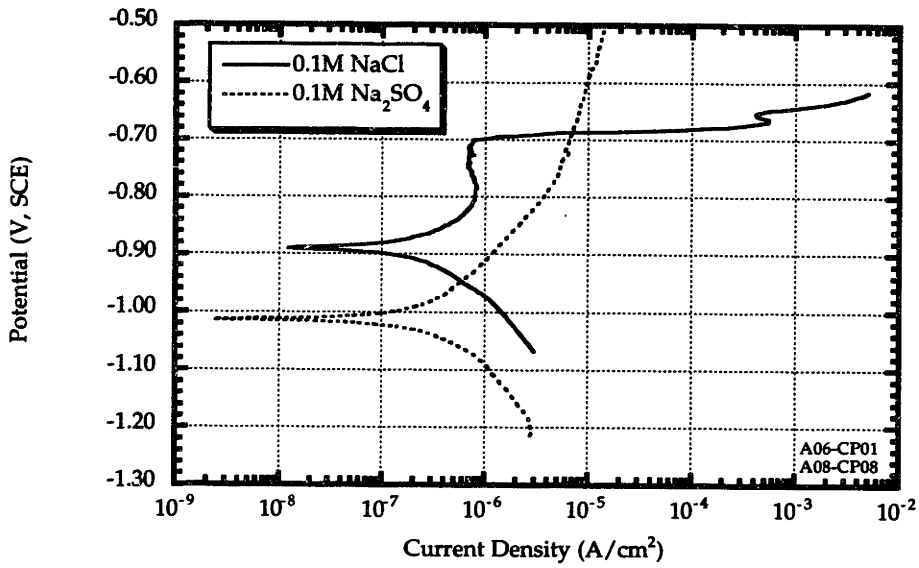

Figure 4.13. Comparison of polarization results of 7178-T6 in NaCl and Na_2SO_4.

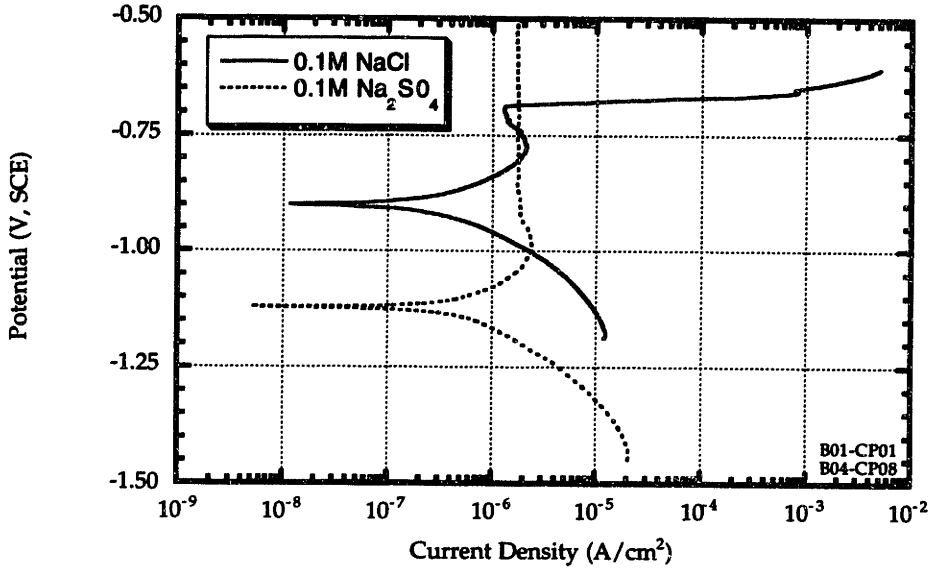

Figure 4.14. Comparison of polarization results of 7075-T651 in NaCl and Na_2SO_4.

4.2.3 Effect of Scan Rate on the Breakdown Potentials

Dynamic polarization experiments were conducted in 0.1M NaCl solutions at 298K with scan rates of 1mV/min and 10mV/min. The results are presented in Figures 4.15 and 4.16. The breakdown potentials for the two sets of experiments are virtually identical.

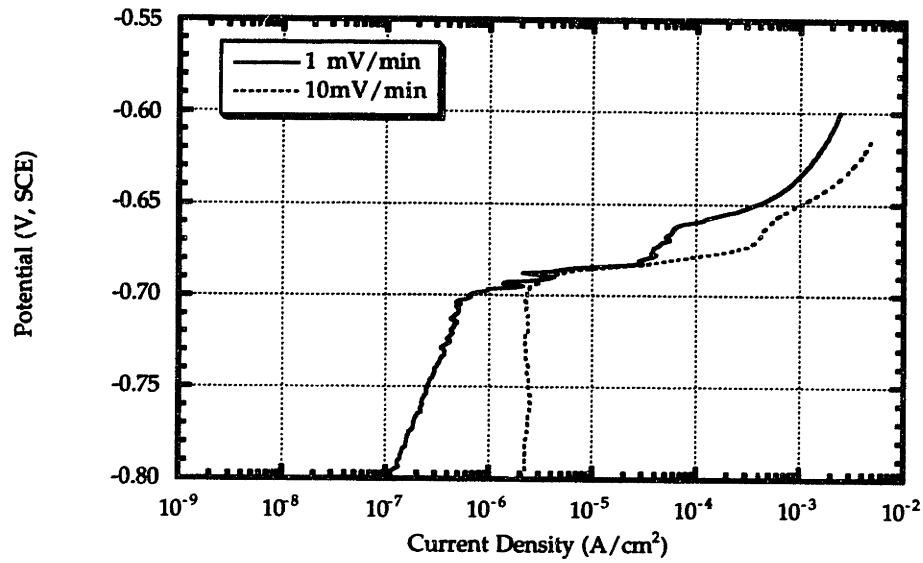

Figure 4.15. The effect of scan rate on the critical potentials for 7178-T6 in 0.1M NaCl at 298K is demonstrated.

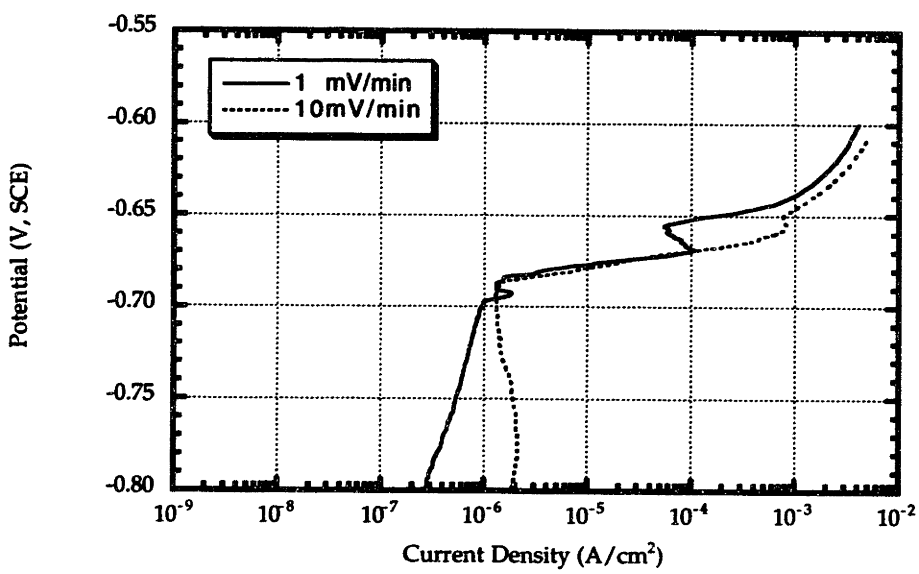

Figure 4.16. The effect of scan rate on the critical potentials for 7075-T651 in 0.1M NaCl at 298K is demonstrated.

4.2.4 Effect of Chloride Ion Concentration on the Breakdown Potentials

Dynamic polarization experiments were conducted at 298K as a function of orientation and material in 0.1M, 0.3M, 1.0M, 3.0M, and 5.0M (saturation at 298K) NaCl solutions. The chloride ion concentrations were converted to activities via the activity coefficients listed in Table 4.1.[72] The breakdown potentials (E_{pit} and E_{iga}) for 7075-T651 and 7178-T6 as a function of orientation and chloride ion activities are presented in Figures 4.17 and 4.18. The critical potentials are fitted to the logarithmic relationship and results of regression analysis are presented in Appendix B. In general, the values for E_{pit} and E_{iga} were more active for the 7178-T6 material at a given chloride ion concentration.

Table 4.1. Chloride ion activity coefficients used.[72]

Concentration (M)	0.10	0.30	1.0	3.0	5.0
Activity coefficient, γ	0.78	0.71	0.66	0.71	0.83
Activity	0.078	0.21	0.66	2.1	4.2

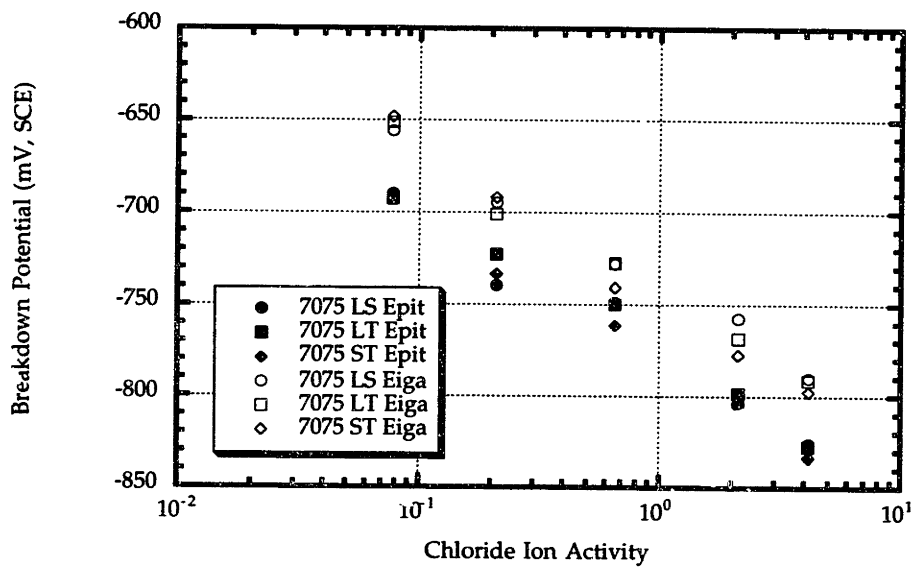

Figure 4.17. Plot of pitting potential (E_{pit}) and intergranular corrosion potential (E_{iga}) in 7075-T651 as a function of chloride ion activity and orientation.

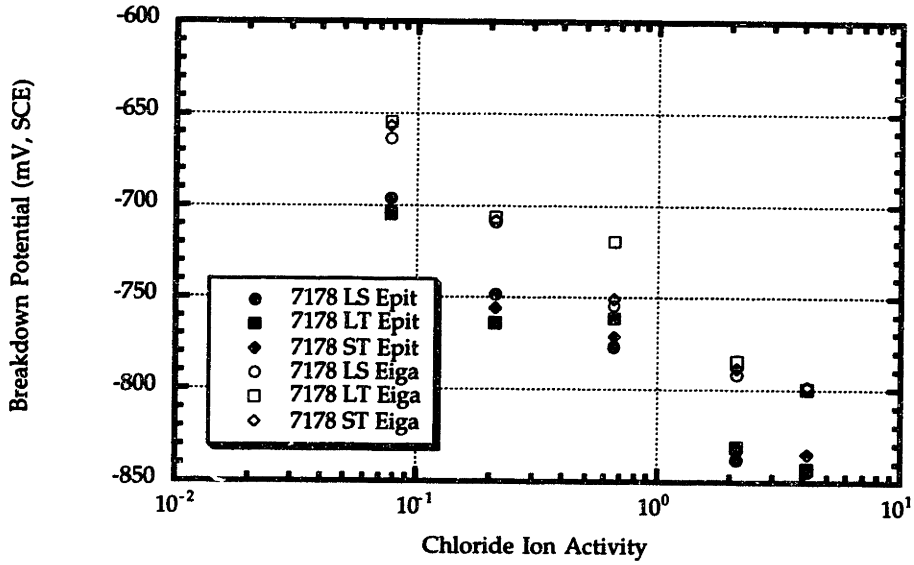

Figure 4.18. Plot of pitting potential (E_{pit}) and intergranular corrosion potential (E_{iga}) in 7178-T6 as a function of chloride ion activity and orientation.

4.2.5 Effect of Temperature on the Breakdown Potentials

Dynamic polarization experiments were conducted in 1.0M NaCl solutions at 298K, 308K, 318K, and 323K. The effect of temperature on the critical potentials (E_{pit} and E_{iga}) are presented in Figures 4.19 and 4.20. The critical potentials are found to be proportional to the reciprocals of the absolute temperature. Results from linear regression analysis are presented in Appendix B.

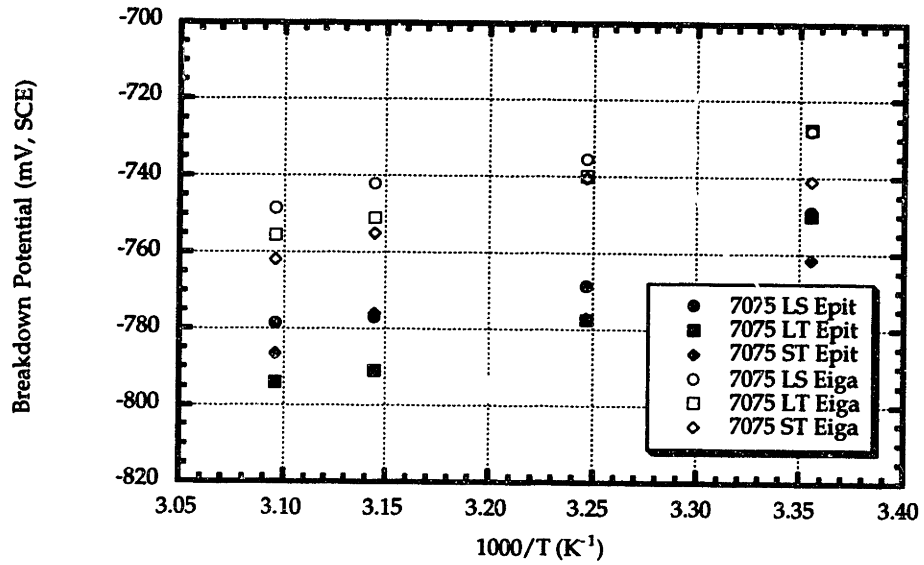

Figure 4.19. Plot of critical pitting potential (E_{pit}) and intergranular corrosion potential (E_{iga}) in 7075-T651 as a function of temperature and orientation in 1.0M NaCl solutions.

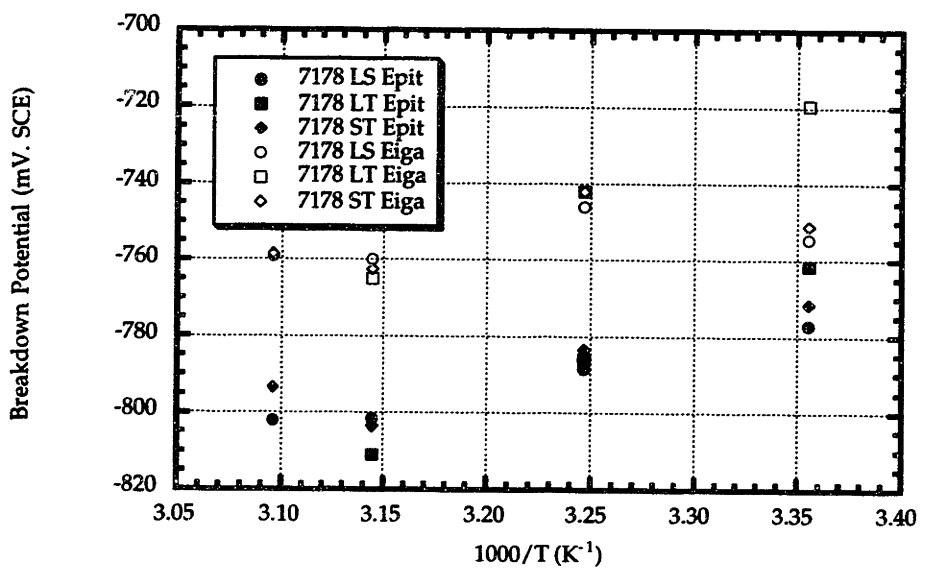

Figure 4.20. Plot of critical pitting potential (E_{pit}) and intergranular corrosion potential (E_{iga}) in 7178-T6 as a function of temperature and orientation in 1.0M NaCl solutions.

4.2.6 Repassivation Behavior

Cyclic polarization experiments were conducted in deaerated 1.0M NaCl solution at 298K to examine the repassivation behavior of 7178-T6 and 7075-T651. The results are presented in Figures 4.21 and 4.22. The arrows in the figures indicate the direction of polarization. The free corrosion potential after exposure to potentials above the breakdown potentials is lower (more active) than that for the unexposed material. Looked at in another way, after exposure above the breakdown potentials, the corrosion current density for a given fixed potential noble to the corrosion potential is higher (by several orders of magnitude). The magnitude of this difference is larger, both in terms of the potential difference and current density, for the 7178-T6 material. In a practical sense, this means that the 7178-T6 material is easier to pit and once pit has initiated, it is easier (less noble potential required) to maintain pit growth.

The average E_{corr} and E_{repass} are -0.91 and -0.95V SCE respectively for 7075-T651 while they are -0.90 and -0.96V SCE for 7178-T6. In other words, the difference between E_{corr} and E_{repass} is more pronounced for 7178-T6.

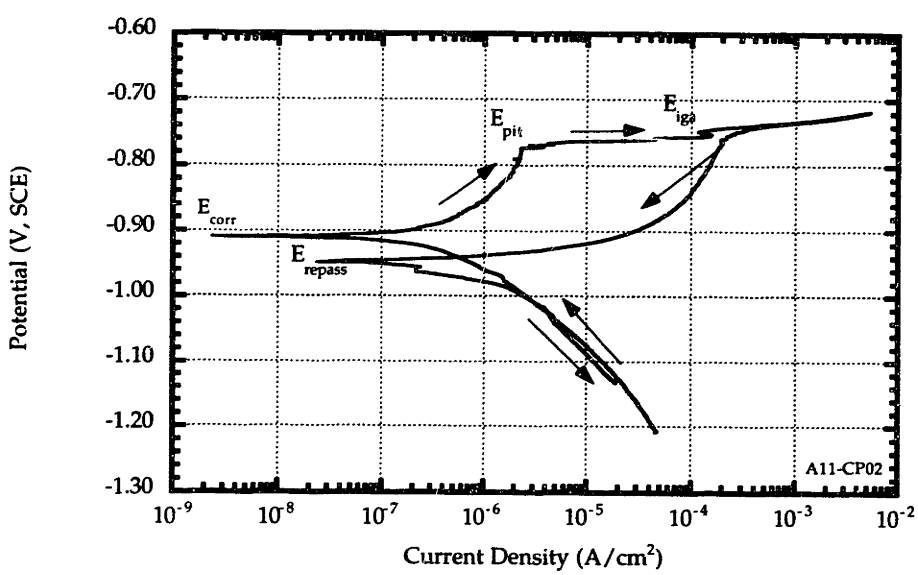

Figure 4.21. Cyclic polarization behavior of 7178-T6 in 1.0M NaCl at 298K. The arrows indicate the direction of polarization.

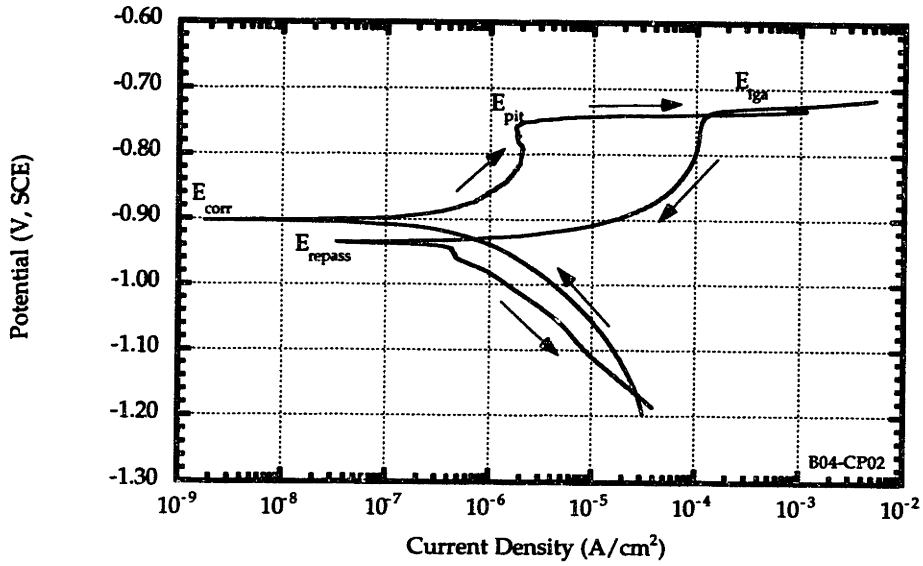

Figure 4.22. Cyclic polarization behavior of 7075-T651 in 1.0M NaCl at 298K. The arrows indicate the direction of polarization.

4.2.7 Polarization Behavior of the Intermetallic Alloys

Dynamic polarization experiments were conducted on the five intermetallic alloys and pure aluminum in 1.0M NaCl solution at 298K. The pH of the electrolyte was found to be 6.2. At least two experiments were conducted on each material to verify the accuracy and reproducibility of the data. Typical results are illustrated in Figures 4.23 through 4.28.

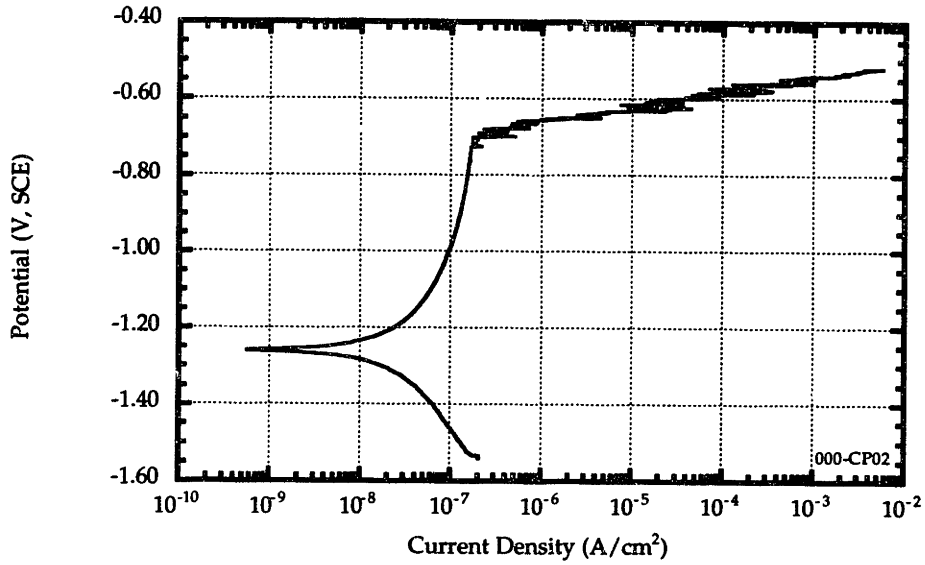

Figure 4.23. Typical polarization response of pure aluminum in 1.0M NaCl solution at 298K.

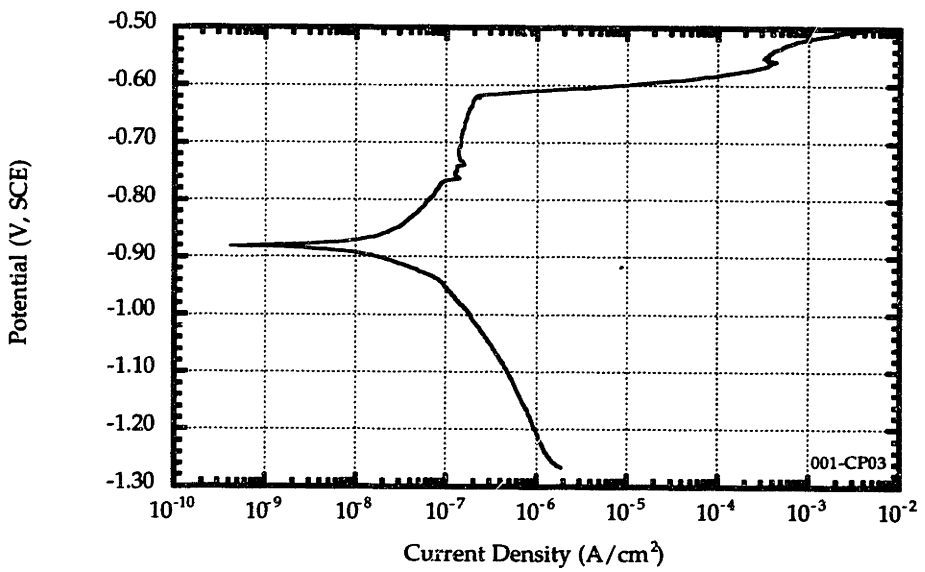

Figure 4.24. Polarization plot of Al_2Cu in 1.0M NaCl solution at 298K.

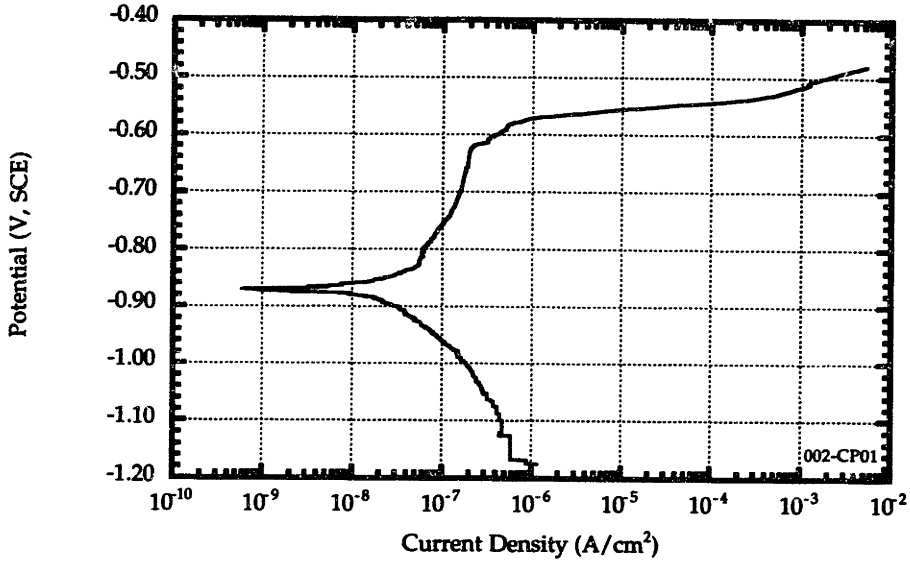

Figure 4.25. Polarization plot of Al_2Cu + 1.5% Zn in 1.0M NaCl solution at 298K.

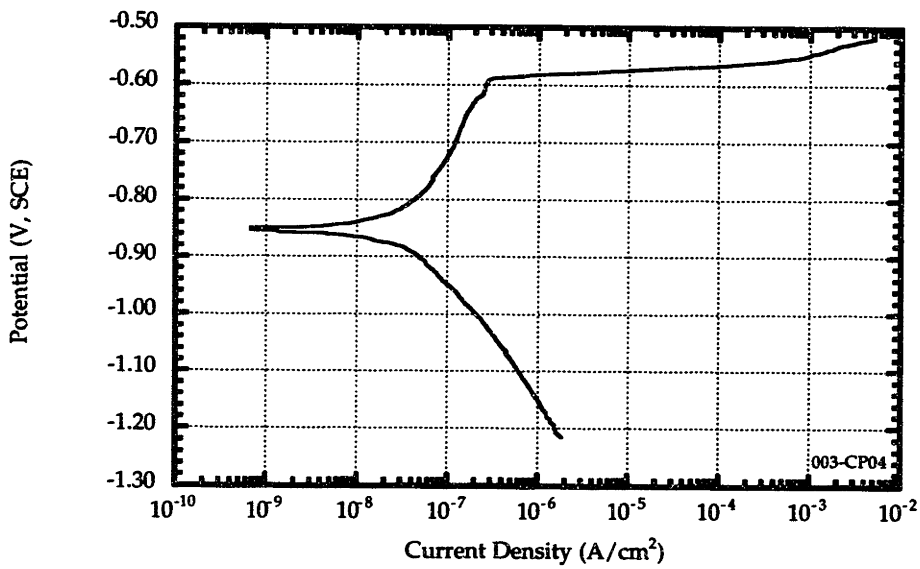

Figure 4.26. Typical polarization plot of Al_2Cu + 2.5% Zn in 1.0M NaCl solution at 298K.

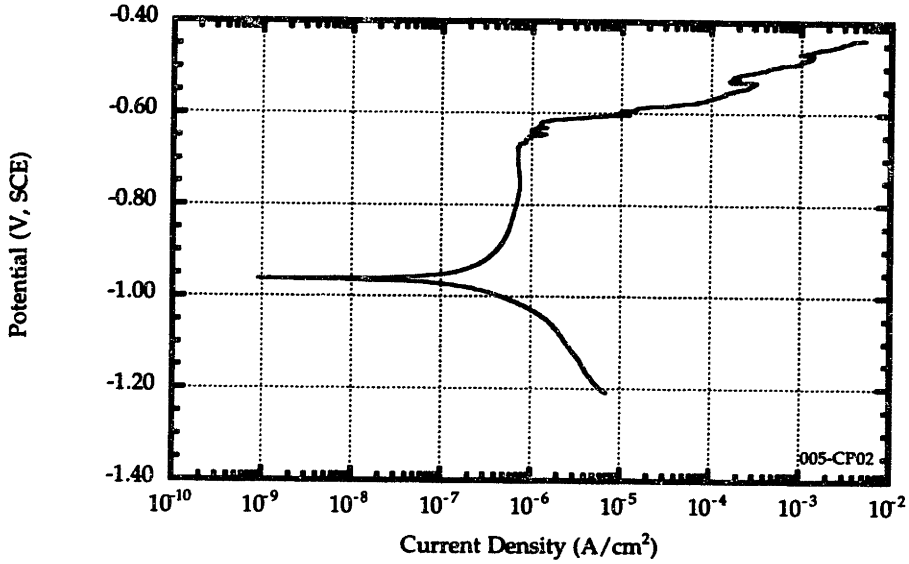

Figure 4.27. Typical polarization plot of $Al_6(Fe,Cu)$ in 1.0M NaCl solution at 298K.

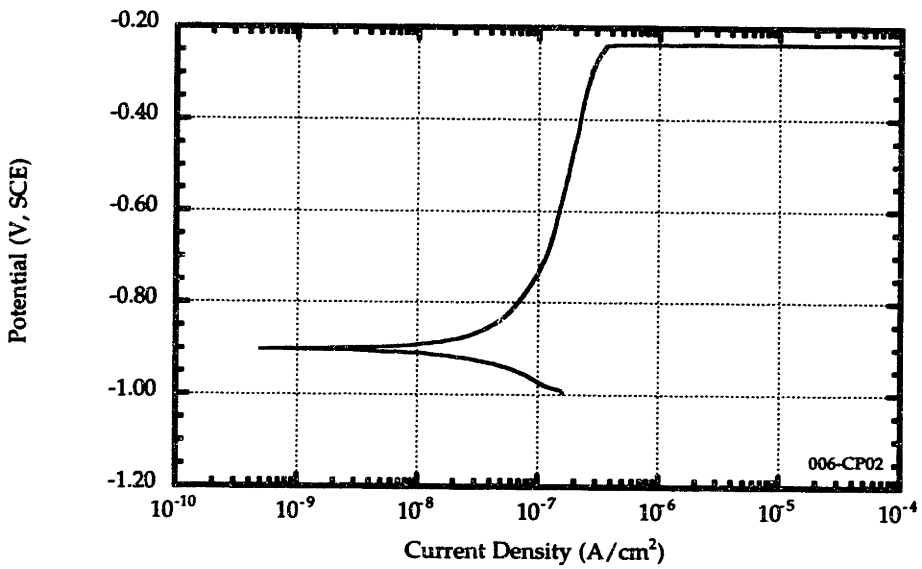

Figure 4.28. Typical polarization plot of Al_3Fe in 1.0M NaCl solution at 298K.

4.2.7.1 Effect of Oxygen

Polarization scans were conducted in aerated 1.0M NaCl solution at 298K. Figure 4.29 through 4.34 compares the polarization behavior of 7075-T651, 7178-T6, pure Al, intermetallic alloys Al_2Cu + 2.5% Zn, and Al_3Fe in aerated and deaerated solutions. The corrosion potential in all cases is more noble (more positive) in the aerated environment. The cathodic current density is also higher in the aerated solution. The corrosion potential for 7075-T651 and 7178-T6 in aerated solutions is more noble than their pitting potential (E_{pit}). In other words, pits can form spontaneously on the surface of these alloys in aerated environments.

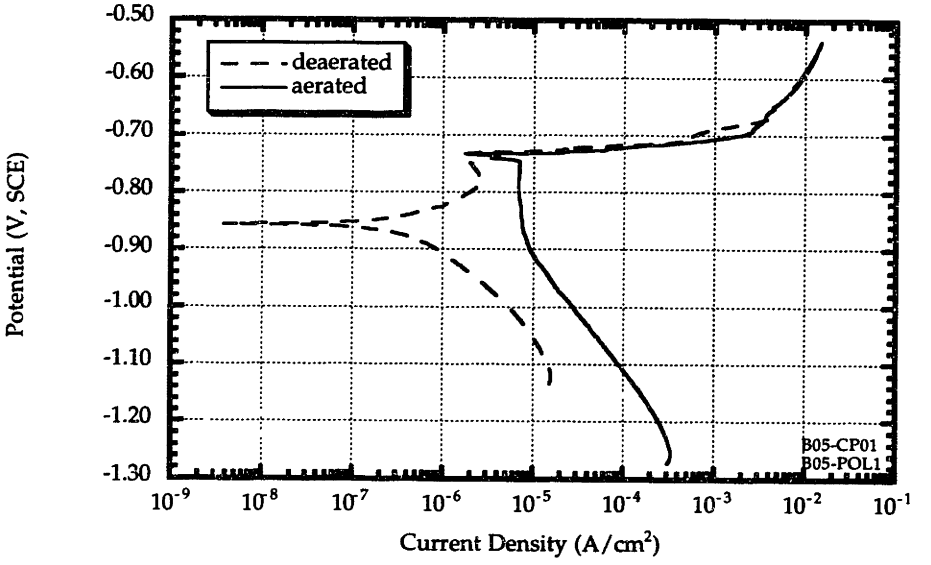

Figure 4.29. Comparison of polarization behavior for 7075-T651 in aerated and deaerated 1.0M NaCl solution at 298K.

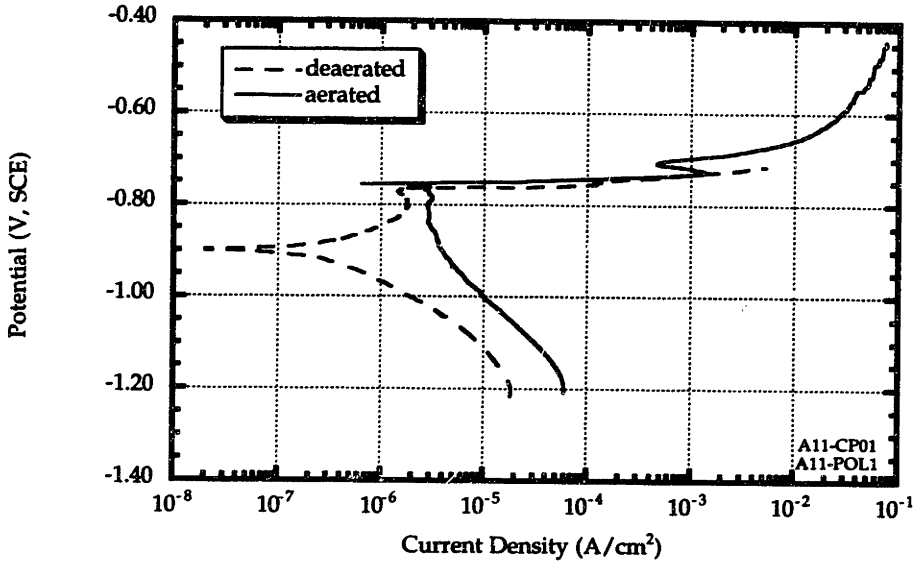

Figure 4.30. Comparison of polarization behavior for 7178-T6 in aerated and deaerated 1.0M NaCl solution at 298K.

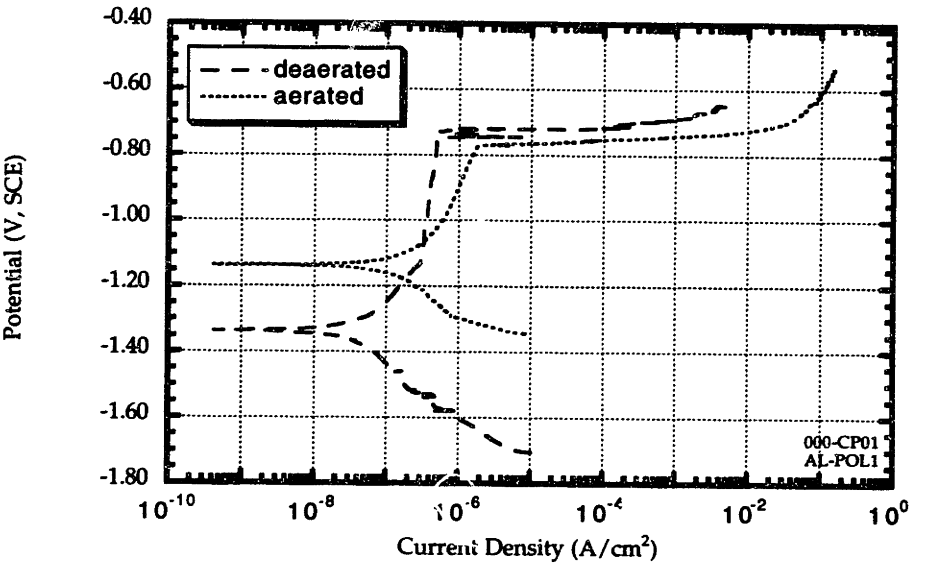

Figure 4.31. Comparison of polarization behavior for pure Al in aerated and deaerated 1.0M NaCl solution at 298K.

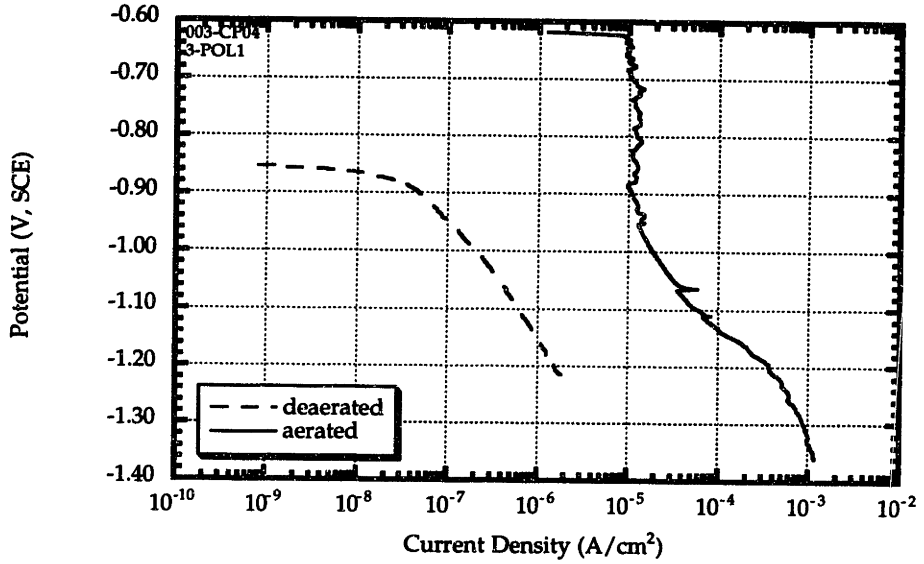

Figure 4.32. Comparison of cathodic polarization behavior for Al_2Cu + 2.5% Zn in aerated and deaerated 1.0M NaCl solution at 298K.

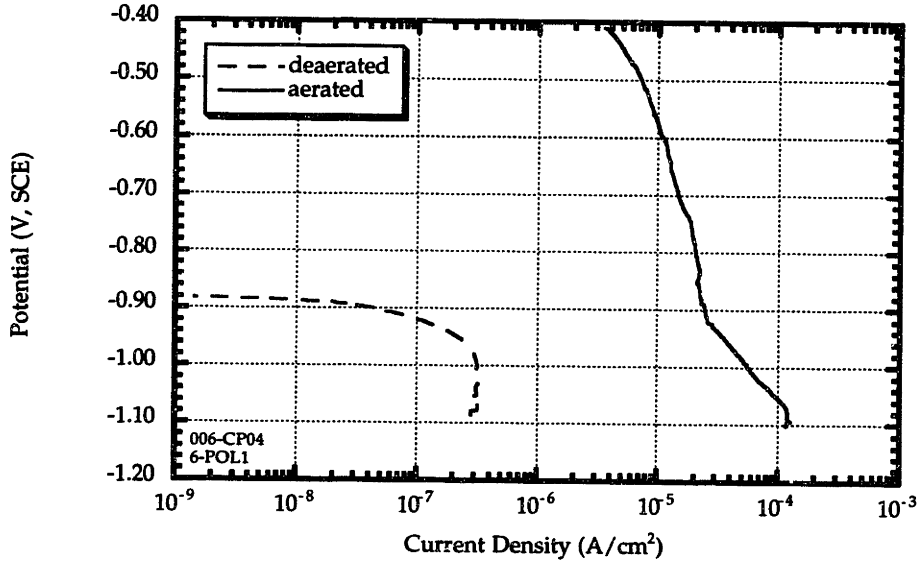

Figure 4.33. Comparison of polarization behavior for Al_3Fe in aerated and deaerated 1.0M NaCl solution at 298K.

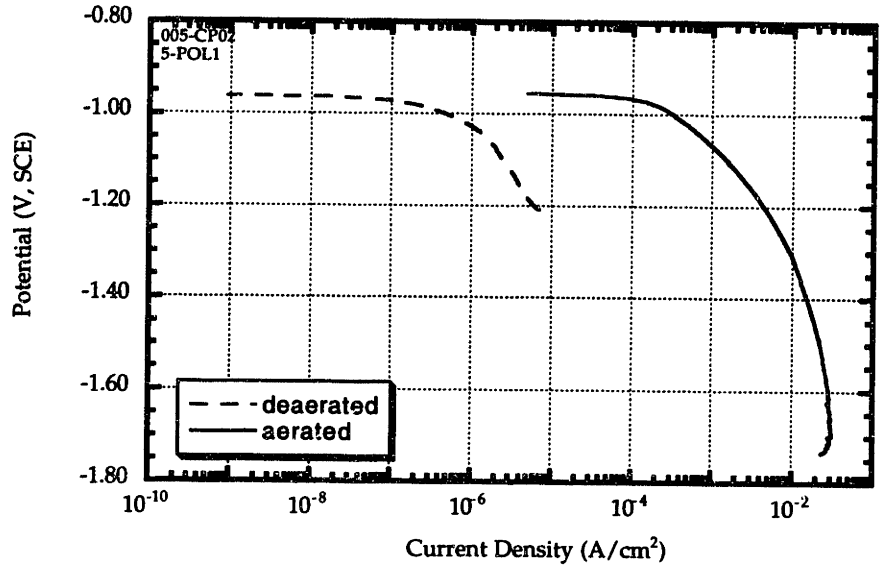

Figure 4.34. Comparison of cathodic polarization behavior for $Al_6(Fe,Cu)$ in aerated and deaerated 1.0M NaCl solution at 298K.

4.2.8 Polarization Behavior of the Wing Joint

Dynamic polarization experiments were conducted on the rivets obtained from the dismantled joints. The results of this analysis are shown in Figure 4.35. Since the plate material used for the two joints are the same, only the plate material from joint #2 was tested. These results are shown in Figure 4.36. Polarization scans were conducted in deaerated 1.0M NaCl solutions.

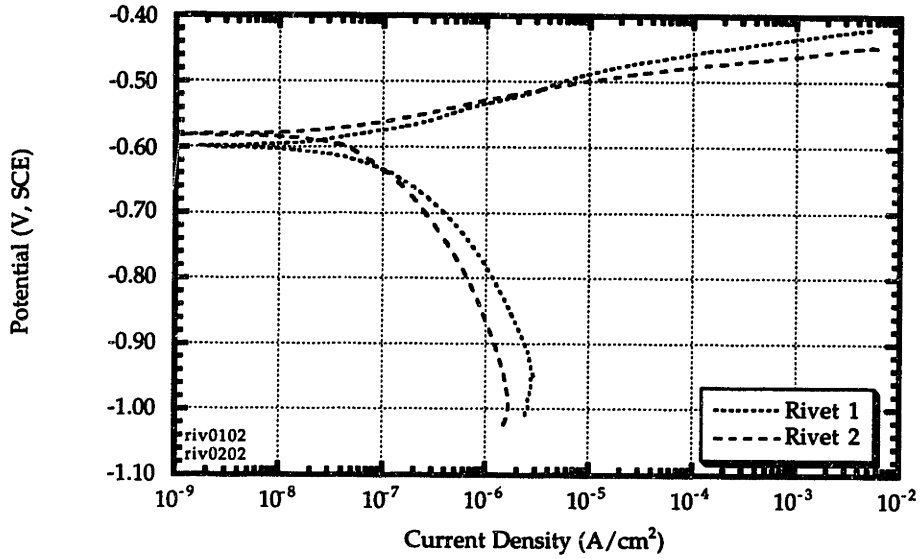

Figure 4.35. Dynamic polarization plots of the two rivets in 1.0M NaCl solution at 298K.

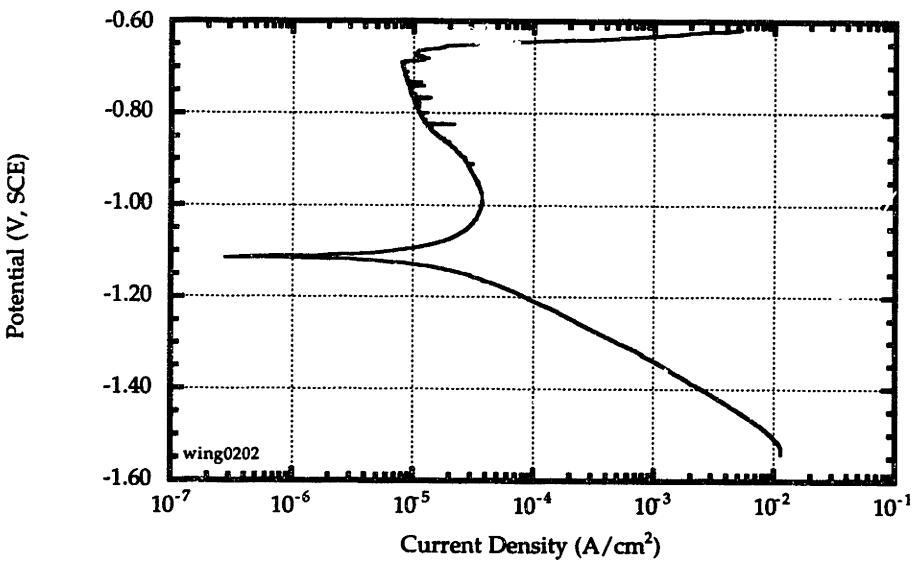

Figure 4.36. Dynamic polarization of plate material from joint #2 in 1.0M deaerated NaCl solution at 298K.

4.2.8.1 Effect of Oxygen

Dynamic polarization experiments were also conducted on the rivets and the alloy plate from joint #2 in aerated 1.0M NaCl solutions. The results from the cathodic scans are presented in Figures 4.37 and 4.38 below. The deaerated data is included for comparison purposes. The current density for the rivet is roughly two orders of magnitude higher in the aerated environment. The cathodic current density for the alloy plate is also higher in the aerated environment although the difference between the two environments is less pronounced. The corrosion potentials for both materials are more noble in the aerated environment.

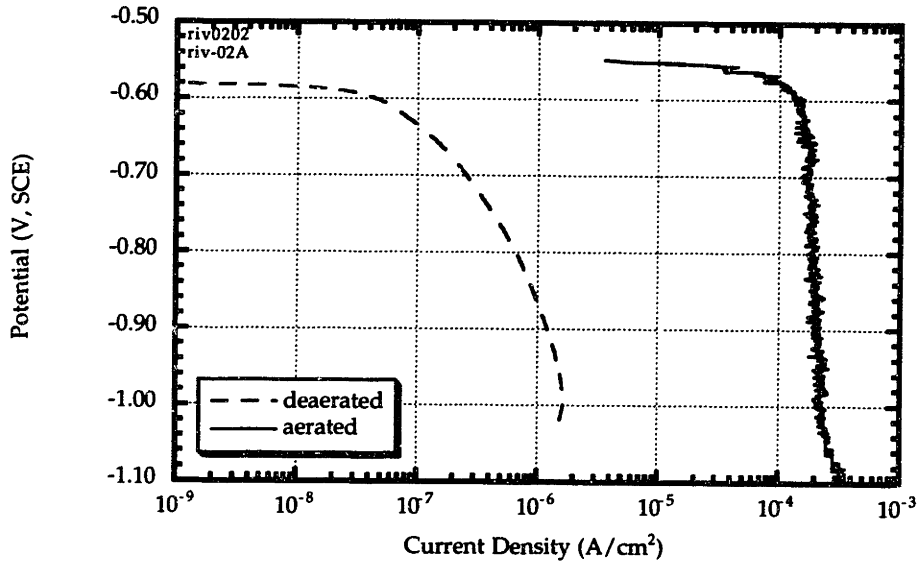

Figure 4.37. Comparison of the cathodic polarization behavior in aerated and deaerated 1.0M NaCl for the steel rivet.

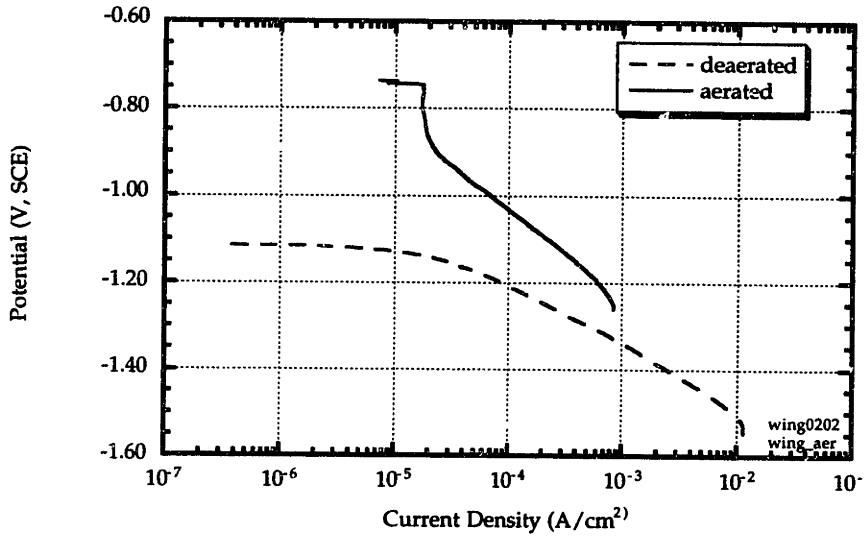

Figure 4.38. Comparison of cathodic polarization behavior for the alloy plate from joint #2 in aerated and deaerated 1.0M NaCl solution.

4.2.9 Galvanic Interaction

4.2.9.1 Constituent Particle / Matrix Interaction

In the deaerated solution, hydrogen reduction (equation 4.2) is the most likely cathodic reaction due to the slightly acidic pH of 6.2. The equilibrium potential for this reaction in the environment is:

$$H^+ + e^- \rightleftarrows \frac{1}{2}H_2 \qquad (4.2)$$

$$E_{eq}\,(V, SHE) = -0.059\,pH$$
$$= -0.37\ V, SHE$$
$$E_{eq}\,(V, SCE) = -0.61\ V, SCE$$

The cathodic and anodic polarization data for the intermetallics and pure aluminum in deaerated 1.0M NaCl is presented as Tafel plots in Figures 4.39 and 4.40. The exchange current densities and slopes were extracted by regression analysis on the linear portion of the plots as outlined in Section 1.1.1. This information was converted to the more convenient form of:

$$E\ (V, SCE) = a + b \log (i) \qquad (4.3)$$

and is summarized in Tables 4.2 and 4.3.

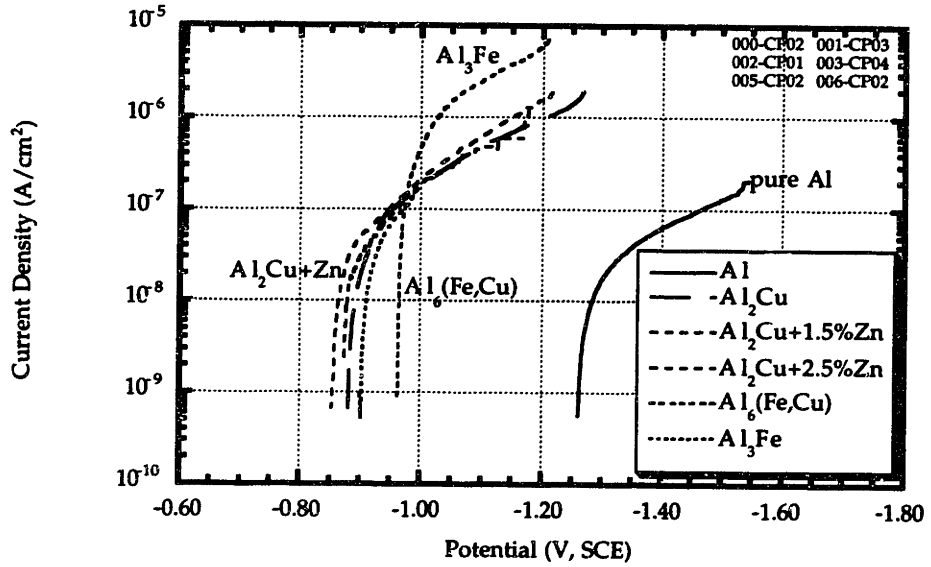

Figure 4.39. Tafel plot showing the cathodic polarization data for pure aluminum and the intermetallic alloys in deaerated 1.0M NaCl at 298K.

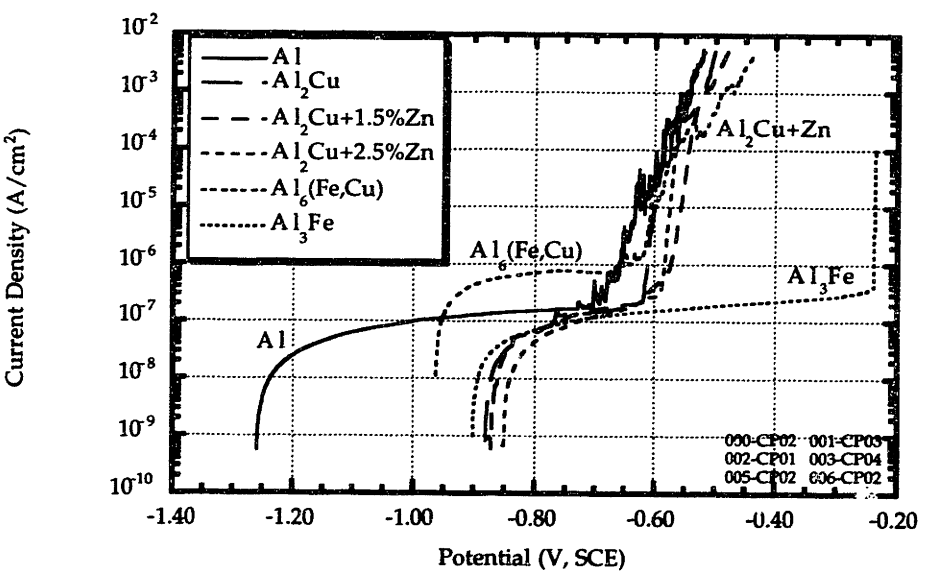

Figure 4.40. Tafel plot of the anodic polarization data for pure aluminum and the intermetallic alloys in deaerated 1.0M NaCl at 298K.

Dynamic polarization experiments were also conducted in aerated 1.0M NaCl solutions. In addition to the hydrogen reduction reaction, reduction of dissolved oxygen (equation 4.3) can take place. The equilibrium potential for the oxygen reduction reaction for the pH range studied is 0.62V SCE. The cathodic polarization data for pure aluminum, Al_2Cu + 2.5% Zn, Al_3Fe, and $Al_6(Fe,Cu)$ in aerated environment are presented in Figure 4.41. The data is summarized in Table 4.2.

$$O_2 + 4H^+ + 4e^- \rightleftarrows 2H_2O \qquad (4.3)$$

$$E_{eq}\ (V, SHE) = 1.228 - 0.059\ pH$$
$$= 0.862\ V, SHE$$
$$E_{eq}\ (V, SCE) = 0.62\ V, SCE$$

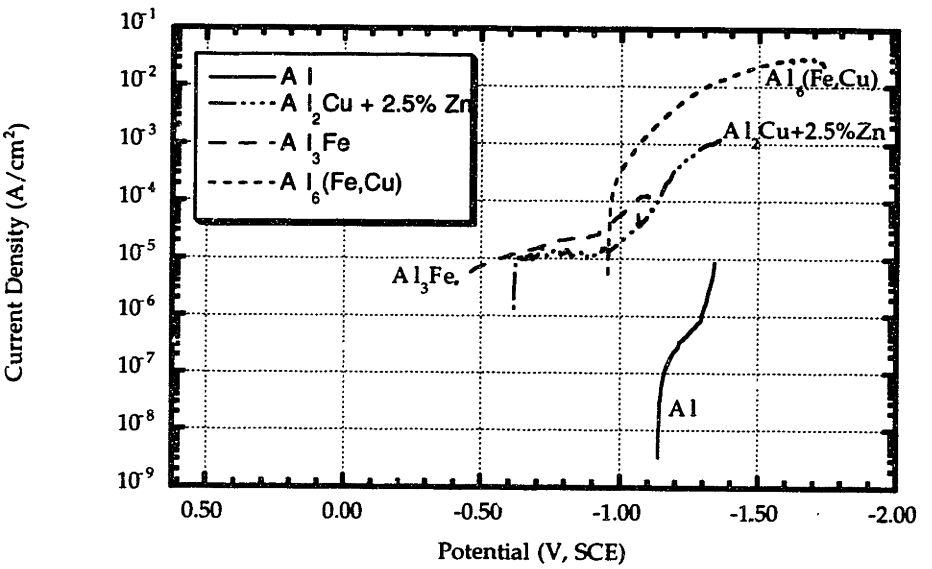

Figure 4.41. Tafel plot showing the cathodic polarization data for pure Al, Al_2Cu + 2.5% Zn, Al_3Fe, and $Al_6(Fe,Cu)$ in aerated 1.0M NaCl solution.

Table 4.2. Cathodic polarization kinetics parameters for the intermetallics and pure aluminum in aerated and deaerated 1.0M NaCl.

	deaerated			aerated		
Material	a	b (V)	i_o(A/cm^2)	a	b (V)	i_o(A/cm^2)
Pure Al	-3.38	-0.27	7.4×10^{-11}	-2.27	-0.22	1.4×10^{-13}
Al_2Cu	-2.89	-0.28	8.0×10^{-9}			
Al_2Cu + 1.5% Zn	-2.55	-0.23	3.5×10^{-9}			
Al_2Cu + 2.5% Zn	-2.35	-0.20	2.1×10^{-9}	-1.77	-0.25	1.9×10^{-15}
Al_6(Fe,Cu)	-2.54	-0.26	2.8×10^{-8}	-1.98	-0.30	2.9×10^{-9}
Al_3Fe	-1.82	-0.12	3.7×10^{-10}	-3.16	-0.51	3.9×10^{-8}

Table 4.3. Anodic polarization parameters for the intermetallics and pure aluminum in deaerated 1.0M NaCl at 298K.

Material	a	b (V, SCE)
Pure Al		
E > -0.69V	-0.43	0.039
E < -0.69V	7.57	1.23
Al_2Cu		
E > -0.62V	-0.54	0.012
E < -0.62V	3.41	0.60
Al_2Cu + 1.5% Zn		
E > -0.58V	-0.48	0.014
E < -0.58V	1.66	0.35
Al_2Cu + 2.5% Zn		
E > -0.59V	-0.53	0.0092
E < -0.59V	1.31	0.29
Al_6(Fe,Cu)		
E > -0.63V	-0.44	0.032
E < -0.63V	3.55	0.70
Al_3Fe		
E > -0.24V	-0.23	0.00058
E < -0.24V	7.23	1.15

With the data in Tables 4.2 and 4.3, the net current density for intermetallic - pure aluminum couples can be computed by applying the mixed potential theory (equations 1.12 through 1.14). The α and β phases in this case are pure aluminum and the intermetallics.

The free corrosion potential is defined as the potential where the net current is zero. Since the anodic and cathodic currents have opposite signs, the free corrosion potential can be found by equating the sum of all cathodic currents to the negative sum of all anodic currents.

$$\sum i_c = -\sum i_a \qquad (4.4)$$

$$f_{Al}\, i_{a,Al} + f_{int}\, i_{a,int} = -(f_{Al}\, i_{c,Al} + f_{int}\, i_{c,int})$$

where

f_{Al} : area fraction of pure Al in the coupled sample
f_{int} : area fraction of the intermetallics in the coupled sample
$i_{a,Al}$: anodic current density on pure Al
$i_{a,int}$: anodic current density on the intermetallics
$i_{c,Al}$: cathodic current density on pure Al
$i_{c,int}$: cathodic current density on the intermetallics

The free corrosion potential for the intermetallic - pure Al couples were calculated as a function of the area fraction of the intermetallic alloy; that is, f_{int} is the independent variable in these calculations. The calculation for Al-Al_2Cu couple (f_{int} = 0.50) in deaerated environment is demonstrated in Figure 4.42. The variation of the coupled free corrosion potential in deaerated and aerated solutions as a function of the area fraction of intermetallic particle are presented in Figures 4.43 and 4.44 respectively. Figures 4.43b and 4.44b are magnified views of these calculations near the pure aluminum end of the spectrum. Galvanic coupled experiments were conducted to verify these calculations. The results of these experiments are shown in Figures 4.45-4.47.

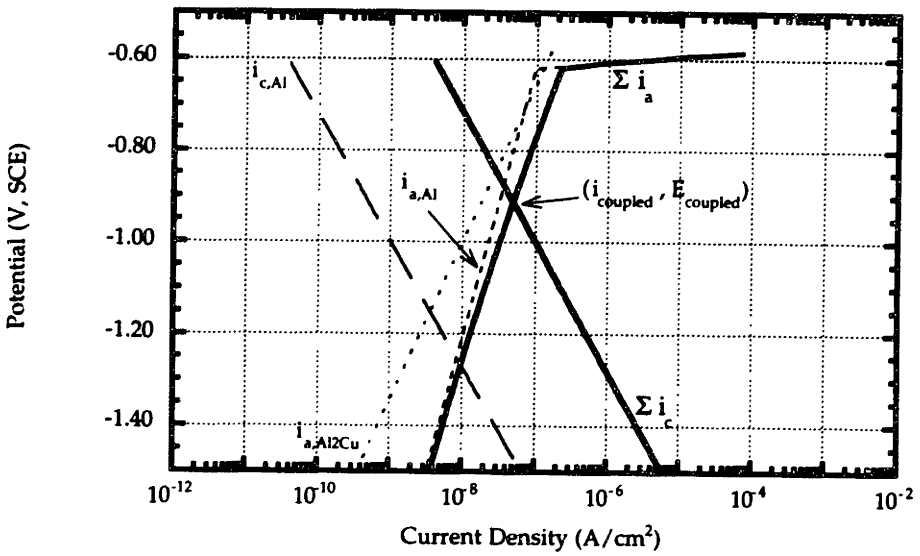

Figure 4.42. Calculation of free corrosion potential of coupled Al and Al_2Cu in deaerated 1.0M NaCl solution at 298K. (Area fraction of Al_2Cu = 0.5)

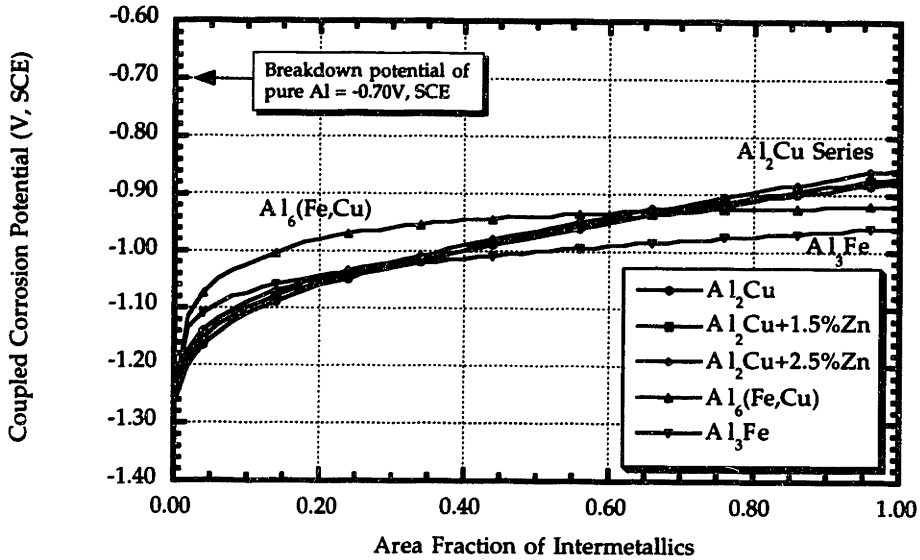

(a)

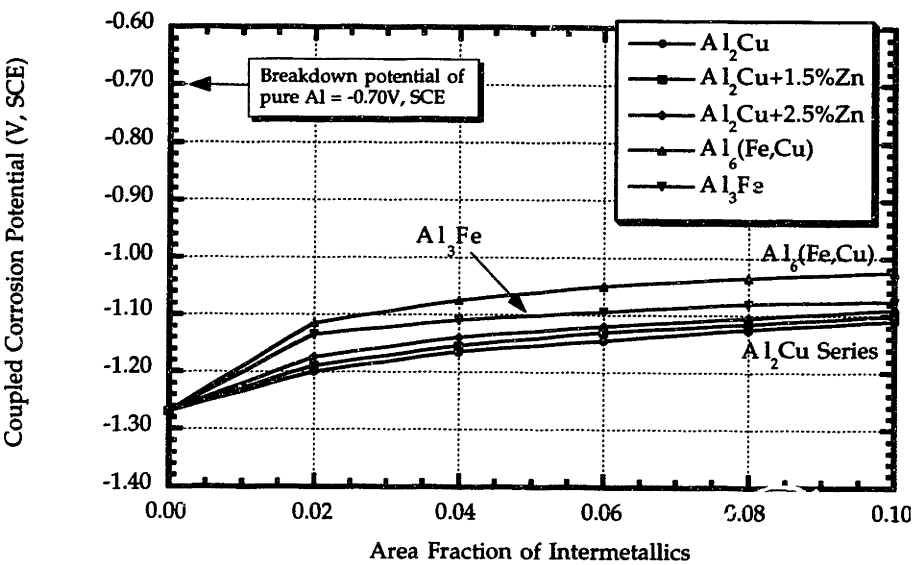

(b)

Figure 4.43. Calculated corrosion potential of intermetallic - pure Al couples in deaerated 1.0M NaCl solution at 298K. Figure b is a magnified view of these calculation when the couples are predominantly aluminum.

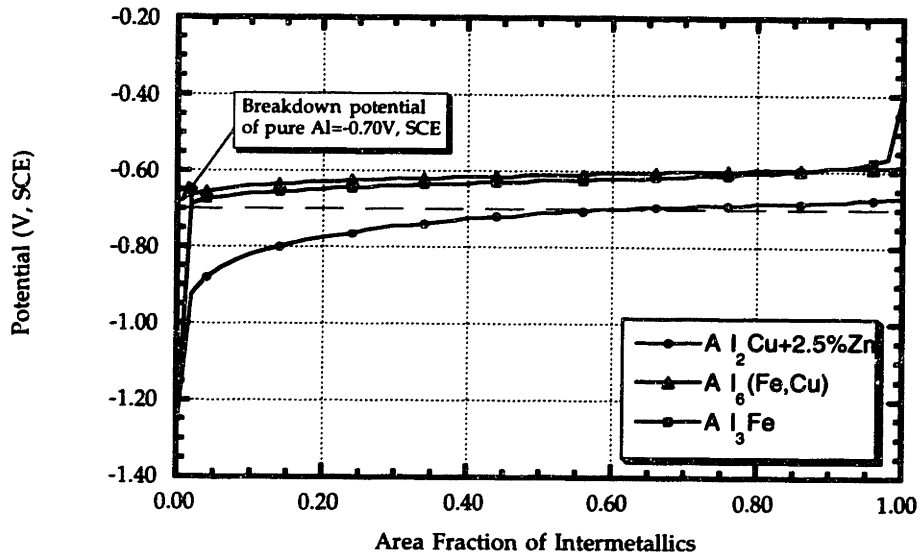

(a)

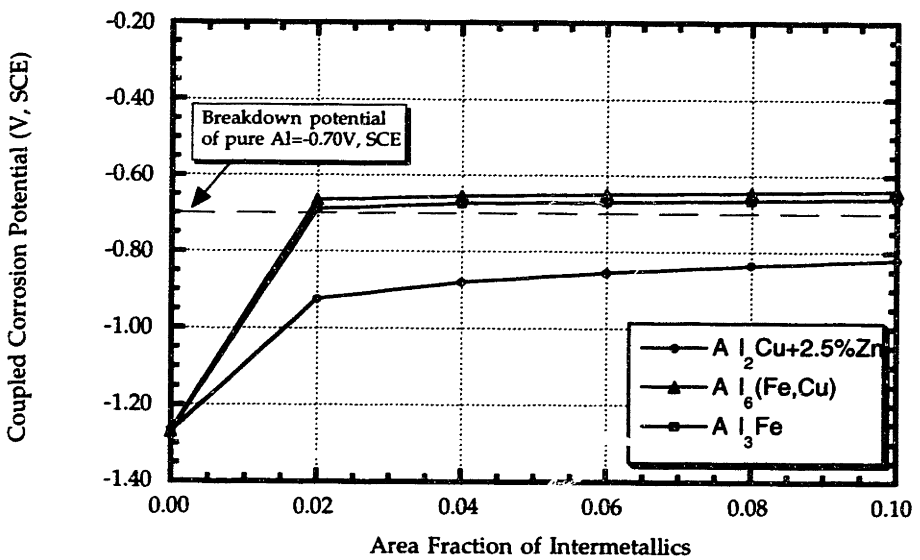

(b)

Figure 4.44. Calculated corrosion potential of intermetallic - pure Al couples in aerated 1.0M NaCl solution at 298K. Figure b is a magnified view of these calculations when the coupled samples are predominantly aluminum.

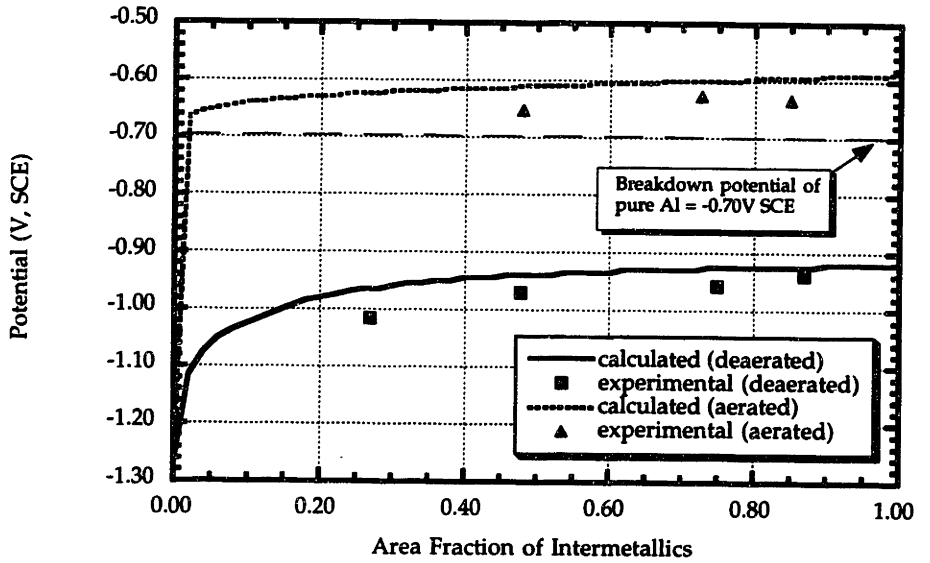

Figure 4.45. Comparison of calculated and experimental coupled corrosion potential in aerated and deaerated environments for $Al_6(Fe,Cu)$ - Al samples.

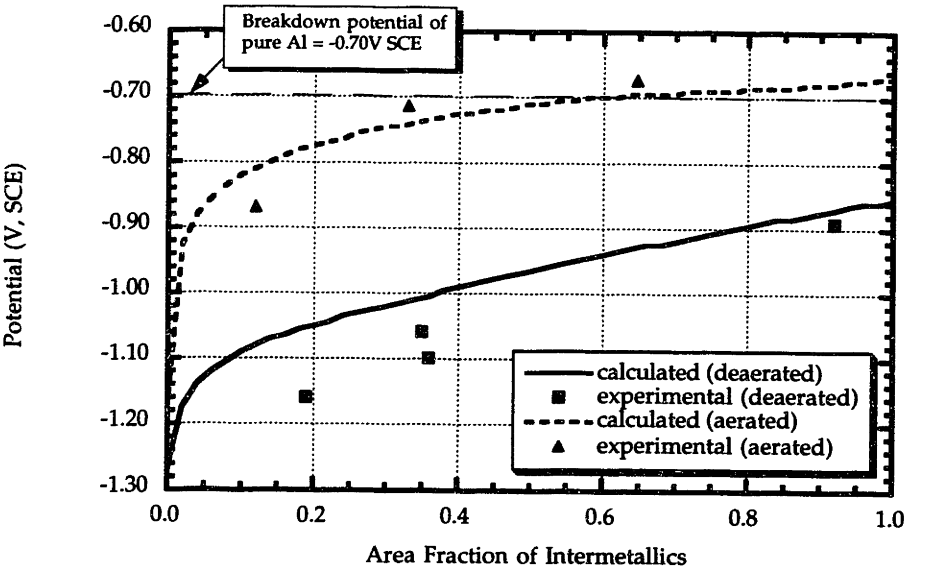

Figure 4.46. Comparison of calculated and experimental coupled corrosion potential in aerated and deaerated 1.0M NaCl for (Al_2Cu + 2.5%Zn) - Al samples.

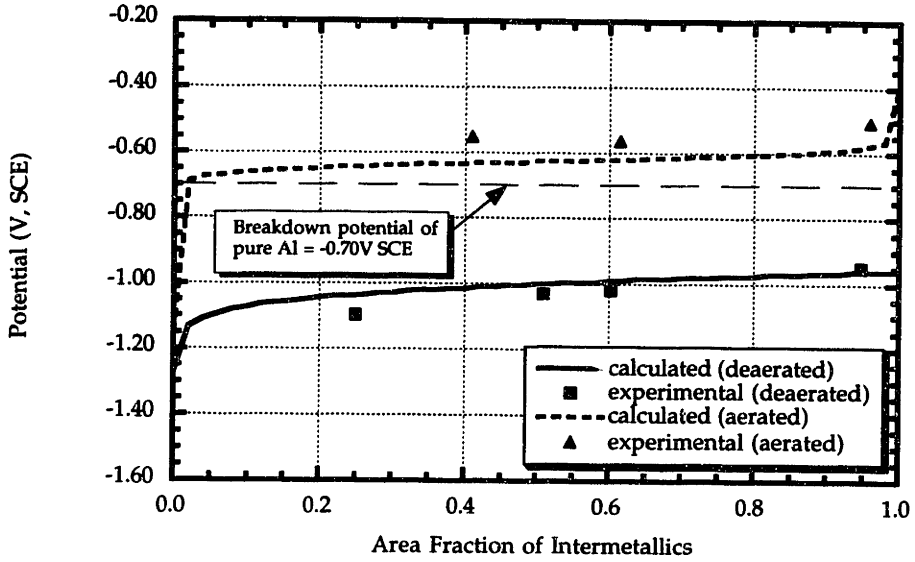

Figure 4.47. Comparison of calculated and experimental coupled corrosion potential in aerated and deaerated 1.0M NaCl for Al_3Fe - Al samples.

4.2.9.2 Rivet / Alloy Plate Interaction

The cathodic polarization data for the rivets, wing panel, 7075-T651, and 7178-T6 in aerated and deaerated 1.0M NaCl are presented as Tafel plots in Figures 4.48 and 4.49. Similarly, the anodic polarization data for these materials in deaerated 1.0M NaCl solution are presented in Figure 4.50. The kinetic parameters were extracted from these plots following the procedure outlined in Section 1.1.1. The cathodic and anodic reaction kinetics parameters are summarized in Tables 4.4 and 4.5 respectively. It is obvious from Figure 4.49 that the rivet is very effective at reducing oxygen. The exchange current density in aerated solutions on the rivet is on average three orders of magnitude higher than that of the aluminum alloys (Table 4.4).

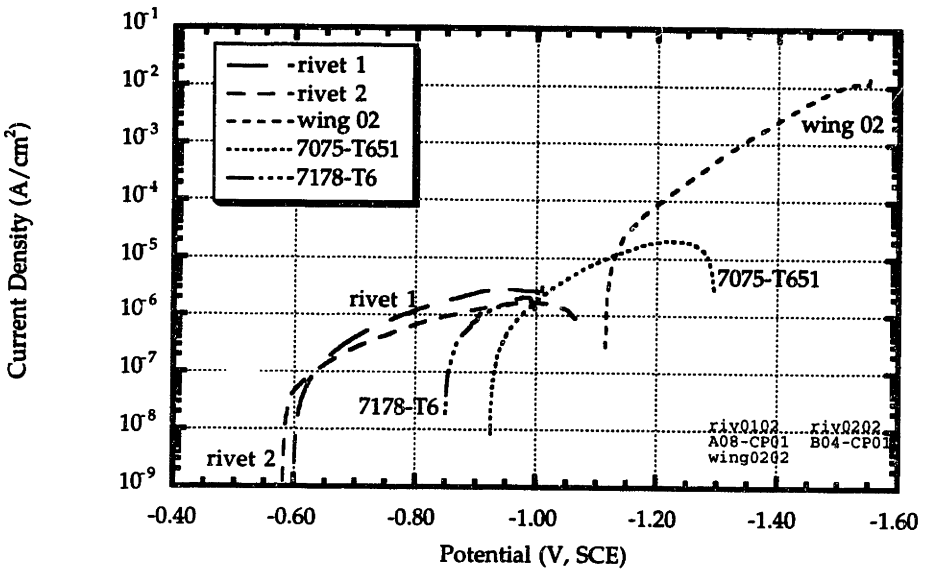

Figure 4.48. Tafel plot of the cathodic polarization data for the rivet from joints #1 and #2, and the wing panel #2 in deaerated 1.0M NaCl solution.

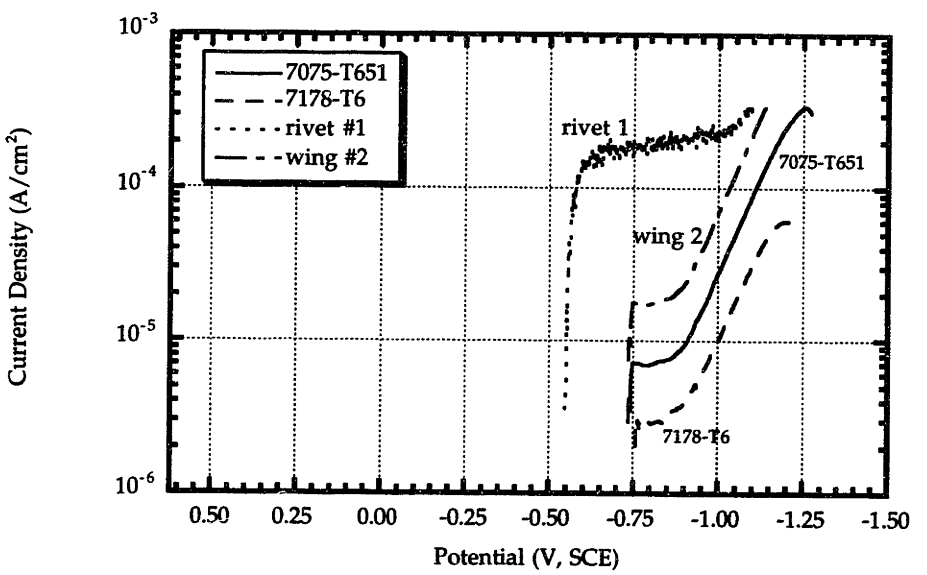

Figure 4.49. Tafel plot of the cathodic polarization data for the rivet, 7178-T6 and 7075-T651 in aerated 1.0M NaCl solution.

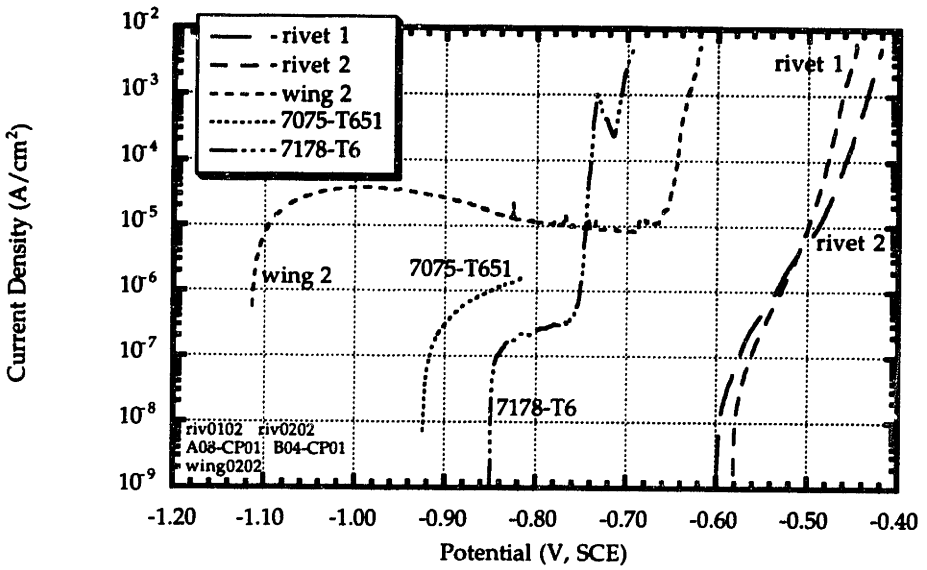

Figure 4.50. Tafel plot presenting the anodic polarization data of rivets from joints #1, #2, and wing material from joint #2. Representative data from 7075-T651 and 7178-T6 is also included.

Table 4.4. Cathodic reaction kinetics parameters extracted from Tafel plots.

	deaerated			aerated		
Material	a	b (V)	i_o(A/cm^2)	a	b (V)	i_o(A/cm^2)
Rivet #1	-2.29	-0.25	1.1×10^{-7}	-7.23	-1.73	1.7×10^{-8}
Rivet #2	-2.72	-0.31	9.4×10^{-8}			
Plate #2	-1.76	-0.14	1.9×10^{-9}	-2.01	-0.25	3.0×10^{-11}
7178-T6	-1.69	-0.12	5.9×10^{-10}	-2.25	-0.24	1.1×10^{-12}
7075-T651	-1.82	-0.15	4.8×10^{-9}	-1.91	-0.20	2.2×10^{-13}

Table 4.5. Anodic reaction kinetics parameters in deaerated 1.0M NaCl extracted from Tafel plots.

Material	a	b (V, SCE)
Rivet #1	-0.29	0.040
Rivet #2	-0.33	0.032
Plate #2	-0.59	0.014
7178-T6		
E > -0.77V	-0.69	0.015
E < -0.77V	-0.015	0.14
7075-T651		
E > -0.74V	-0.72	0.0052
E < -0.74V	-0.47	0.066

The free corrosion potential of coupling the rivets to the plate from joint #2, 7178-T6, and 7075-T651 was calculated by applying the mixed potential theory with the kinetics parameters listed above. The results of these calculations in both aerated and deaerated environments are presented in Figures 4.51 through 4.53.

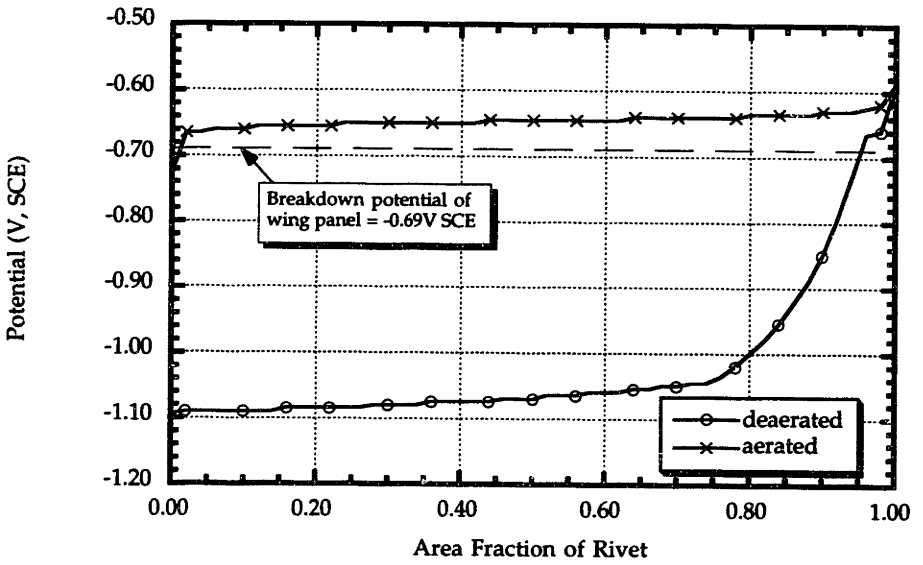

Figure 4.51. Plot showing the calculated corrosion potential of the coupled rivet - wing panel in aerated and deaerated 1.0M NaCl solutions.

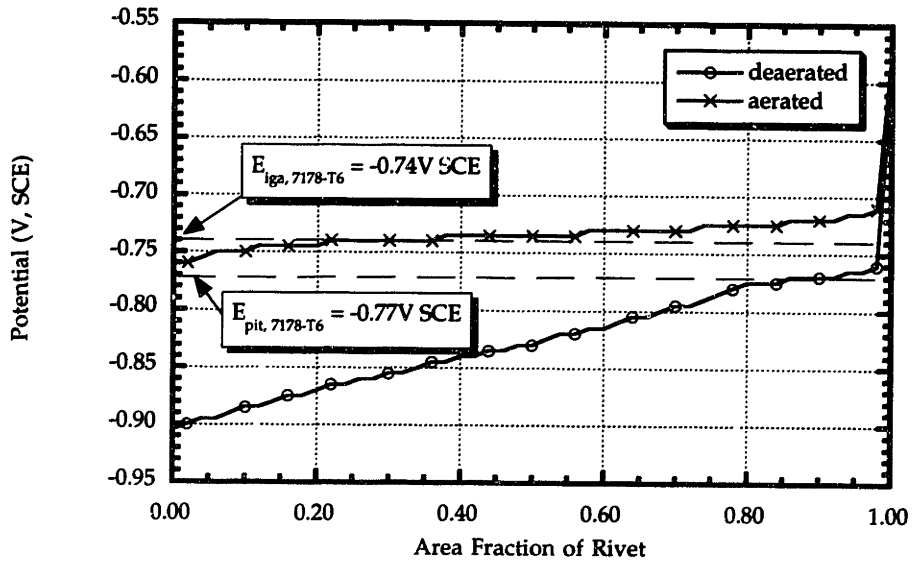

Figure 4.52. Plot showing the calculated corrosion potential of the coupled rivet - 7178-T6 in aerated and deaerated 1.0M NaCl solutions.

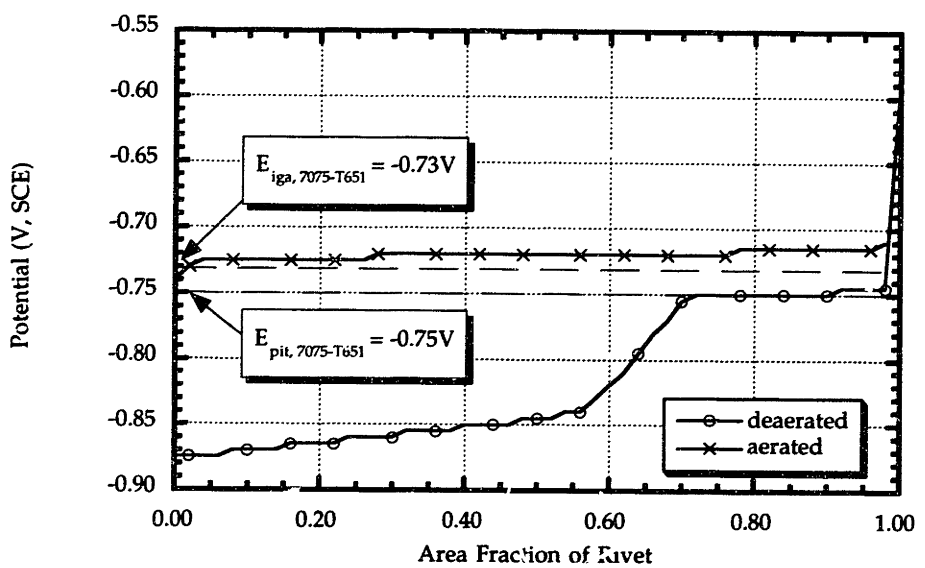

Figure 4.53. Plot showing the calculated corrosion potential of the coupled rivet - 7075-T651 in aerated and deaerated 1.0M NaCl solutions.

Experiments were conducted in 1.0M aerated and deaerated NaCl solutions to verify the calculations above. Comparisons between the experimental results and calculations are presented in Figures 4.54 to 4.56 below. There is in general good agreement between the calculated and observed results.

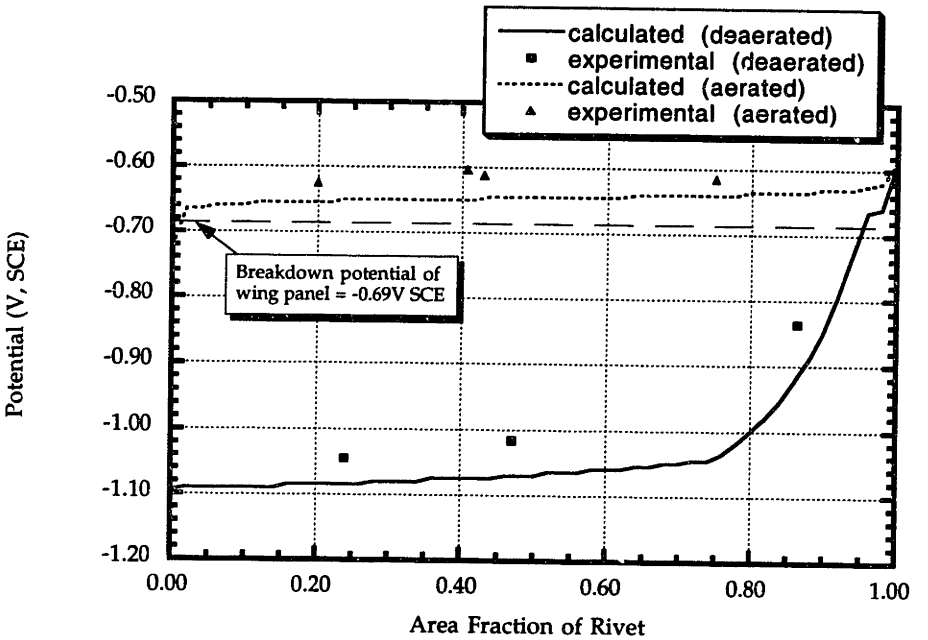

Figure 4.54. Comparison of calculated and experimental coupled corrosion potential in aerated and deaerated 1.0M NaCl for rivet - wing panel samples.

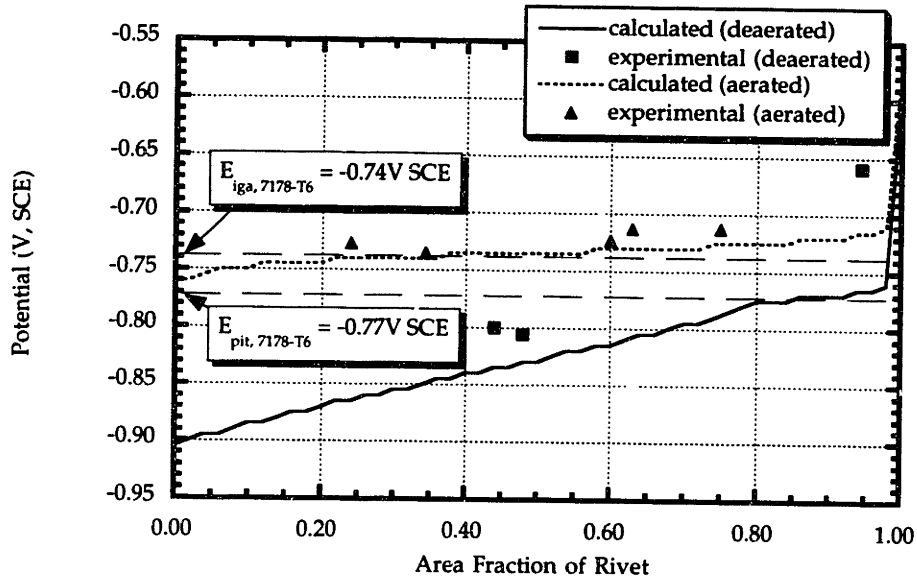

Figure 4.55. Comparison between experimental and calculated coupled corrosion potential between the steel rivet and 7178-T6 plate.

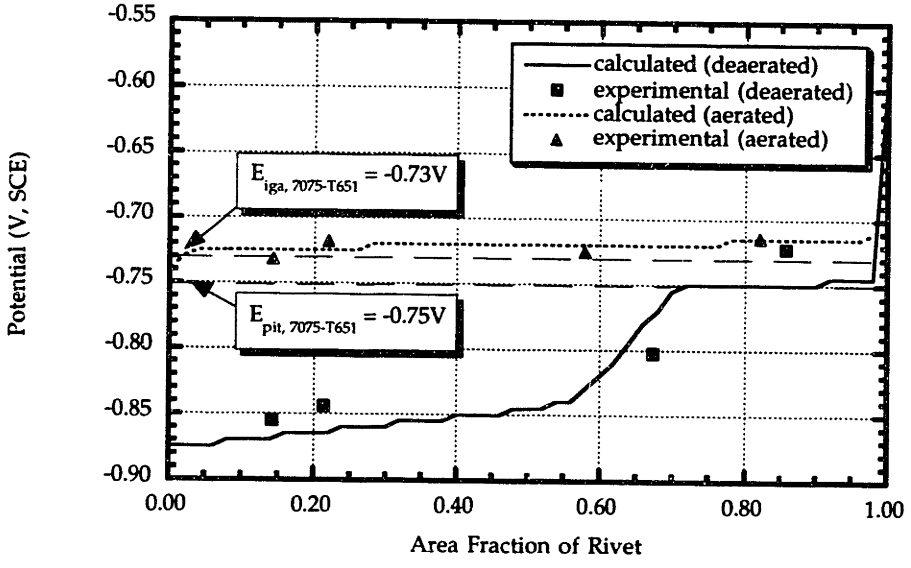

Figure 4.56. Comparison between experimental and calculated coupled corrosion potential between the steel rivet and 7075-T651 plate.

The important electrochemical potentials for 7178-T6 and 7075-T651 are summarized in Figures 4.57(a) and (b) respectively. The properties of the alloy are denoted in bold. The terms used in these figures are explained below.

Ecorr, dea.	: Corrosion potential of the alloy in deaerated environment
Ecorr, aer.	: Corrosion potential of the alloy in aerated environment
Eiga	: Critical potential for the initiation of intergranular attack
Epit	: Critical potential for the initiation of pitting
Ecorr, int, dea.	: Corrosion potential of the intermetallics in deaerated environment
Ecorr, int, aer.	: Corrosion potential of the intermetallics in aerated environment
Ecorr, riv.	: Corrosion potential of the rivet in both aerated and deaerated environment

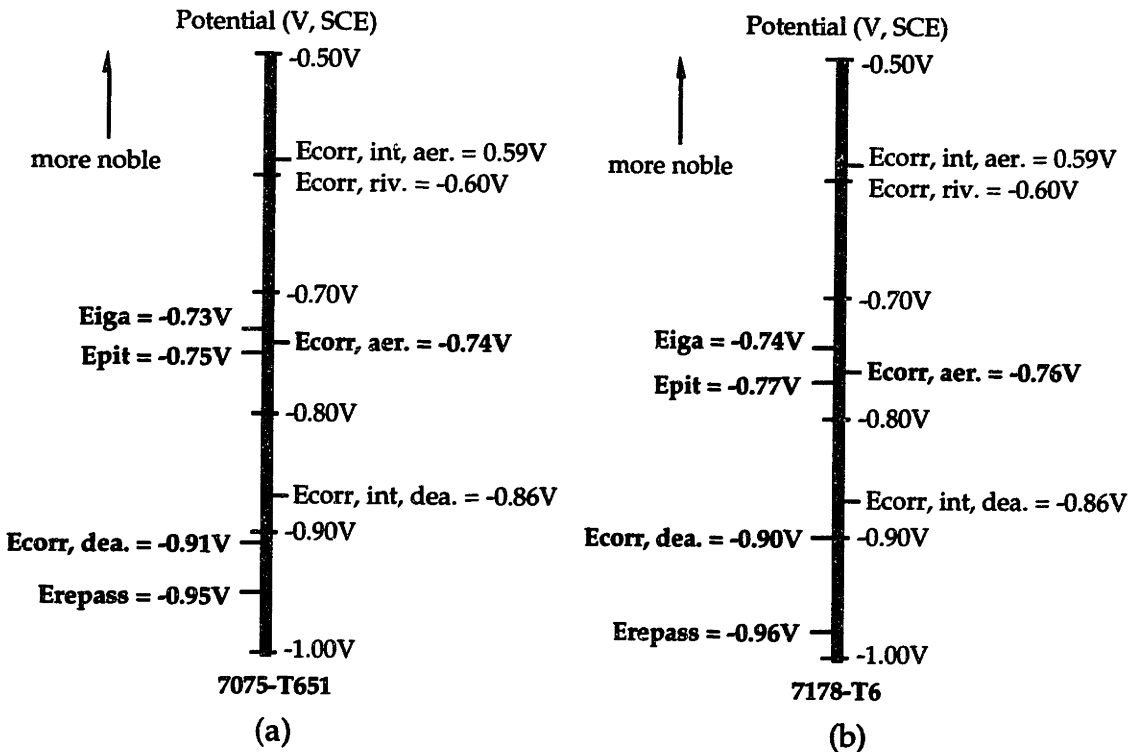

Figure 4.57. Schematic summary of the important electrochemical potentials for (a) 7075-T651 and (b) 7178-T6.

4.3 Mechanical / Environmental Behavior Testing

4.3.1 Tensile Tests

Tensile tests were conducted to obtain the 0.2% yield stress of the material. The results presented in Table 4.6 are the averages of at least two tests. The fracture surfaces for the two materials are shown in Figures 4.58 and 4.59.

Table 4.6. Tensile properties of the materials used.

Material	Orientation	Yield Stress (MPa)
7075-T651	Longitudinal	561
7075-T651	Transverse	571
7178-T6	Longitudinal	575
7178-T6	Transverse	598

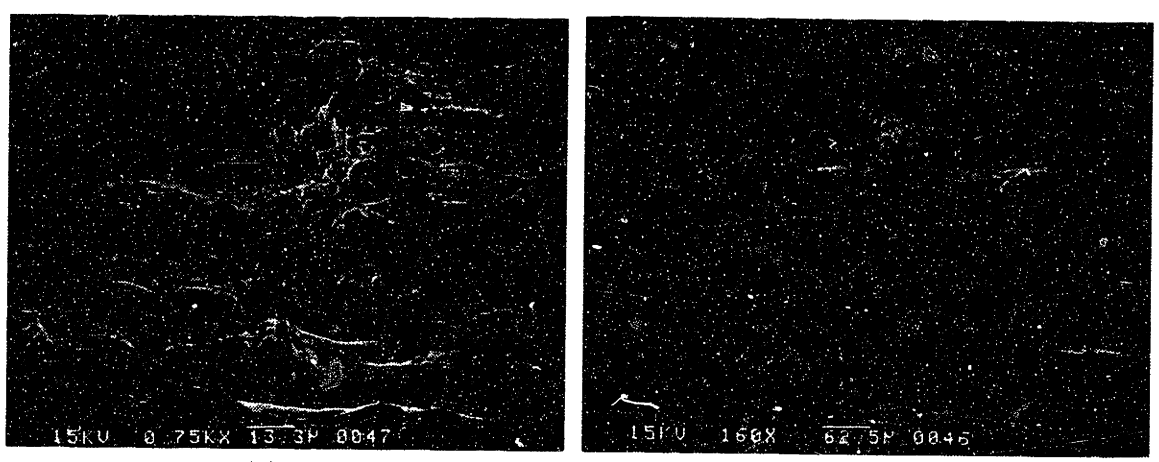

(a) (b)

Figure 4.58. Fracture surfaces from 7075-T651 tensile samples along the (a) longitudinal, (b) transverse direction.

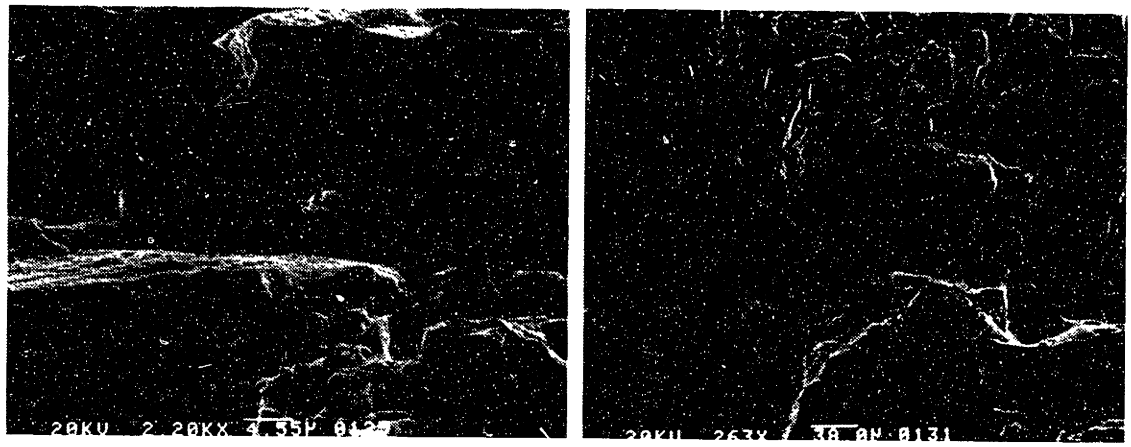

(a) (b)

Figure 4.59. Fracture surfaces from 7178-T6 tensile samples along (a) longitudinal, (b) transverse direction.

4.3.2 Stress Corrosion Cracking Tests

Stress corrosion cracking studies were conducted in 1.0M NaCl solution at 298K. The material was loaded to approximately 65% of yield. A potentiostat was used to maintain the potential above the lower breakdown potential, E_{pit}, but below the upper breakdown potential, E_{iga}. Hence, pitting was the only form of corrosion on these specimens. Figure 4.60 shows a 7075-T651 sample tested to failure in 1.0M NaCl solution under a constant tensile load of 3,540kg. This is equivalent to an initial tensile stress of 379 MPa. Only one longitudinal surface (the surface on the right of Figure 4.60 a) was exposed. All other surfaces were masked off with resin. High magnifications of the fracture surface (Figure 4.60 b and c) show little sign of ductility.

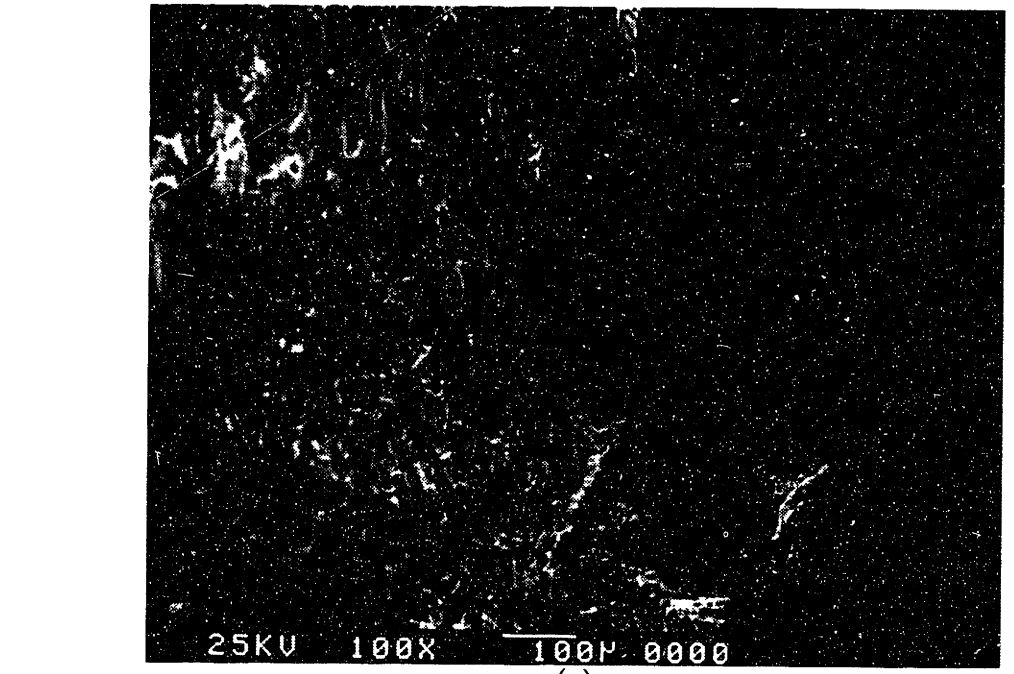

(a)

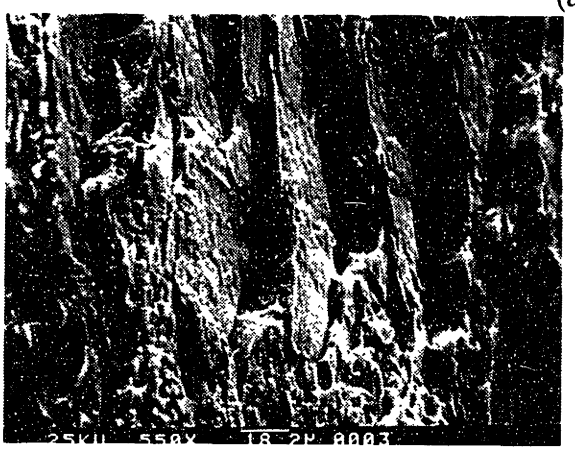

(b)

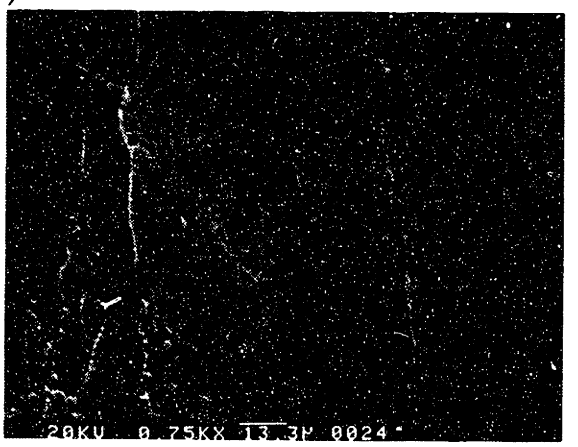

(c)

Figure 4.60. Fractograph of 7075-T6 in 1.0M NaCl solution under a constant tensile load of 3,540 kg•f.

A 7178-T6 4-point bend sample was tested in 3.0M NaCl solution at 298K. The potential was maintained at -0.810V SCE which is between the critical potentials in this environment. Only one surface of the specimen was exposed to the environment. The maximum tensile stress was 448 MPa (76% of 0.2% yield stress). After 48 hours, the test was stopped and the exposed surface examined. Figure 4.61 shows the surface examined. Pits were observed on the specimen surface. There was no sign of intergranular corrosion. The specimen was then pulled to failure in air and the fracture surfaces examined. Figure 4.62 and 4.63 show tensile fracture initiating from

corroded areas. The elliptical corroded sites are easily distinguishable from the subsequent tensile fracture. IGSCC was not observed in either one of these sites. Figure 4.63, on the other hand, shows a corroded site where IGSCC was observed. Facets similar to those depicted in Figure 4.60 b and c can be observed. Figure 4.64 shows the transition zone between IGSCC and subsequent tensile failure.

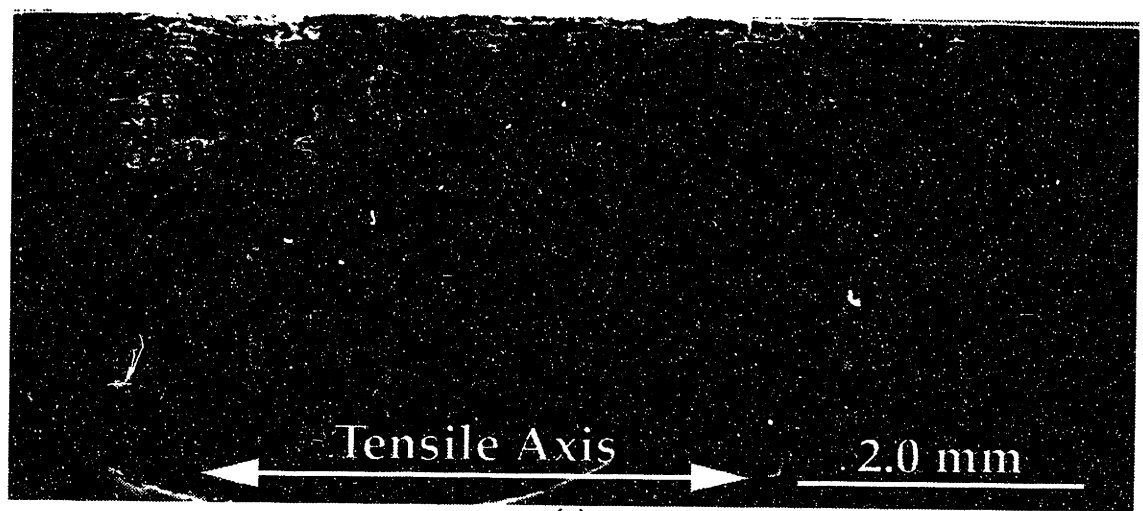

(a)

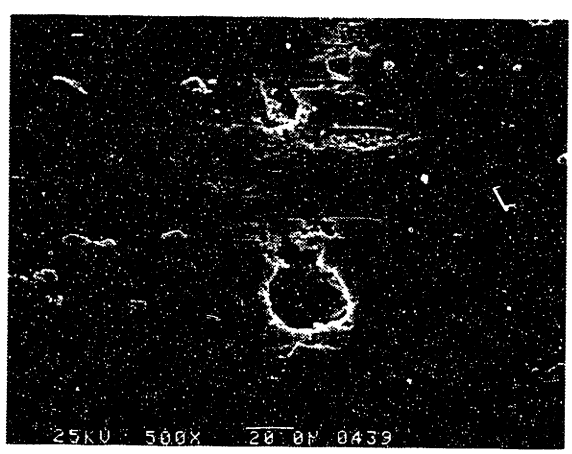

(b)

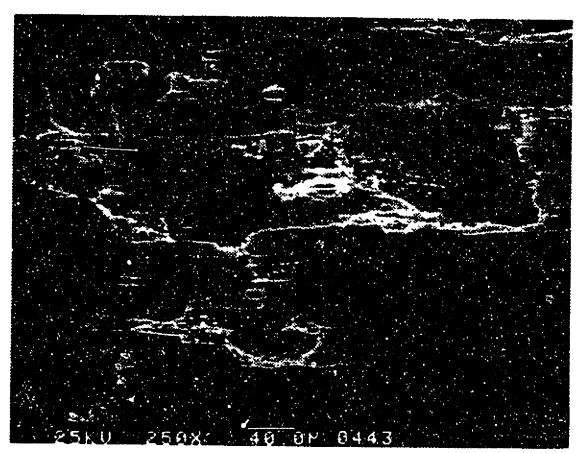

(c)

Figure 4.61. Examination of 7178-T6 4-point bend specimen tested in 3.0M NaCl solution for 48 hours. Figures b and c are high magnification images of typical corrosion observed on the exposed surface.

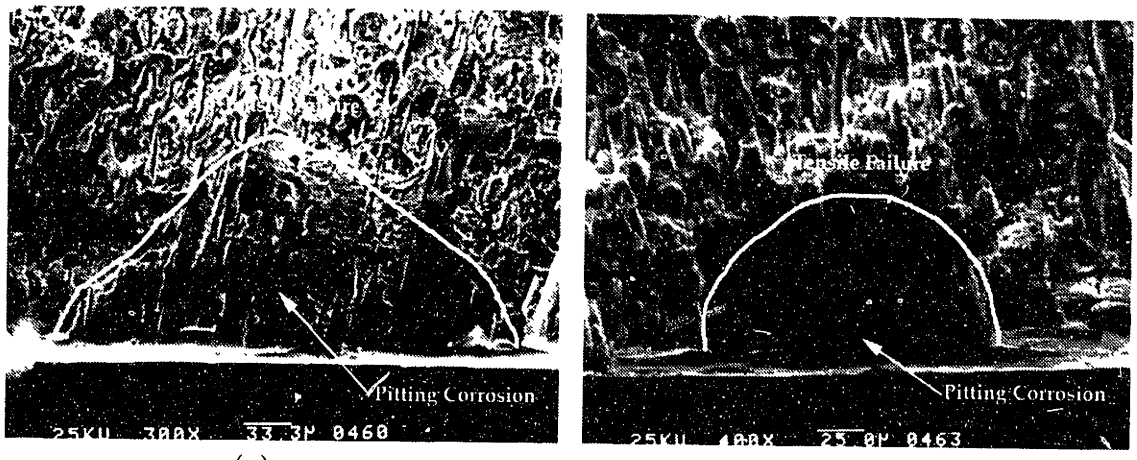

(a) (b)

Figure 4.62. Fracture surfaces of the same specimen depicted in Figure 4.61 after being pulled to failure in tension. (a) and (b) show tensile fracture along corroded sites. No SCC was observed in these areas.

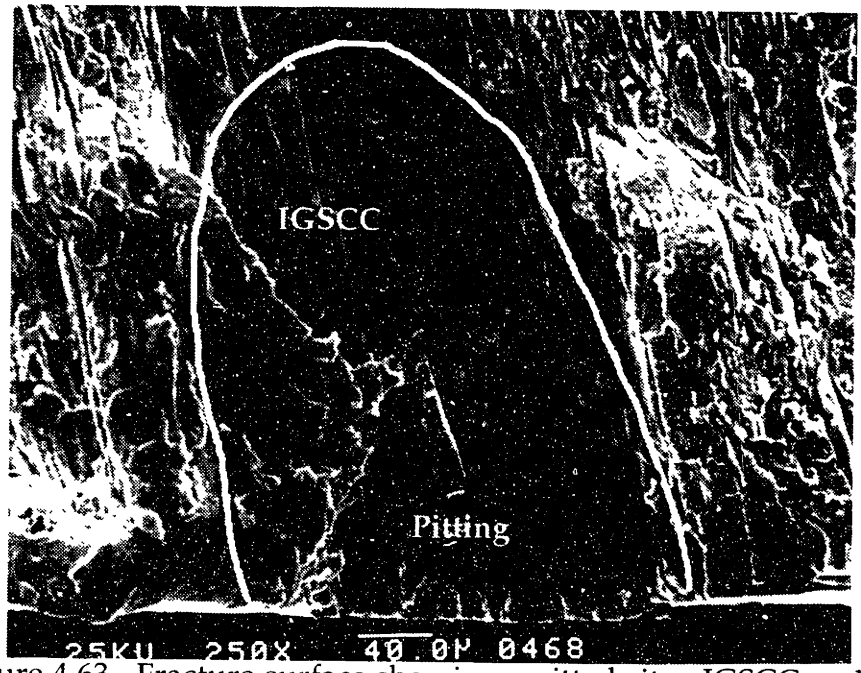

Figure 4.63. Fracture surface showing a pitted site. IGSCC and the subsequent tensile failure can be seen originating from the pit.

One half of the broken specimen was then mounted and polished for examination and is shown in Figure 4.65. Two cracks can be seen emanating from the pitted area. Figure 4.65 b shows the polished surface after etching. The cracks clearly follow the grain boundaries confirming the intergranular nature of these cracks. Figure 4.66 shows the same area under higher magnification.

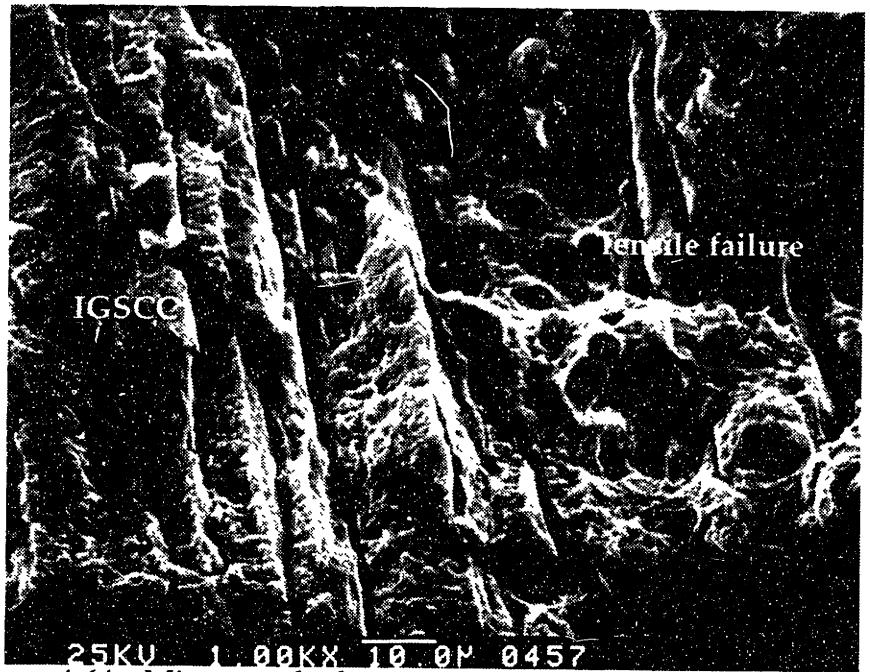

Figure 4.64. Micrograph showing the transition between IGSCC and tensile fracture.

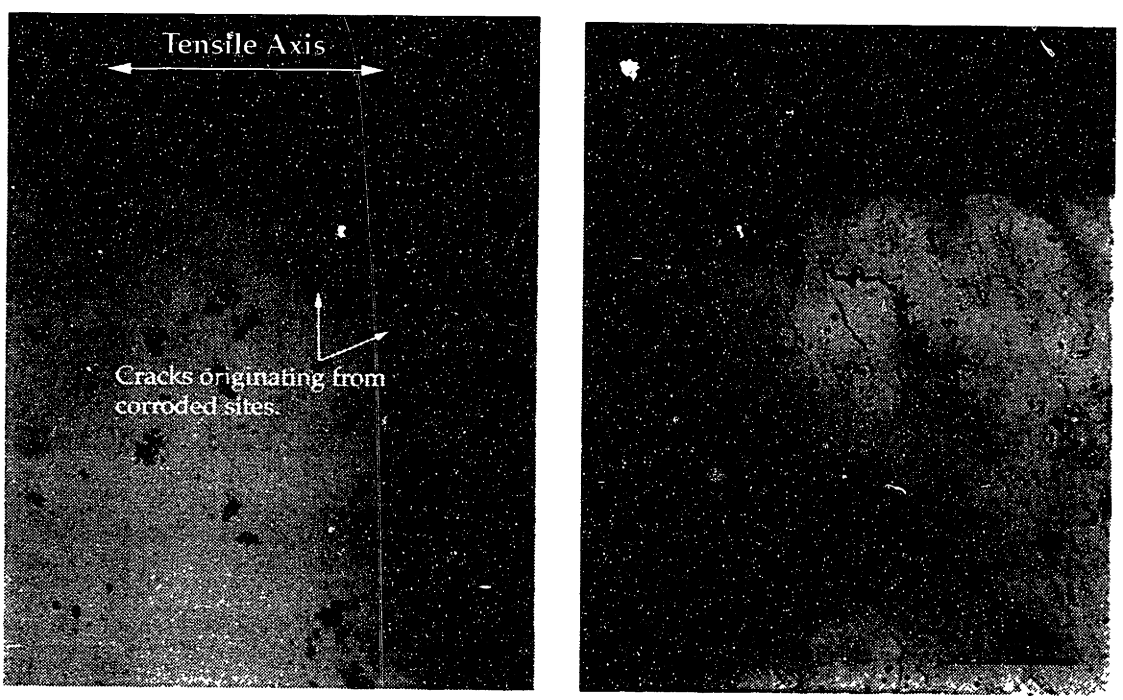

(a) (b)

Figure 4.65. Cross section of 7178-T6 fracture surface. The etched surface (b) indicates that cracking is intergranular. Note that only pitting occurred on the surface - no iga was observed.

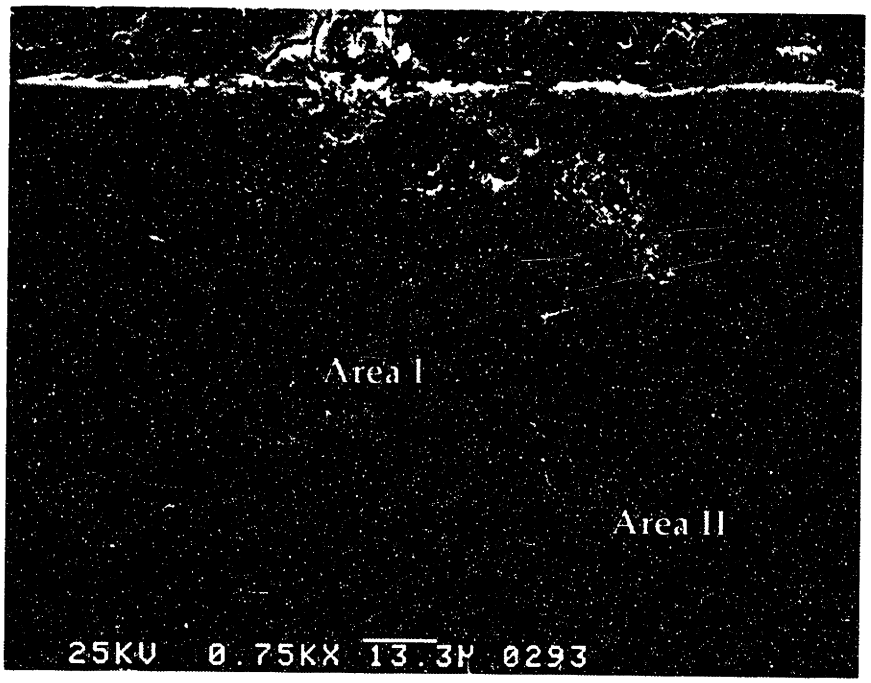

(a)

(b)

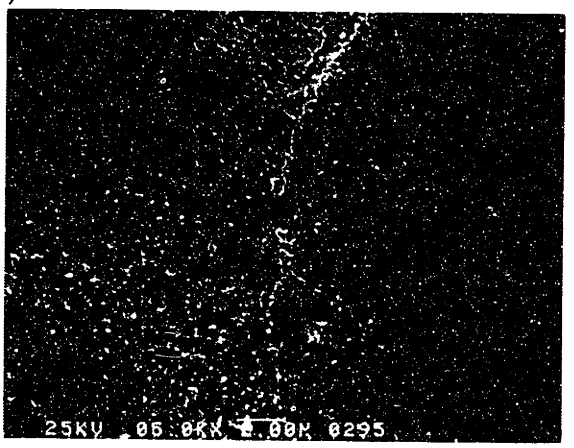

(c)

Figure 4.66. SEM micrographs of the sectioned fracture surface. Figures (b) and (c) are close ups of areas I and II in (a) respectively.

4.3.2.1 Stress Intensity Factor Calculations

The corroded areas in Figures 4.62 a, b and 4.63 were modeled as elliptical surface cracks. The stress intensity factor for this crack configuration under bending was calculated using the formulas presented by Newman and Raju [73] The idealized pit shape of an elliptical surface crack configuration is presented in Figure 4.67. The stress intensity factors were calculated as a function of position along the crack front and the definition of the parametric

angle used is given in Figure 4.68. Only half of the crack needs to be considered because of symmetry. The parameters used for the calculations are listed in Table 4.7.

Figure 4.64 shows the stress intensity factor as a function of the parametric angle for the three pits portrayed in Figures 4.62a, b, and 4.63. The stress intensity factors for the pits depicted in Figures 4.62a and 4.63 are above K_{ISCC} for this material.

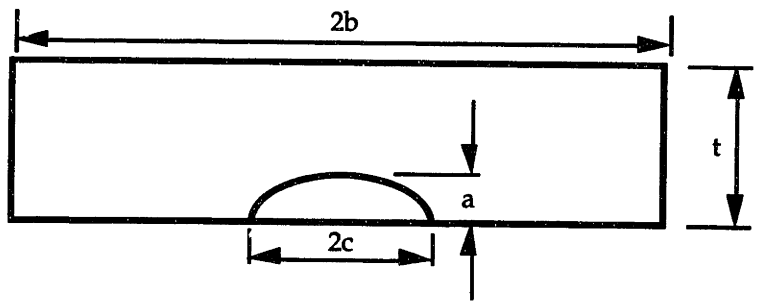

Figure 4.67. Schematic of an elliptical surface crack.

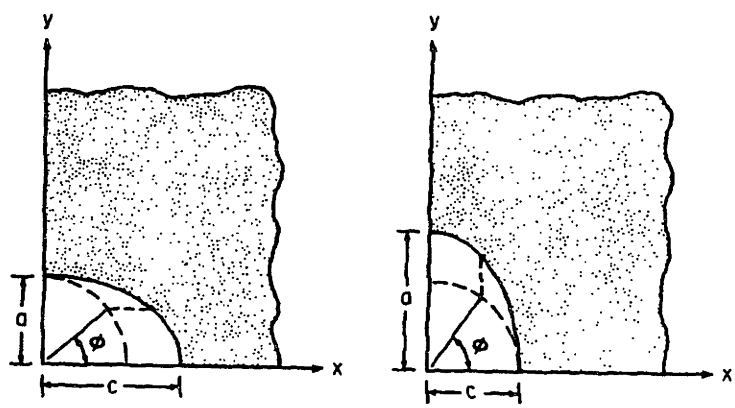

Figure 4.68. Coordinate system used to define the parametric angle, ϕ.[73]

Table 4.7. Parameters used to calculate stress intensity factors. The bending stress is 448 MPa.

Pit depicted in	a (μm)	c (μm)	c/a	t (cm)	b (cm)
Figure 4.62a	132	145	0.92	0.36	.15
Figure 4.62b	89	56	1.59	0.36	.15
Figure 4.63	135	150	0.91	0.36	.15

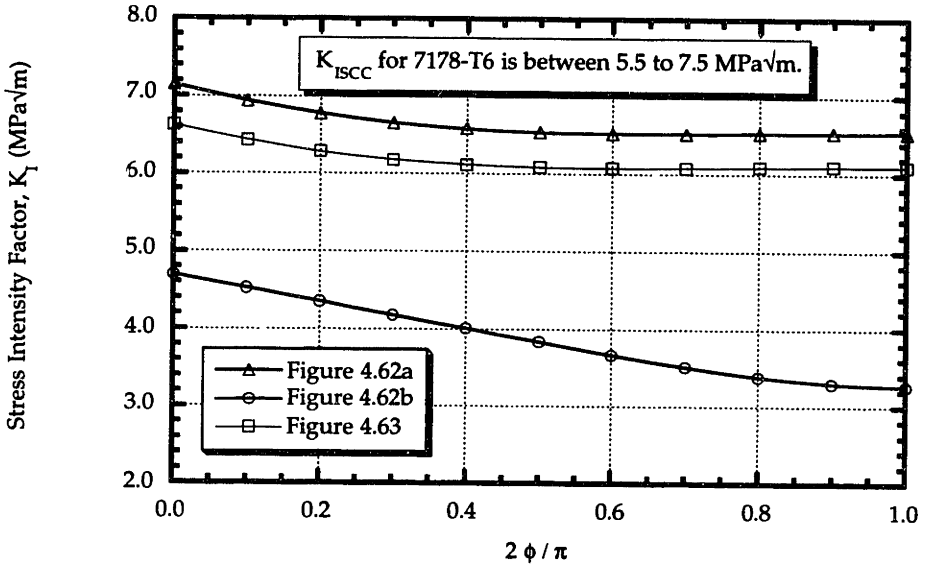

Figure 4.69. Plot of stress intensity factor as a function of the parametric angle for the three pits observed on the fracture surface.

5.0 Discussion

5.1 Polarization Behavior of the Alloys

Both 7075-T651 and 7178-T6 exhibit localized film breakdown in NaCl environments. Film breakdown leads to intergranular attack (IGA) and/or pitting. Breakdown however was not observed in 0.1M Na_2SO_4 solution. This lends support to Galvele et al.'s argument [18] that the breakdown is not simply the results of a galvanic cell but is related to the stability of the passive film on aluminum. Chloride ions play a critical role in establishing film stability.

It is important to first understand the significance of the film breakdown potentials at potentials more noble than the corrosion potential. The breakdown potential is defined as the potential where there is a significant increase in the current density. Since the film formed on individual phases (or even regions) in a material will differ in stability and hence, response to its environment differently, these phases/regions will exhibit distinct breakdown potentials. Indeed, while pitting and IGA are the consequences of breakdown in the materials studied, this need not be the case for other systems. If there are more than one metallurgical phase in the material and the phases are in significant quantity, there may be a distinct breakdown potential for each of these phases. This is in fact the case for the alloys 7178-T6 and 7075-T651 studied: corrosion around second phase particles (E_{pit}) and intergranular attack (E_{iga}) each has a unique initiation potential in the chloride environments examined. For both materials, E_{pit} is approximately 30mV more active than E_{iga} regardless of orientation, test temperature, and chloride ion concentration.

The breakdown potentials for 7178-T6 are consistently more anodic than that of 7075-T651 in the same environment. E_{pit} and E_{iga}, in various chloride ion concentrations at 25°C, are on average 19mV and 9.3mV respectively more active in 7178-T6. This is also reflected in the corrosion potential measurements during ASTM G69 tests. The corrosion potential for 7178-T6 was 11mV more active than that of 7075-T651. These measurements are in accordance with the data reported by Burleigh et al.[74] Alloying elements,

when they are in solid solution, can have large effects on the corrosion potential of aluminum alloys. This is especially true for copper and zinc [74] and is illustrated in Figure 5.1. Increasing the zinc content lowers the corrosion potential to more active values while copper has the opposite effect. The zinc content in the 7178-T6 alloy is 1% higher than that of the 7075-T651 (6.4% vs. 5.3%). At the same time, the copper content in 7178-T6 is only slightly higher than that of 7075-T651 (1.9% vs. 1.5%). It is therefore reasonable to expect the net effect of these compositional differences is the lowering of the potentials in 7178-T6 to more active values due to its higher zinc content.

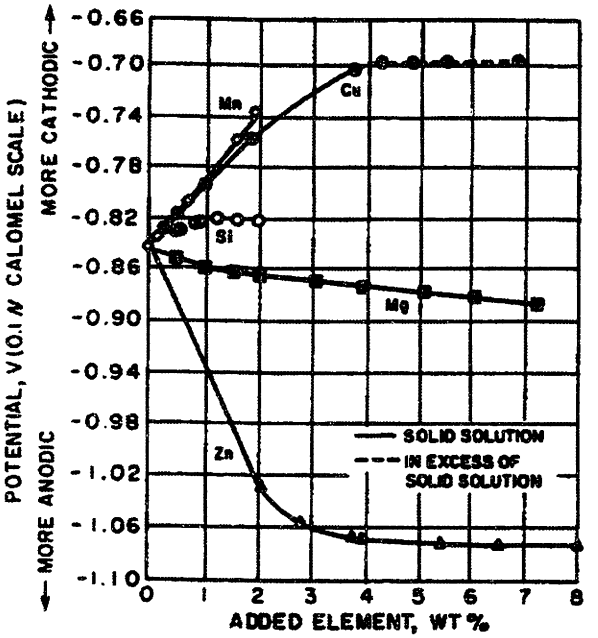

Figure 5.1. Effects of principal alloying elements on the solution potential of Al binary alloys in NaCl – H_2O_2 solution at 25°C.[17]

For the alloys studied, the polarization behavior is not strongly influenced by the scan rate. The critical potentials (E_{pit} and E_{iga}) obtained from tests with a scan rate of 1mV/min is virtually identical to those from 10mV/min experiments. As a result, a scan rate of 10mV/min was used for all dynamic polarization experiments. The breakdown potentials were then obtained as a function of orientation, chloride ion concentration, and test temperature.

The critical pitting potential for numerous alloy systems are often found to have a logarithmic dependence on the chloride ion concentration or

activity.[22, 24, 75] The data reported in the literature are usually in the form of:

$$E_{pit} = A + B \log [Cl^-] \qquad (5.1)$$

and B is found to depend on the composition of the supporting electrolyte, the measurement technique, and the metal involved.[25] In the case of aluminum alloys, B has been reported to be in the range of 0.05 to 0.13V.[18, 26] This is true for the alloys examined in this study. The pitting potential shows a logarithmic dependence on the chloride ion activity and B is found to be on average 0.077 and 0.081V for 7075-T651 and 7178-T6 respectively. This is well within the range of values found in published literature.

The breakdown potentials for both materials are linearly dependent on the reciprocal of the absolute test temperature. An increase of 25°C shifts the breakdown potentials roughly 30mV in the active direction. This indicates that pitting and intergranular corrosion resistance of these materials decreases with increasing temperature.

There does not appear to be a strong correlation between the critical potentials and orientation. The variations in critical potentials between the different orientations is well within the scatter of experimental measurements.

With the knowledge that the critical potentials follow a logarithmic relationship with chloride ion activity and are linearly dependent on the reciprocal of the absolute temperature, E_{pit} and E_{iga} can be predicted in various environments. An understanding of the conditions necessary for pitting/IGA has both practical as well as scientific implications. Since stress corrosion cracking (SCC) is often preceded by pitting (cracks initiate from pits), preventing pitting will significantly improve a material's response to stress corrosion cracking. On the scientific (fundamental) side, the ability to reproduce these conditions in a laboratory setting allows one to study the initiation process in a more controlled environment. The ability to control the form of localized breakdown is crucial to the task of reproducing stress corrosion cracks which originate from pits in a laboratory setting. With a thorough understanding of the interactions between these environmental parameters and the corrosion behavior of the alloys, it is possible to generate

materials with pits and no intergranular corrosion. For example, the material can be polarized to a potential above E_{pit} but below E_{iga}. As a result, only pits can form. In the presence of a tensile stress, SCC may initiate from these pitted sites. Hence, this understanding of the interactions between the macroscopic parameters and the corrosion properties of these materials forms the back bone of the SCC studies.

In a deaerated environment, neither pit nor IGA can occur spontaneously on 7178-T6 and 7075-T651 because the corrosion potential for these materials in deaerated conditions ($E_{corr, dea}$) are more active than the corresponding breakdown potentials. This is illustrated in Figure 5.2 a and b where $E_{iga} > E_{pit} > E_{corr, dea}$. In an aerated environment, the cathodic current density for these materials increases by approximately one order of magnitude. This is caused by the added oxygen reduction reaction in the aerated environment. The anodic reaction rate, on the other hand, is not affected by the addition of oxygen. As a result, the corrosion potential of the alloys is more noble in the aerated environment. The corrosion potential of 7178-T6 increases from -0.90V to -0.76V SCE when oxygen is present. Similarly, the corrosion potential of 7075-T651 increases from -0.91V in the deaerated case to -0.74V in aerated conditions. The increase in corrosion potential in the presence of oxygen results in a potential that is noble to the pitting potential for both alloys while still being active to the IGA potential. This is shown in Figure 5.2 a and b where the corrosion potential in the aerated environment ($E_{corr, aer.}$) is in between their corresponding breakdown potentials (E_{pit} and E_{iga}). That is, $E_{iga} > E_{corr, aer.} > E_{pit}$. This implies that pits can form spontaneously on both materials in aerated chloride environments while IGA cannot occur. In other words, neither pitting nor IGA should be observed on 7178-T6 and 7075-T651 in deaerated environments while the addition of oxygen to the electrolyte can cause pits to form spontaneously.

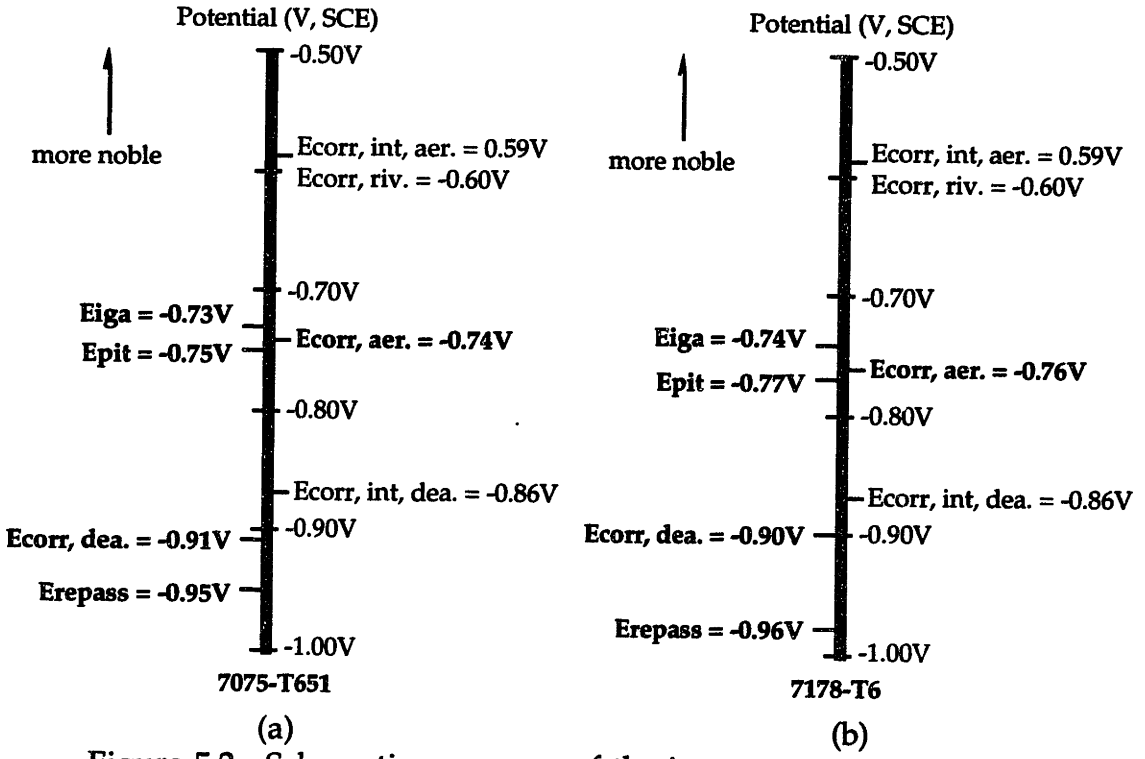

Figure 5.2. Schematic summary of the important electrochemical potentials for (a) 7075-T651 and (b) 7178-T6.

Once localized breakdown has occurred, the potential must decrease beyond (more active than) the repassivation potential (E_{repass}) before repassivation can occur. The repassivation potential for both 7178-T6 and 7075-T651 are more active than their corresponding free corrosion potential in both aerated and deaerated solutions ($E_{corr,aer.}$ and $E_{corr,\ dea.}$). This is demonstrated in Figure 5.2 where $E_{corr,\ aer} > E_{corr,dea.} > E_{repass}$. In other words, once localized breakdown has occurred, active dissolution continues because none of these materials can repassivate spontaneously. This is especially troubling in aerated solutions where pits can form spontaneously on both materials. The difference between E_{corr} and E_{repass} is less pronounced in 7075-T651. This suggests that 7075-T651 may have a better chance of repassivation than 7178-T6. Even if repassivation can occur, the large hysteresis loop in the repassivation behavior of both materials implies that significant corrosion can occur before repassivation.

5.2 Constituent Particles

Based on the static polarization experiments, it is obvious that second phase particles play a significant role in localized corrosion of aluminum alloys. E_{pit}, for example is related to the dissolution of the matrix at the interface between the matrix and the constituent particles. In order to gain an insight into the role of these particles, five intermetallic alloys that are representative of the constituent particles found in commercial grade aluminum alloys were produced in bulk for this thesis work. The composition and crystal structure of these alloys were confirmed by EDX and X-ray diffraction phase analysis. In the case of Al_3Fe, the crystal structure could not be confirmed due to a lack of information in the published literature. The chemical composition however, is well within the specified limit. It can therefore be concluded that the intermetallic alloys produced are representative in both chemical composition and crystal structure of the constituent particles found in commercial grade aluminum alloys.

The polarization behavior of these alloys was studied in both aerated and deaerated chloride solutions. Results from these experiments provided the much needed electrochemical data of these alloys. The corrosion properties of $CuAl_2$ have been studied before. It has been reported that $CuAl_2$ is cathodic in relation to the Cu depleted zones in aged Al-4%Cu alloys.[18] It has also been reported that $CuAl_2$ can dissolve up to 2-3% of Zn.[69] Since Zn can drastically lower the corrosion potential of aluminum alloys, it is worthwhile to investigate the effect of Zn on the corrosion properties of $CuAl_2$ itself. Hence, three intermetallics were produced with varying amounts of Zn (from 0 to 1.6%). The free corrosion potential for these materials in deaerated 1.0M NaCl at 298K varied from a high of -0.85V to a low of -0.88V SCE. This is well within the scatter of corrosion potential measurements. The polarization behavior of these materials are also indistinguishable from each other. Furthermore, the cathodic polarization behavior of $CuAl_2$ in aerated 1.0M NaCl published by Galvele et al. [18] is identical to that of Al_2Cu+Zn from this work. It can therefore be concluded that Zn addition does not significantly alter the electrochemical properties of the phase $CuAl_2$.

The corrosion properties of aluminum alloys can be modeled as a combination of the electrochemical behavior of the constituent particles and

pure aluminum. Once the electrochemical properties of individual components are known, mixed potential theory can be applied to predict the behavior of the alloy as a whole. The intermetallics were manufactured to simulate the composition as well as the crystal structure of the constituent particles. Dynamic polarization scans were then conducted on pure aluminum and the intermetallics in both aerated and deaerated chloride solutions. The potential - current relations for these materials are extracted from the Tafel plots. This data are then combined in accordance with the mixed potential theory and used to predict the corrosion behavior of aluminum alloys.

Aluminum is protected by an oxide film in the pH and potential range of interest. The current density is therefore virtually independent of the potential. This is reflected by the steep slope in the anodic polarization behavior for aluminum before the breakdown. Hydrogen reduction on the surface of the intermetallics, on the other hand, is not hindered. Slight cathodic polarization produces a relatively large increases in the cathodic current. In other words, the cathodic polarization plot has a very shallow slope while the anodic polarization curve has a very steep slope. This is consistent with the development of an anodically controlled system where polarization occurs mostly at the anode and the corrosion potential is close to the open circuit potential of the cathode. Thus, the corrosion potential of a couple between aluminum and the intermetallic phase quickly approaches the open circuit potential of the intermetallics.

The corrosion potential for all the intermetallics are above (more noble than) -0.9V SCE while the corrosion potential for pure aluminum is roughly -1.3V SCE. In other words, the corrosion potentials of all the intermetallic alloys in 1.0M NaCl at 298K are more noble than that of pure aluminum. Furthermore, hydrogen ion reduction is accelerated on the surface of these intermetallics. Table 4.2 shows that the exchange current density of hydrogen reduction for the intermetallics is on average two orders of magnitude higher than that of pure aluminum ($3x10^{-9}$ vs. $7x10^{-11}$ A/cm^2). Since the reduction of hydrogen ions is more rapid on the intermetallics, and the free corrosion potential of the intermetallics are more noble than that of aluminum, it is clear that the intermetallics will act as cathodes when they are coupled with

pure aluminum. Figure 5.3 shows that when the samples are electrically coupled, the cathodic current on the intermetallics is roughly two orders of magnitude higher than that of pure aluminum (10^{-7} vs. 10^{-9} A/cm^2). The anodic dissolution rate on aluminum increases accordingly (from 10^{-8} to 10^{-7} A/cm^2) as the coupled system must remain electrically neutral. These predictions are verified by the galvanic experiments where increasing the area fraction of the intermetallics polarizes the pure aluminum to more noble potentials.

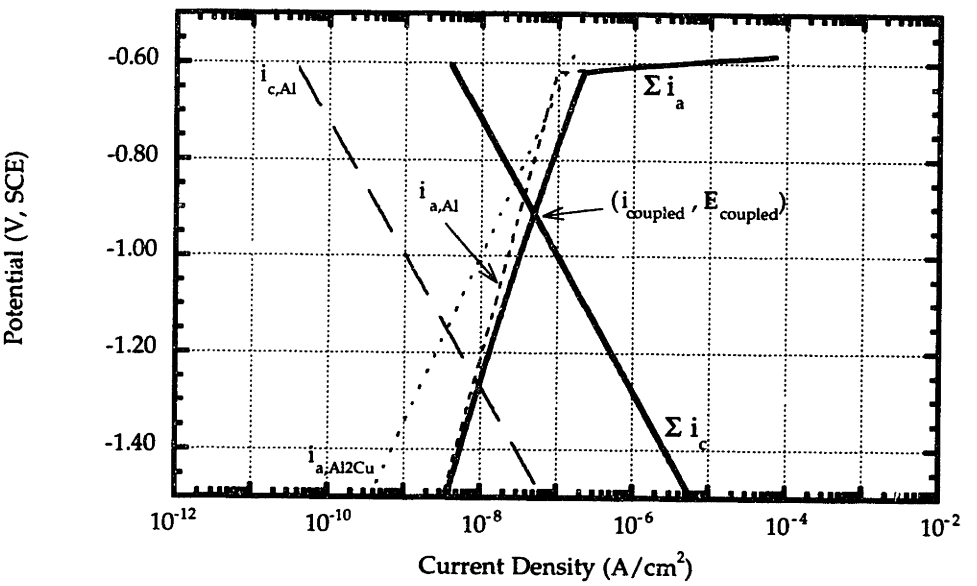

Figure 5.3. Calculation of free corrosion potential of coupled Al and Al_2Cu in deaerated 1.0M NaCl solution at 298K. (Area fraction of Al_2Cu = 0.5)

The mixed potential theory does not take into the account the possibility of secondary reactions between the cathode and the anode, such as the formation of a protective oxide film. In other words, the corrosion potential calculated from the mixed potential theory is bounded by the free corrosion potential of the components. In this case, the calculated free corrosion potential for these couples are between that of pure aluminum and the intermetallics. There is good agreement between the calculated corrosion potential and that from galvanic experiments. It can therefore be concluded that no secondary reaction occurred between the alloy systems and the mixed

potential theory is successful in predicting the corrosion behavior of pure aluminum - intermetallics couples.

Although Al_2Cu + Zn alloys have the most noble corrosion potentials among all the intermetallics, their corrosion potentials in deaerated 1.0M NaCl environment are over 0.15V more active than the breakdown potential of aluminum. In other words, the corrosion potential of Al - intermetallics couples are more active than the breakdown potential of Al regardless of the area fraction of the intermetallics. This is illustrated graphically in Figure 5.4 where the coupled potential is always more active than -0.70V SCE, the breakdown potential of Al. This implies that **the intermetallics cannot cause localized breakdown in aluminum under deaerated conditions.** In aerated environments, the corrosion potential of pure aluminum and the intermetallics become more noble because of the added oxygen reduction reaction. As demonstrated in Figure 5.5, the corrosion potential of Al - intermetallics couples can become more active than the breakdown potential of aluminum. In other words, **when the intermetallics are electrically coupled to aluminum in aerated electrolytes, localized breakdown can be expected.**

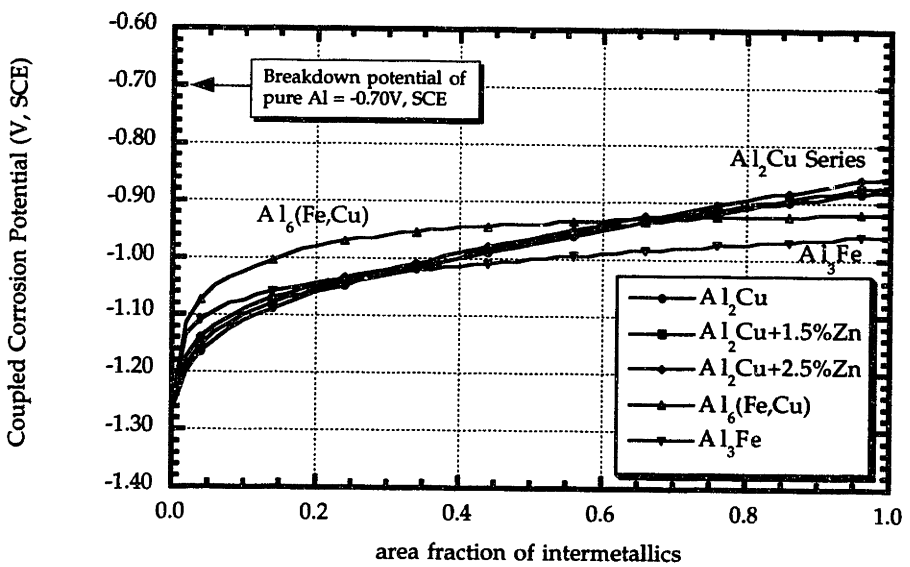

Figure 5.4. Calculated corrosion potential of intermetallic - pure Al couples in deaerated 1.0M NaCl solution at 298K.

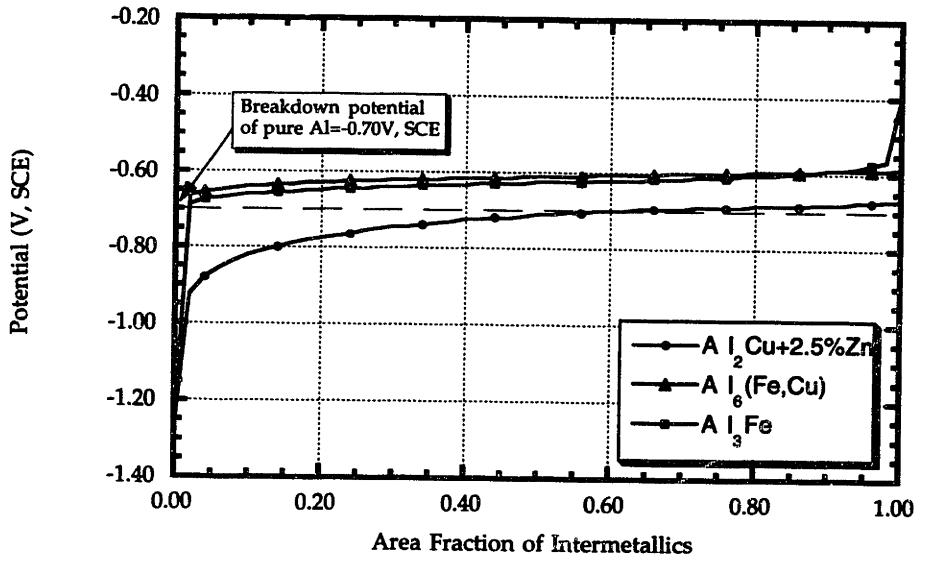

(a)

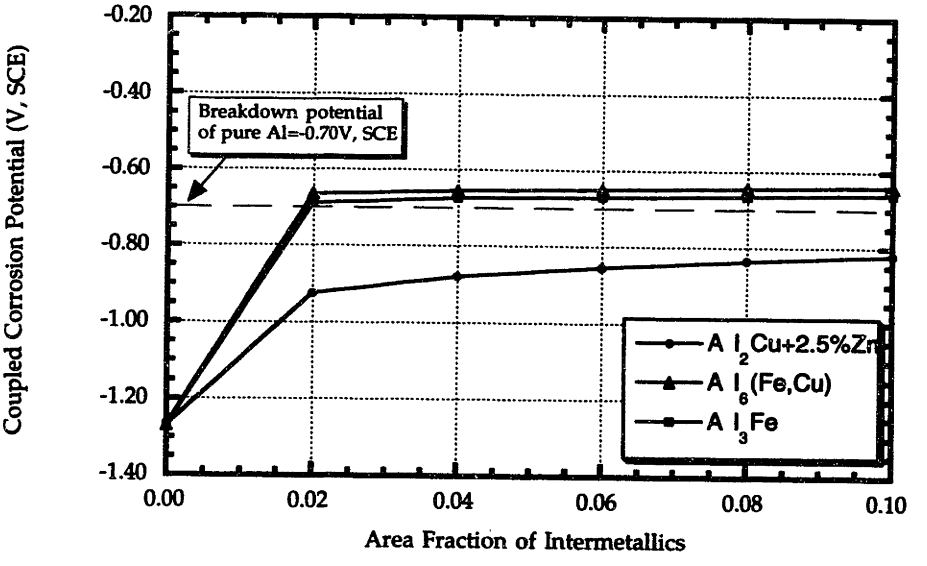

(b)

Figure 5.5. Calculated corrosion potential of intermetallic - pure Al couples in aerated 1.0M NaCl solution at 298K. Figure b is a magnified view of these calculations when the couples are predominantly aluminum.

Figure 5.5b is a magnified view of the calculated corrosion potential of aluminum - intermetallics couples when the coupled samples are predominantly aluminum. This reflects the condition found in commerical aluminum alloys where the volume fraction (area fraction) of constituent particles ranges from 0.1% to 3%. The benefit of improving the purity of aluminum alloys is clearly demonstrated. When the area fraction of intermetallics is less than 2%, the Al-intermetallics coupled corrosion potential is more active than the breakdown potential. In other words, localized corrosion around constituent particles can be prevented if the volume fraction of the constituent particles is less than 2%.

Hübner et al. [21] observed that the electrolyte must contain dissolved oxygen for pits to initiate in commercial aluminum alloys. Hydrogen reduction by itself cannot cause localized breakdown. They reported that once pitting has begun however, hydrogen reduction is enough to sustain the dissolution reaction. **The results from this work provide a mechanistic explanation to Hübner's observation**. Recall that the pure aluminum - intermetallics studies indicate that the intermetallics by themselves cannot polarize the matrix above the breakdown potential in deaerated environments. The intermetallics, however, can cause localized breakdown in aerated solutions. This is the exact observation reported by Hübner et al. In other words, the matrix adjacent to the constituent particle is polarized above the breakdown potential and pitting can therefore occur. Once breakdown has begun, the potential must be lowered beyond E_{repass} (more active than E_{repass}) before repassivation can occur. The cyclic polarization data for 7178-T6 and 7075-T651 indicates that the corrosion potential of these materials are more noble than E_{repass}. This is summarized in Figures 5.2 a and b where the corrosion potential in both aerated and deaerated conditions are more noble than the repassivation potential ($E_{corr, aer.} > E_{corr, dea.} > E_{repass}$). In other words, these materials will not spontaneously repassivate in either aerated or deaerated environments and active dissolution continues. Hence, hydrogen reduction alone is enough to sustain the pitting reaction after pitting has initiated.

Recall the objective of the pure aluminum - intermetallics experiments is to model the corrosion properties of aluminum alloys according to the mix potential theory as a combination of the electrochemical behavior of the

constituent particles and pure aluminum. Considering the good fit between Hübner's observation on commercial aluminum alloys and the prediction made from the pure aluminum - intermetallics studies, it can be concluded that modeling the corrosion behavior of aluminum alloys as a combination of the constituent particles and pure aluminum is not only a valid approach, but also a successful and useful one.

5.3 Riveted Joints

Steel rivets are often used in wing joints because of the higher strength requirements. This configuration presents the situation of electrically coupling two dissimilar metals: the steel rivet and the aluminum panel. In deaerated conditions, the corrosion potential of the steel rivet is roughly 0.5V more noble than that of the wing panel, the 7178-T6, and the 7075-T651 plates. Furthermore, the exchange current density for the hydrogen reduction on the steel rivet is on average one order of magnitude higher than that of the aluminum alloys (1.1×10^{-7} vs. 2.5×10^{-8} A/cm^2, Table 4.4). In other words, not only is the steel rivet more noble than the aluminum alloys, it is also more effective at reducing hydrogen ions. The steel rivet will therefore act as the cathode when it is electrically coupled to the aluminum alloys while the aluminum alloys will be the anode. The cathodic current density of the coupled sample is higher than that of the aluminum alloy by itself because of the steel rivet's higher capacity for hydrogen reduction. The anodic current density in the coupled sample must increase accordingly as the coupled sample must remain electrically neutral. As a result, the aluminum alloy is polarized to more noble potentials when it is electrically coupled to the steel rivet. The amount of polarization increases as the area fraction of the rivet in the coupled sample increases. In other words, the corrosion potential of the coupled sample in deaerated environments approaches that of the steel rivet as the area fraction of the rivet increases.

Mixed potential calculations suggest that when the area fraction of the rivet exceeds approximately 0.9, the corrosion potential of the coupled sample in deaerated environments will be more active than the breakdown potentials (E_{pit} and E_{iga}) of the aluminum alloys. **Pitting and intergranular corrosion can therefore occur in the immediate vicinity of the steel rivet in deaerated chloride environments.** As pointed out in Section 5.1 earlier, these materials

cannot repassivate spontaneously. Once localized breakdown has occurred, active dissolution continues.

When the electrolyte is aerated, in addition to the hydrogen reduction reaction, the reduction of oxygen becomes possible. Compared to the aluminum alloys, the steel rivet is much more effective at reducing oxygen (Figure 4.49 and Table 4.4). The exchange current density for oxygen reduction on the rivet is on average three orders of magnitude higher than that of the aluminum alloys (1.7×10^{-8} vs. 1×10^{-11} A/cm^2). In other words, the steel rivet remains as the cathode in the rivet - aluminum panel coupled sample. Because of the added oxygen reduction reaction, the corrosion potential of the rivet and the aluminum alloys assume more noble values as compared to the deaerated situation. The corrosion potentials of the aluminum alloys, in aerated environments, are more noble than their E_{pit} but more active than E_{iga}. In other words, pits can form spontaneously on these alloys while intergranular attack cannot occur when the electrolyte is aerated. **When these alloys are electrically coupled to the steel rivet, they are polarized to more noble values because of the added oxygen reduction capacity on the steel rivet. As a result, the corrosion potential of the coupled sample becomes more noble than the E_{iga} of the aluminum panel.** That is, when the aluminum alloy is by itself in aerated electrolytes, only pits can form. When it is electrically coupled to the steel rivet however, both pitting and intergranular corrosion can occur.

The results from these steel rivet - aluminum alloy coupled experiments provide an explanation for the type and the extent of corrosion observed on the two dismantled joints from a replaced B52 wing panel shown in Figures 3.1 and 3.2. The steel rivets in both joints were not corroded. Pitting and intergranular corrosion was observed on the countersink area of one of the aluminum panels while the other was intact. These observations are consistent with the laboratory results. The steel rivet, acting as the cathode in the rivet - aluminum panel coupled system, should not be corroded. The aluminum panel, on the other hand, is the anode. Because of the polarizing effects of the steel rivet, the corrosion potential in the vicinity of the rivet can be more noble than both E_{pit} and E_{iga} of the aluminum alloy. Localized breakdown can therefore occur spontaneously when a conductive electrolyte

penetrates the joint. As a result, it is not surprising to see pits and IGA at the countersink area of the steel riveted joint which are depicted in Figure 3.2 c and d.

The results of electrically coupling pure aluminum or aluminum alloys to the constituent particles and the steel rivet are summarized in Table 5.1.

Table 5.1. Summary of the results when aluminum alloys are electrically coupled to constituent particles and the steel rivet used in wing joints.

	Deaerated environment	Aerated environment
Coupled with constituent particles	No localized breakdown	Localized breakdown
Coupled with steel rivet	Pitting and IGA	Pitting and IGA
Spontaneous repassivation	No	No

5.4 SCC Initiation from Pits

Numerous SCC studies have been conducted on these high strength aluminum alloys using either the ASTM G69 solution (58.5 ± 0.1 g NaCl and 9 ± 1 ml of 30% H_2O_2 per 1 L of aqueous solution, this solution is 1M with respect to concentration of NaCl) or the 3.5% NaCl solution. Both these electrolytes rely on chemical means to maintain the electrochemical potential. The hydrogen peroxide in the ASTM G69 solution, for example, increases the cathodic reaction kinetics by raising the level of dissolved oxygen in the electrolyte. As a result, the potential is raised to more noble values. There are several drawbacks in applying this method to SCC tests. First, the electrochemical potential cannot be maintained for long periods of time by chemical means. As the solution ages, the electrochemical potential will vary. The corrosion potential of 7178-T6, for example, dropped roughly 7mV during the two hour ASTM G69 test when the added hydrogen peroxide was gradually consumed by the cathodic reaction. Typical SCC test can last for hours, if not days. Continuous maintenance of the electrochemical for the duration of SCC tests by chemical means is therefore unfeasible. Second, the electrochemical potential cannot be controlled precisely by chemical means. In order to reproduce the phenomenon of IGSCC initiating from pits, it is critical to be able to generate corroded surfaces with only pits and no

intergranular attack. This implies that the potential must be more active than E_{iga} but more noble than E_{pit}. In other words, the potential must be controlled within roughly a 20mV range. This is not possible by chemical means. As a result, all the SCC tests conducted in this work were done with a potentiostat where the electrochemical potential could be maintained precisely and indefinitely.

Stress corrosion cracking is the synergistic interaction between tensile stress and corrosion acting on a susceptible environment in a specific environment. In the case of these high strength aluminum alloys, stress corrosion cracks propagate along the grain boundaries. Intergranular stress corrosion cracks (IGSCC) have been observed to initiate from pitted sites on the countersink and bore area of wing joints.[1] The goal of the SCC tests in this thesis work was to reproduce and understand the phenomenon IGSCC initiating from pits.

A thorough understanding of the interaction between the macroscopic environmental variables and the corrosion behavior of 7075-T651 and 7178-T6 is made possible by the results of the dynamic polarization studies. This enables one to generate samples with only pitting corrosion but no intergranular attack. Figure 5.6 demonstrates that this goal was successfully accomplished as the sample was pitted only and no sign of intergranular corrosion was observed. Concurrent to the corrosion reaction, a bending load was applied to the sample. As a result, tensile stresses were generated on the top surface of the specimen. After being in this configuration for 48 hours, the test was terminated and the specimen was then pulled to failure in air. The fracture surfaces indicate that IGSCC has initiated at some of the corroded sites.

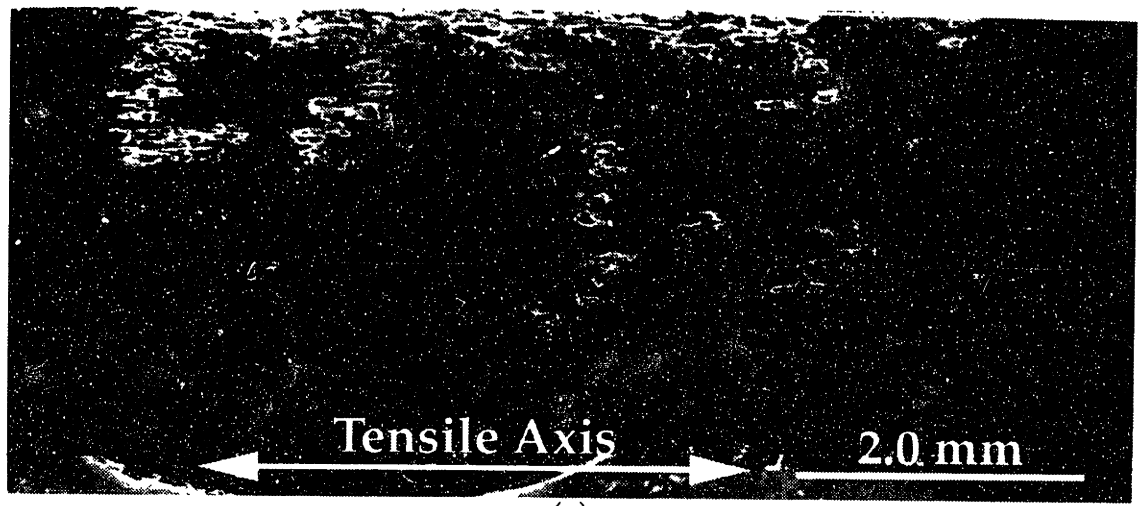

(a)

(b)

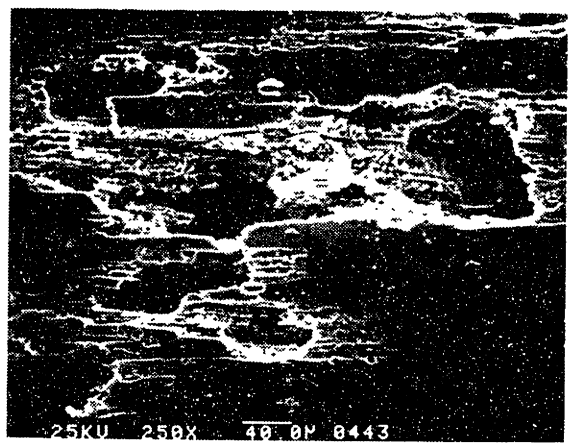

(c)

Figure 5.6. Examination of 7178-T6 4-point bend specimen tested in 3.0M NaCl solution for 48 hours. Figures b and c are high magnification images of typical corrosion observed on the exposed surface.

The goal was then to understand why IGSCC has formed in only some of the pitted sites and not in others. It is important to first understand the sequence of events leading up to IGSCC. When the stress intensity factor at the corroded site exceeds a threshold (K_{ISCC}), the stress corrosion crack can be expected to grow at an appreciable rate. The pitting process however, is still active. In other words, **pitting and crack growth are competitive processes and the one with a higher growth rate will dominate**. The kinetics of pit growth usually diminishes with time. The pit depth is often fitted to a power growth equation where

$$d = kt^n \quad (5.1)$$

where

d : pit depth at time t
k : kinetics constant
t : time
n : coefficient of power law (less than 1, in the order of 1/3)

Crack growth rate, on the other hand, accelerates as the stress intensity factor increases. In other words, pitting has a higher growth rate in the early stages and SCC dominates at a later time. A transition from pitting to SCC can therefore be expected. Based on the above discussion, several events must occur before this transition can be observed. Since the stress corrosion crack is intergranular in nature for these alloys, the corroded site where IGSCC may initiate must be in the vicinity of a grain boundary. This allows a growing pit to come into contact with a grain boundary. If the stress intensity is high enough such that the IGSCC growth rate is higher than the corrosion rate, a transition from pitting to IGSCC can be observed. When the crack growth rate is too low, or when the corroded site is not in the vicinity of a grain boundary, this transition from pitting to IGSCC will not occur.

Figure 5.7 a and b show two corroded sites where the transition from pitting to IGSCC has not occurred. Calculations show that the stress intensity factor for the pit shown in Figure 5.7b is below K_{ISCC}. Hence, corrosion should be the only form of damage. In the case of the pit depicted in Figure 5.7a, the stress intensity factor is above K_{ISCC} but no IGSCC was observed. One possible explanation is that the corroded site has not reached a grain boundary and therefore, the transition from corrosion to IGSCC cannot occur. A pitted site where IGSCC was observed is depicted in Figure 5.8. The stress intensity factor for this corroded site is above K_{ISCC}. It is therefore not surprising to observe the transition from pitting to IGSCC in this area.

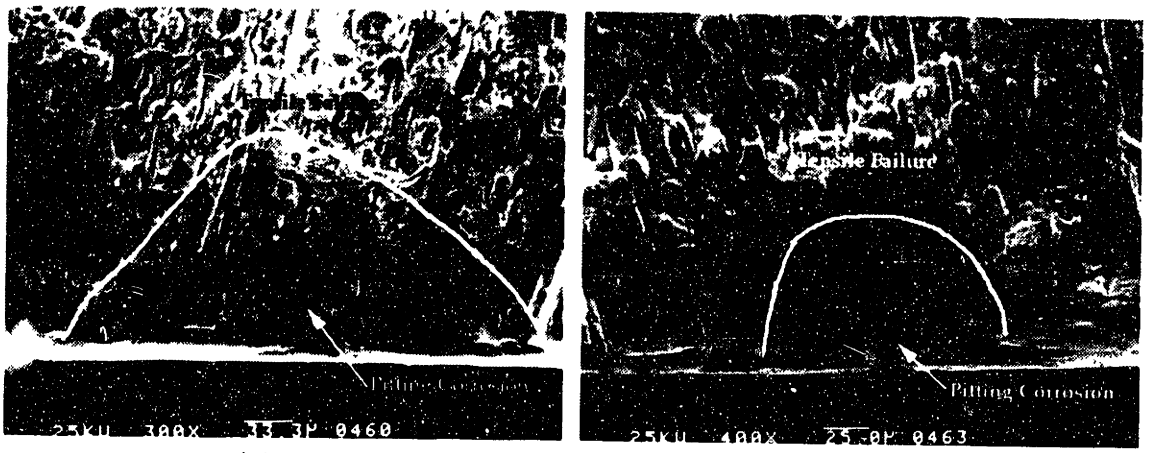

(a) (b)

Figure 5.7. Fractographs showing that the transition from pitting to IGSCC has not occurred in these corroded sites.

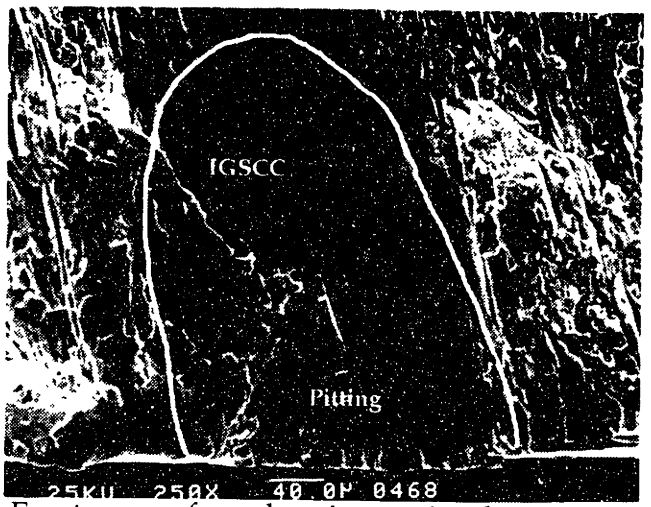

Figure 5.8. Fracture surface showing a pitted site. IGSCC and the subsequent tensile failure can be seen originating from the pit.

5.5 Practical Implications

A mechanistic model can be proposed to explain the observed corrosion and the subsequent formation of intergranular stress corrosion cracks around steel riveted wing joints. Mechanical wear, for example, can form a crevice between the steel rivet and the aluminum panel. This allows a chloride containing conductive electrolyte to seep into the joint. It has been demonstrated that the constituent particles in 7075-T651 and 7178-T6 can polarize the matrix above the pitting potential when the electrolyte is aerated. These constituent particles however, are unable to cause intergranular attack (IGA). The steel rivet, on the other hand, can polarize the aluminum panel

above both E_{iga} and E_{pit} in either deaerated or aerated solutions. In other words, the constituent particles can only cause pitting but not IGA in aerated solutions while the steel rivet can cause both pitting and IGA in either aerated and deaerated conditions. Hence, localized breakdown occurs spontaneously on the aluminum panel where it is electrically coupled to the steel rivet. This explains the fact that corrosion often occurs on the aluminum alloy in the countersink and shank area of riveted joints and that the corrosion is much more extensive if the rivet is made from steel.

The oxygen in the electrolyte is consumed by the cathodic reaction as dissolution continues. Mass transport to the corroding area is limited because it is in an occluded region. As a result, the oxygen content in the electrolyte drops as the corrosion reaction continues. The corrosion potential of 7075-T651 and 7178-T6, in either aerated or deaerated solutions, are more noble than the repassivation potential. Thus, these materials cannot spontaneously repassivate. Once breakdown has occurred, active dissolution continues. Hydrolysis of the dissolved metal ion can lower the pH to 3.5 at the bottom of a pit. Aluminum ions, rather than aluminum oxide, becomes the thermodynamically stable product in this environment. Repassivation is therefore impossible at these actively corroding sites. The corrosion process can become autocatalytic as increased dissolution rate occurs with decreasing pH. This explains the severity and rapidity of corrosion damages observed around steel riveted wing joints.

When the wing panel is under a tensile load, and the corroded site is in the vicinity of a grain boundary, intergranular stress corrosion cracks may develop. If the crack growth rate is smaller than the corrosion rate, pitting remains the dominant form of damage. When the crack growth rate exceeds the corrosion rate, IGSCC can be observed.

6.0 Conclusions and Key Findings

6.1 Conclusions

A study of the fundamental mechanisms of localized corrosion has been conducted for two aluminum airframe structural materials, 7178-T6 and 7075-T651. Alloy 7178 represents a higher strength material used in airframes such as the KC-135 and B-52. Alloy 7075 has a higher fracture toughness and is used in more recent airframes.

The dynamic and cyclic polarization behavior of aluminum alloys 7178-T6 and 7075-T651 was investigated in aerated and deaerated chloride environments. Two breakdown potentials were observed for these materials. The more noble breakdown potential is related to corrosion around constituent particles while the more active breakdown potential is associated with the dissolution of grain boundaries. These potentials are associated with the initiation of pitting and intergranular attack respectively. The breakdown potentials follow the logarithmic relationship with chloride ion activity and are linearly dependent on the reciprocal of the absolute temperature. The repassivation potential for these materials were found to be more noble than the corrosion potential in either aerated or deaerated environments. In other words, these materials cannot spontaneously repassivate. Once localized breakdown has occurred, active dissolution continues.

Constituent particles have often been found to be the site of localized breakdown in these alloys. In order to understand the fundamental role of these particles, five intermetallics were produced in bulk to simulate the constituent particles found in commercial aluminum alloys. Three of the alloys produced are variants on the phase Al_2Cu with different concentrations of Zn (0 - 1.6 wt.%). The other two are $Al_6(Fe,Cu)$ and Al_3Fe. The chemical compositions and crystal structures of these alloys were verified and are found to be similar to those of the constituent particles.

Dynamic polarization studies were conducted on all the intermetallics. Experiments were also conducted on pure aluminum for comparison purposes. The results indicate that Zn does not have a strong influence on the corrosion properties of the phase Al_2Cu. The corrosion potential and

polarization behavior of the three alloys with varying amount of Zn are virtually identical. All the intermetallics were found to be more noble than aluminum. The hydrogen and oxygen exchange current density on these intermetallics are several orders of magnitude higher than that on aluminum. The particles are all cathodic in relation to aluminum. As a result, aluminum will be polarized to more noble potentials when it is electrically coupled to these alloys. In deaerated conditions, the constituent particles cannot polarize aluminum above its breakdown potential. In aerated solutions however, localized breakdown can be expected. These observations are in accordance with the published literature. It is reported that the electrolyte must contain dissolved oxygen for localized breakdown to occur. Modeling the corrosion behavior of aluminum alloys as electrically coupled samples of pure aluminum - constituent particles is both valid and successful.

Two riveted joints from a replaced wing panel were dismantled and examined for corrosion damage. The electrochemical behavior of the steel rivet and the wing panel was obtained independently via potentiodynamic experiments. The data were then combined in accordance with the mixed potential theory and used to predict the corrosion behavior of the joint assembly as a whole. The results indicate that the steel rivet is cathodic in relation to the aluminum alloys. The steel rivet can cause both pitting and intergranular attack on the aluminum panel in either aerated and deaerated solutions. Since the aluminum alloys cannot spontaneously repassivate, active dissolution continues. This provides an explanation to the fact that severe corrosion damage is often observed in the countersink and shank area of riveted joints.

Intergranular stress corrosion cracks which initiate from pits have been successfully reproduced in the laboratory.

6.2 Key Findings

As a result of this research, the following key findings and original contributions have been made.

1. A detailed and fundamental understanding of the source of pits and intergranular attack initiation in aluminum alloys 7178 and 7075 has been developed.

2. A fundamental understanding of the role of the constituent particles in pit initiation has been developed.

3. The electrochemical properties of the constituent particles in alloys 7178 and 7075 have been studied in detail.

4. The mixed potential theory has been applied to model the role of environment and microstructural features in the pit initiation process.

5. The results of this research have been applied to actual riveted joints to rationalize the observed corrosion behavior.

6. While alloy 7178 is more susceptible to pitting and intergranular attack than 7075, both of these materials can be expected to degrade with time.

7.0 Future Work

In this research work, the electrochemical properties of constituent particles which caused localized film breakdown have been studied in detail. Future work should investigate the properties of constituent particles which do not cause localized film breakdown. Silicon rich particles are prime candidates for such studies.

The effect of area fraction of constituent particles on the corrosion properties of aluminum alloys has been studied. The relationship between the corrosion properties and other material parameters, such as the number of constituent particles per unit area, the size of the constituent particles, and the average distance between the particles, should be studied.

The potential is maintained to be more noble than E_{pit} and more active than E_{iga} in all the stress corrosion cracking studies conducted for this research. Future work should investigate the role of potential on the stress corrosion cracking behavior of these high strength aluminum alloys. Tests should be conducted with potential more active than E_{pit} and more noble than E_{iga}.

A set of guidelines has been developed to compare the corrosion performance of various aluminum alloys. The corrosion properties of other aluminum alloys that are used for aircraft structures, such as 7049, 7050, and 7079, should also be studied. A data bank can then be compiled which can be useful for material selection purposes.

The materials used in this research program are in the peak aged condition. The effect of heat treatment on the corrosion properties of aluminum alloys should be investigated. Other heat treatment conditions include T4, T6, and T73.

The kinetics of corrosion processes, such as the pit growth rate and the intergranular dissolution rate, should be studied. Quantitative predictions of the corrosion damage can then be developed.

Appendices

A. Chemical Composition of Second Phase Particles

Large second phase intermetallic particles were found on 7178-T651 and 7075-T6 plates after electrochemical experiments. These particles were analysed in-situ by energy dispersive x-ray spectroscopy (EDX) and the results are presented in Table A.1.

Table A.1. Results of EDX analysis on second phase particles found on 7178-T6 and 7075-T651 plates.

	Atomic %						
	Al	Si	Fe	Cu	Zn	Cr	Mg
Al-Cu-Zn							
A6-SP2-62	85.10			12.58	2.32		
A6-SP2-61	75.97	1.18		20.45	2.41		
A6-SP3-107-4	68.18			27.51	2.67		1.64
A6-SP3-107-3	67.84			28.52	2.05		1.59
A6-SP3-107-2	68.52			29.36	2.12		
A6-SP3-107-1	65.49			31.57	2.94		
A4-SP1-5-3	56.50			42.26	1.15	0.10	
A4-SP1-5-2	41.75		0.06	57.33	0.74	0.12	
A4-SP1-5-1	36.68		0.78	62.26		0.28	
Al-Fe-Cu-Zn							
B3-SP1-135	86.24		8.67	2.65	2.01	0.42	
A6-SP3-104-1	69.51		8.70	21.80			
B3-SP1-138-2	80.87		10.32	4.15	1.27	3.40	
A6-SP3-105-1	61.36		10.87	27.77		1.17	
A6-SP3-105-2	69.40		10.88	16.54	2.01	0.00	
B3-SP1-138-1	79.80		11.67	3.97	0.85	3.70	
A6-SP3-105-4	80.84		11.88	3.86	3.42		
A6-SP3-105-3	75.17		16.78	3.61	1.86	2.58	
Al-Si							
B2-SP1-23-1	86.07	10.33		1.27	2.33		
B3-SP1-132-1	74.05	22.59		0.68	2.68		
A6-SP2-64	67.38	28.69		0.92	3.00		
B2-SP1-23-2	56.00	41.92		0.93	1.15		
B3-SP1-139-1	54.57	43.07		0.58	1.78		
B3-SP1-139-2	50.79	46.42		0.40	2.39		

B. Regression Analysis on Breakdown Potentials

Breakdown potentials were obtained from dynamic polarization scans of 7178-T651 and 7075-T651 in 0.10, 0.30, 1.0, 3.0, and 5.0M (saturation at 298K) NaCl solutions at 298K. The concentrations are converted to activities according to the activity coefficients listed in Table 4.1. Results from regression analysis are presented below. The potentials used in these equations are in mV, SCE.

$$E_{pit}\ 7075\text{-LS} = -777 - 75.2 \log(a_{Cl^-}) \qquad R^2=0.982 \qquad (B.1)$$

$$E_{pit}\ 7075\text{-LT} = -774 - 76.9 \log(a_{Cl^-}) \qquad R^2=0.993 \qquad (B.2)$$

$$E_{pit}\ 7075\text{-ST} = -780 - 78.7 \log(a_{Cl^-}) \qquad R^2=0.995 \qquad (B.3)$$

$$E_{pit}\ 7178\text{-LS} = -799 - 87.2 \log(a_{Cl^-}) \qquad R^2=0.990 \qquad (B.4)$$

$$E_{pit}\ 7178\text{-LT} = -797 - 77.2 \log(a_{Cl^-}) \qquad R^2=0.962 \qquad (B.5)$$

$$E_{pit}\ 7178\text{-ST} = -796 - 77.6 \log(a_{Cl^-}) \qquad R^2=0.978 \qquad (B.6)$$

$$E_{iga}\ 7075\text{-LS} = -740 - 73.7 \log(a_{Cl^-}) \qquad R^2=0.996 \qquad (B.7)$$

$$E_{iga}\ 7075\text{-LT} = -744 - 77.9 \log(a_{Cl^-}) \qquad R^2=0.994 \qquad (B.8)$$

$$E_{iga}\ 7075\text{-ST} = -749 - 86.5 \log(a_{Cl^-}) \qquad R^2=0.996 \qquad (B.9)$$

$$E_{iga}\ 7178\text{-LS} = -760 - 80.1 \log(a_{Cl^-}) \qquad R^2=0.989 \qquad (B.10)$$

$$E_{iga}\ 7178\text{-LT} = -750 - 82.7 \log(a_{Cl^-}) \qquad R^2=0.983 \qquad (B.11)$$

$$E_{iga}\ 7178\text{-ST} = -757 - 82.4 \log(a_{Cl^-}) \qquad R^2=0.988 \qquad (B.12)$$

Linear polarization experiments were conducted in 1.0M NaCl solutions at 298K, 308K, 318K, and 323K (Figures 4.19 and 4.20). Results from linear regression analysis are presented below. The temperatures used in these equations are in degrees Kelvin.

$$E_{pit}\ 7075\text{-LS} = -1130 + 114\,(1000/T) \qquad R^2=0.967 \qquad \text{(B.13)}$$

$$E_{pit}\ 7075\text{-LT} = -1320 + 170\,(1000/T) \qquad R^2=0.976 \qquad \text{(B.14)}$$

$$E_{pit}\ 7075\text{-ST} = -1040 + 82.1\,(1000/T) \qquad R^2=0.917 \qquad \text{(B.15)}$$

$$E_{pit}\ 7178\text{-LS} = -1120 + 102\,(1000/T) \qquad R^2=0.988 \qquad \text{(B.16)}$$

$$E_{pit}\ 7178\text{-LT} = -1550 + 234\,(1000/T) \qquad R^2=0.997 \qquad \text{(B.17)}$$

$$E_{pit}\ 7178\text{-ST} = -1130 + 106\,(1000/T) \qquad R^2=0.889 \qquad \text{(B.18)}$$

$$E_{iga}\ 7075\text{-LS} = -981 + 75.5\,(1000/T) \qquad R^2=0.991 \qquad \text{(B.19)}$$

$$E_{iga}\ 7075\text{-LT} = -1090 + 108\,(1000/T) \qquad R^2=0.999 \qquad \text{(B.20)}$$

$$E_{iga}\ 7075\text{-ST} = -1020 + 84.1\,(1000/T) \qquad R^2=0.912 \qquad \text{(B.21)}$$

$$E_{iga}\ 7178\text{-LS} = -820 + 29.8\,(1000/T) \qquad R^2=0.538 \qquad \text{(B.22)}$$

$$E_{iga}\ 7178\text{-LT} = -1440 + 215\,(1000/T) \qquad R^2=0.999 \qquad \text{(B.23)}$$

$$E_{iga}\ 7178\text{-ST} = -910 + 48.8\,(1000/T) \qquad R^2=0.623 \qquad \text{(B.24)}$$

Bibliography

1. W.W. Wallace, D.W. Hoeppner, AGARD Corrosion Handbook, Volume 1, Aircraft Corrosion: Causes and Case Histories, 1985, pp. 101-102.

2. S. Barter, P.K. Sharp, and G. Clark, "The Failure of an F/A-18 Trailing Edge Flap Hinge", Engineering Failure Analysis, vol. 1, 1994, pp. 255-266.

3. J. Tafel, Z. Physik. Chem., vol. 50, 1904, p.641.

4. A.J. Bard, and L.R. Faulkner, Electrochemical Methods: Fundamentals and Applications, John Riley & Sons, New York, New York, 1980, p. 107.

5. M.G. Fontana, and N.D. Greene, Corrosion Engineering, McGraw-Hill Book, New York, New York, 1978, p.314.

6. N.D. Tomashov, Theory of Corrosion and Protection of Metals, The Macmillan Company, New York, New York, 1966, pp. 211-218.

7. M.O. Speidel, M.V. Hyatt, "Stress-Corrosion Cracking of High-Strength Aluminum Alloys", Advances in Corrosion Science and Technology, Volume 2, eds. M.G. Fontana and R.W. Staehle, Plenum Press, New York, 1972.

8. J.E. Hatch, Aluminum: Properties and Physical Metallurgy, American Society for Metals, Metals Park, 1984, p.143-147.

9. A.J. Sedriks, J.A.S. Green, and D.L. Novak, "Corrosion Processes and Solution Chemistry Within Stress Corrosion Cracks in Aluminum Alloys", Localized Corrosion, B.F. Brown, J. Kruger, and R.W. Staehle, eds., 1971, National Association of Corrosion Engineers, Houston, Texas, pp. 569-575.

10. Registration Record of Aluminum Association Alloy Designations and Chemical Composition Limits for Wrought Aluminum Alloys, The Aluminum Association.

11. M.O. Speidel, M.V. Hyatt, "Stress-Corrosion Cracking of High-Strength Aluminum Alloys", Advances in Corrosion Science and Technology, Volume 2, eds. M.G. Fontana and R.W. Staehle, Plenum Press, New York, 1972, p.121.

12. M.O. Speidel, M.V. Hyatt, "Stress-Corrosion Cracking of High-Strength Aluminum Alloys", Advances in Corrosion Science and Technology, Volume 2, eds. M.G. Fontana and R.W. Staehle, Plenum Press, New York, 1972, p. 119.

13. J.J. Thompson, E.S. Tankins, and V.S. Agarwala, "A Heat Treatment for Reducing Corrosion and Stress Corrosion Cracking Susceptibilities in 7XXX Aluminum Alloys", Material Performance, vol. 26, 1987, pp. 45-52.

14. R.H. Brown, W.I. Fink, and M.S. Hunter, "Measurement of Irreversible Potentials as a Metallurgical Tool", Trans. AIME, 1941, pp. 115-123.

15. E.H. Dix, R.H. Brown, and W.W. Binger, "The Resistance of Aluminum Alloys to Corrosion", Metals Handbook, 8th edition, vol. 1, Metals Park, Ohio, pp. 916-928.

16. E.H. Dix, "Acceleration of the Rate of Corrosion by High Constant Stress", Trans. AIME, 1940, pp. 11-40.

17. Metals Handbook, 9th edition, vol. 13, 1987, p.584.

18. J.R. Galvele, and S.M. De De Micheli, "Mechanism of Intergranular Corrosion of Al-Cu Alloys", Corrosion Science, vol.10, 1970, pp. 795-807.

19. J.R. Galvele, S.M.de De Micheli, I.L. Mueller, S.B. de Wexler, and I.L. Alanis, "Critical Potentials for Localized Corrosion of Aluminum Alloys", Localized Corrosion, NACE 3, R. Staehle, B. Brown, J. Kruger, A. Agrawals, Eds., National Association of Corrosion Engineers, Houston, Texas, 1974, pp. 580-599.

20. M. Pourbaix, Atlas of Electrochemical Equilibria in Aqueous Solutions, National Association of Corrosion Engineers, Houston, 1974.

21. W. Hübner, G. Wranglen, "Studies on the Mechanism of the Pitting Corrosion of Aluminum", Current Corrosion Research in Scandinavia, Lectures held at the Fourth Scandinavian Corrosion Congress, 1964, Helsinki, J. Larinkari, eds., pp.60-69.

22. G. Sussek, and M. Kestern, "Eine Charakterisierung der Lochfrabkorrosion des Nickels - I. Die Bestimmung der Lochfrabpotentiale in Neutralen und Alkalischen Lösungen" (Abstract), Corrosion Science, vol. 15, 1975, pp.225-238.

23. H.H. Strehblow, and B. Titze, "Pitting Potentials and Inhibition Potentials of Iron for Different Aggressive and Inhibiting Anions", Corrosion Science, vol. 17, 1977, pp. 461-472.

24. Z.A. Foroulis, and M.J. Thubrikar, "On the Kinetics of the Breakdown of Passivity of Preanodized Aluminum by Chloride Ions", J. Electrochem. Soc., vol. 122, 1975, pp. 1296-1301.

25. Z. Szklarska-Smialowska, Pitting Corrosion of Metals, National Association of Corrosion Engineers, Houston, Texas, 1986, pp. 203-205.

26. H. Bohni, and H.H. Uhlig, Corrosion Science, vol. 9, (1969) p.353.

27. N. Nilsen, and E. Bardal, "Short Duration Tests and a New Criterion for Characterization of Pitting Resistance of Al Alloys", Corrosion Science, vol. 17, 1977, pp. 635-646.

28. D.S. Keir, M.J. Pryor, P.R. Sperry, "Galvanic Corrosion Characteristics of Aluminum Alloyed with Group IV Metals", J. Electrochem. Soc., vol. 114, 1967, pp. 777-782.

29. G.C. Wood, W.H. Sutton, J.A. Richardson, T.N.K. Riley, and A.G. Malherbe, "The Mechanism of Pitting of Aluminum and Its Alloys", Localized Corrosion, NACE 3, R. Staehle, B. Brown, J. Kruger, A. Agrawals, Eds., National Association of Corrosion Engineers, Houston, Texas, 1974, pp. 526-539.

30. Z. Szklarska-Smialowska, "Insight into the Pitting Corrosion Behavior of Aluminum Alloys", Corrosion Science, vol. 33, 1992, pp. 1193-1202.

31. O. Seri, "The Effect of NaCl Concentration on the Corrosion Behavior of Aluminum Containing Iron", Corrosion Science, vol. 36, 1994, pp. 1789-1803.

32. ASTM G34-90, "Standard Test Method for Exfoliation Corrosion Susceptibility in 2XXX and 7XXX Series Aluminum Alloys (EXCO Test)".

33. D.G. Evans, P.W. Jeffrey, "Exfoliation of AlZnMg Alloys", Localized Corrosion, NACE 3, R. Staehle, B. Brown, J. Kruger, A. Agrawals, Eds., National Association of Corrosion Engineers, Houston, Texas, 1974, pp. 614-622.

34. "Effects of Alloying Elements and Impurities on Properties", Aluminum: Properties and Physical Metallurgy, J.E. Hatch, Eds., American Society for Metals, Metals Park, Ohio, 1984, pp. 230-231.

35. G.A.W. Murray, H.J. Lamb, and H.P. Godard, "Role of Iron in Aluminum on the Initiation of Pitting in Water", Brit. Corros. J., vol. 2, 1967, pp. 216-218.

36. P.M. Aziz, and M.S. Walker, "Pitting Corrosion Characteristics of Aluminum", Corrosion, vol. 10, 1954, pp. 269-279.

37. G.A. Gehring, and M.H. Peterson, "Corrosion of 5456-H117 Aluminum in High Velocity Sea Water", Corrosion, vol. 37, (1981), pp. 232-242.

38. Aluminum and Aluminum Alloys, J.R. Davis, and Davis & Associates, eds., ASM, Metals Park, Ohio, 1993, pp. 31-33.

39. M.O. Speidel, and M.V. Hyatt, "Stress-Corrosion Cracking of High-Strength Aluminum Alloys", Advances in Corrosion Science and Technology, vol.2, M.G. Fontana, and R.W. Staehle, eds., Plenum Press, New York, 1972, pp.299-305.

40. N.J.H. Holroyd, "Environment-Induced Cracking of High-Strength Aluminum Alloys", Environment-Induced Cracking of Metals, Proceedings of the First International Conference on Environment-induced Cracking of Metals, R.P. Gangloff, M.B. Ives, Eds., National Association of Corrosion Engineers, Houston, 1988, pp. 311-345.

41. M.O. Speidel, and M.V. Hyatt, "Stress-Corrosion Cracking of High-Strength Aluminum Alloys", Advances in Corrosion Science and Technology, vol.2, M.G. Fontana, and R.W. Staehle, eds., Plenum Press, New York, 1972.

42. S. Maitra, and G.C. English, "Mechanism of Localized Corrosion of 7075 Alloy Plate", Met. Tran. A, vol. 12A, 1981, pp.535-541.

43. S. Maitra, and G.C. English, "Environmental Factors Affecting Localized Corrosion of 7075-T7351 Alminum Alloy Plate", Met. Tran. A, vol. 13A, 1982, pp.161-166.

44. S.C. Byrne, "Effect of Microstructure on Stress-Corrosion Cracking in 7075-T7", Aluminum Alloys - Physical and Mechanical Properties, T.H. Sanders, and E.A. Starke, eds., 1986, pp.1095-1107.

45. P.K. Poulose, J.E. Morral, and A.J. McEvily, "Stress Corrosion Crack Velocity and Grain Boundary Precipitates in Al-Zn-Mg Alloy", Met. Tran., vol. 5, 1974, pp.1393-1400.

46. P.N. Adler, R. De Isai, G. Geschwind, "Influence of Microstructure on the Mechanical Properties and Stress Corrosion Susceptibility of 7075 Aluminum Alloy", Met. Trans., 3 (1972), p.3191.

47. A.J. De Ardo, R.D. Townsend, Met. Trans., vol. 1, 1970, p.2573.

48. I.J. Polmear, J. Aust. Inst. Metals, vol. 89, 1960, p.193.

49. A.J. Sedriks, P.W. Slattery, E.N. Pugh, Trans. ASM, vol. 26, 1969, p.238.

50. R.M. Pelloux, and J.A. Van den Avyle, Hydrogen in Metals, I.M. Bernstein, and A.W. Thompson, eds., ASM, Metals Park, Ohio, 1974, pp. 275-276.

51. J.A. Albrecht, B.J.M. McTiernan, I.M. Bernstein, and A.W. Thompson, "Hydrogen Embrittlement in High-Strength Aluminum Alloys", Scripta Met., vol. 11, 1977, pp. 893-897.

52. T.F. Klimowicz, and R.M. Latanision, "On the Embrittlement of Aluminum Alloys by Cathodic Hydrogen: The Role of Surface Films", Met. Trans. A, vol. 9A, 1978, pp.597-599.

53. I.M. Bernstein, and A.W. Thompson, "An Evaluation of Hydrogen Embrittlement Mechanism", Mechanisms of Environment Sensitive Cracking of Materials, Swann, Ford, and Westwood, eds., 1977, Metals Society, London, pp. 412-491.

54. S.P. Lynch, "Environmentally Assisted Cracking: Overview of Evidence for an Adsorption Induced Localized-Slip Process", Acta Met., vol. 36, 1988, pp. 2639-2661.

55. G.M. Scamans, N.H.J. Holroyd, and C.D.S. Tuck, "The Role of Magnessium Segregation in the Intergranular Stress Corrosion Cracking of Aluminum Alloys", Corrosion Science, vol. 27, 1987, pp.329-347.

56. S.W. Ciaraldi, J.L. Nelson, R.A. Yaske, and E.N. Pugh, "Studies of Hydrogen Embrittlement and Stress-Corrosion Cracking in an Aluminum-Zinc-Magnessium Alloy", Hydrogen Effects in Metals, I.M. Bernstein, and A.W. Thompson, eds., Metallurgical Society of AIME, 1981, Warrendale, Pennsylvania, pp.437-447.

57. K. Rajan, W. Wallace, and J.C. Beddoes, "Microstructural Study of a High Strength Stress-Corrosion Resistant 7075 Aluminum Alloy", J. Materials Science, vol. 17, 1982, pp. 2817-2824.

58. Z.X. Tong, Sl Lin, and C.M. Hsiao, "The Influence of Hydrogen on Atomic Binding Energy, Critical Slip Shear Stress, and Fatigue Crack Propagation Rate of Aluminum Single Crystals", Met. Trans. A, vol. 20A, 1989, pp. 921-924.

59. C.P. You, M. Dollar, A.W. Thompson, and I.M. Bernstein, "Microstructure Property Relationships and Hydrogen Effects in a Particulate-Reinforced Aluminum Composite", Met. Tran. A., vol. 22A, 1991, pp. 2445-2450.

60. H.P. Van Leeuvwan, "A Quantative Model of Hydrogen Induced Grain Boundary Cracking", Corrrosion, vol. 29, 1973, pp.197-204.

61. J. Albrecht, I.M. Bernstein, and A.W. Thompson, "Evidence for Dislocation Transport of Hydrogen in Aluminum", Met. Trans. A, vol. 13A, 1982, pp. 811-820.

62. W. Gruhl, "Stress Corrosion Cracking of High Strength Aluminum Alloys", Z. Metallkd, vol. 75, 1984, pp.819-826.

63. A.W. Thompson, M.A. Mueller, and I.M. Bernstein, "Stress-Corrosion Cracking in Equiaxed 7075 Aluminum under Tension and Torsion Loading", Met. Tran. A., vol. 24A, 1993, pp.2569-2575.

64. M.O. Speidel, "Interaction of Dislocations with Precipitates in High Strength Aluminum Alloys and Susceptibility to Stress Corrosion Cracking", Fundamental Aspects of Stress Corrosion Cracking, R.W. Staehle, eds., 1967, pp.561-579.

65. F.S. Lin, E.A. Starke, "The Effect of Copper Content and Degree of Recrystallization on the Fatigue Resistance of 7XXX Type Aluminum Alloys. I. Low Cycle Corrosion Fatigue", Mater. Sci. Eng., 39 (1979), pp.27-41.

66. D.A. Hardwick, A.W. Thompson, and I.M. Bernstein, "The Effect of Copper Content and Microstructure of the Hydrogen Embrittlement of Al-6Zn-2Mg Alloys," Met. Trans. A., vol. 14A, 1983, pp. 2517-2526.

67. J. Albrecht, A.W. Thompson, and I.M. Bernstein, "The Role of Microstructure in Hydrogen-Assisted Fracture of 7075 Aluminum", Met. Trans. A., vol. 10A, 1979, pp.1759-1766.

68. P. Villars, and L.D. Calvert, Pearson's Handbook of Crystallographic Data for Intermetallic Phases, Volume 2, ASM, Metals Park, OH, 1985, p.973.

69. L.F. Mondolfo, Aluminum Alloys: Structure and Properties, Butterworths, Boston, 1976, p.284.

70. G.F. Vander Voort, Metallography Principles and Practices, McGraw-Hill, 1984, p.610.

71. F.P. Beer, and E.R. Johnston, Jr., Mechanics of Materials, McGraw-Hill Book Company, New York, 1981, pp.156-158.

72. H.H. Uhlig, and R.W. Revie, Corrosion and Corrosion Control, John Wiley & Sons, New York, NY, 1985, pp. 406-408.

73. J.C. Newman, Jr., and I.S. Raju, "Stress-Intensity Factor Equations for Cracks in Three-Dimensional Finite Bodies Subjected to Tension and Bending Loads", Computational Methods in the Mechanics of Fracture, eds. S.N. Atluri, Elsevier Science Publishers, 1986, pp. 318-321.

74. T.D. Burleigh, R.C. Rennick, and F.S. Bovard, "Corrosion Potential for Aluminum Alloys Measured by ASTM G69," Corrosion, 1993, Vol. 49, pp.683-685.

75. H.H. Strehblow, and B. Titze, "Pitting Potentials and Inhibition Potentials of Iron for Different Aggressive and Inhibiting Anions", Corrosion Science, vol. 17, 1977, pp. 461-472.

76. H. Bohni, and H.H. Uhlig, Corrosion Science, vol. 9, 1969, p.353.

77. L.F. Mondolfo, Aluminum Alloys: Structure and Properties, Butterworths, London, Year, pp. 518-520.

THESIS PROCESSING SLIP

FIXED FIELD: ill. _____ name _____

index _____ biblio _____

► COPIES: (Archives) Aero Dewey Eng Hum

Lindgren Music Rotch (Science)

TITLE VARIES: ► ☐ _____

NAME VARIES: ► ☒ Sc degree book

IMPRINT: (COPYRIGHT) _____

► COLLATION: 142 ℓ

► ADD. DEGREE: _____ ► DEPT.: _____

SUPERVISORS: _____

NOTES:

cat'r: date:

page: F49

► DEPT: MatSci & E

► YEAR: 1996 ► DEGREE: Sc.D.

► NAME: AU, Hiu